PROCESSING CONSIDERATIONS FOR THE COMBUSTION SYNTHESIS OF YTTRIUM ALUMINUM GARNET POWDERS

by

Robert Randall Harl, Jr.

Dissertation Submitted to the Faculty of the

Graduate School of Vanderbilt University

in partial fulfillment of the requirements

for the degree of

DOCTOR OF PHILOSOPHY

in

CHEMICAL ENGINEERING

DECEMBER 2013

Nashville, Tennessee

Approved:

Professor Bridget R. Rogers (Chair), Ph.D.

Professor Kenneth A. Debelak, Ph.D

Professor M. Douglas LeVan, Ph.D.

Professor D. Greg Walker, Ph.D.

To my parents, Randy and Cassie, brother, Grant, and extended family for their relentless support during my life's biggest challenge.

ACKNOWLEDGEMENTS

The path to the PhD has brought me into contact with a plethora of talented individuals without whom I would never have been able to complete this body of work. Besides the insight I gained through interacting with all of these individuals from a scientific perspective, the camaraderie developed outside of the lab was just as crucial to help maintain a life balance.

I will start by thanking Dr. Bridget Rogers for providing me a place in her lab, guiding my scientific enthusiasm and giving me opportunities to work with other talented individuals to become a well-trained experimentalist. My committee also deserves a big thank you, I appreciate your willingness to be on my committee and sacrifice your time for constructive feedback on my progress to the PhD. The next three people who deserve recognition are Dr. Benjamin Schmidt, Dr. Steve Vilt and Spencer Crowder, all friends since the beginning of the PhD experience. Ben is still around and we still discuss topics from research to life, and for that I owe him a debt. Steve has moved away from Nashville, but the late nights and early mornings would have been far less bearable without him around. As for Spencer Crowder, I have too many words to describe the comraderie inherent in my fellow Texan so I'll keep it simple and Texan: thank ya.' I would also like to recognize the first year class of 2009 and specifically Carlos Escobar and Lucas Mitchell for being fantastic friends and scientific collaborators. In addition to those I've known since I got here, there have been friends across campus and I'll provide a truncated list here: Dr. Brandon Booth, Bob Marvel, Dhiraj Prasai, Sarah Gollub, Courtney Mitchell, Marc Panu, Tim Moore, Taylor Murphy, Jason Ballangee, Will French, Margarita Chacón, James McBride and Juan Tuberquia. There are many more, and thank you all who I've met during this journey.

In addition to my peers I've been lucky to have dealt with many of the faculty at Vanderbilt and I would like to recognize their guidance and support during this work. Doug LeVan was always there to commiserate on my interest in beer and unbeknownst to him usually provided me the motivation I lacked to brew a new batch. Greg Walker helped to guide my efforts in meetings and during discussions that occurred outside designated meeting times and I only regret we never played music together. Kane

Jennings involved me in multiple collaborations and beyond the work Kane was always open to discussing topics as wide ranging as football and the new recruiting class. Marcus Mendenhall for being the brilliant and open person he is, coaching me at how to run a particle accelerator properly and discussing the physics involved as well as his enthusiasm about his hiking adventures. In addition, working with Mike McCurdy, Rich Gregory, Bob Weller, Robert Reed, all of the people at Physical Electronics, especially Brian Yates and Dan Stockinger, and the install team from NEC provided me practical experience and friendship.

Those were all people who helped me learn on a conceptual level, and now I get to the people that really helped me get things done. This thesis would not be possible without the help from Mark Holmes, Robin Midgett, Mary Gilleran, Rae Uson and Rossane DeLapp. To all of you, I say thank you and want to express my full appreciation for everything you did for me over the past four years.

Most importantly I want to thank my family, both extended and immediate, for supporting my work these last four years. At times people wondered how I could still be in school, and even after the ink has dried on this dissertation I'll still be in school, but they never undermined the importance of the education. To my Mom and Dad, who always knew I could accomplish this, thank you for suggesting this as a path forward for me. Your experience and guidance from birth gave me the tools to accomplish this major life accomplishment. Grant, thank you for being there to try to get me to believe some things didn't matter. The still did, but at least I dealt with it easier.

Lastly, I'd like to acknowledge and thank my funding sources throughout this work: the Defense Threat Reduction Agency (DTRA) under grand HDTRA1-10-11-0112 and the Department of Education for a Graduate Assistance in Areas of National Need (GAANN) Fellowship under grant number P200A090323 .

As Tolkein wrote, "It's the job that's never started as takes the longest to finish." I thus begin my dissertation; thank you all.

TABLE OF CONTENTS

TABLE OF TABLES

TABLE OF FIGURES

CHAPTER 1

BACKGROUND

Introduction

Rare-earth doped yttrium aluminum garnet (YAG), yttrium borate (YBO) and lanthanum zirconate (LZO) are luminescent ceramics that have been used in TV's, LED's, metal oxide transistors, and as laser sources[1-5]. These materials are crystalline ceramics that are stable at high temperatures and chemically resistant, making them candidate materials for use as thermal barrier coatings or as components in solid-oxide fuel cells[5,6].

Crystalline YAG, YBO and LZO are ceramic phosphors that luminesce after absorbing energy via radiation. These materials luminesce after absorbing short wavelength radiation and have a delay in photonic emission. The ability to emit photons after absorbing short wavelength light is known as photoluminescence (PL). The delay in photonic emission is known as phosphorescence (PR)[7]. PR is characterized by having electron relaxation times greater than 0.1s[7,8]. PL occurring with relaxation times less than 0.1s is referred to as fluorescence.

Luminescence is initiated by the adsorption of radiative energy that promotes an electron to an excited state. The system then relaxes by emitting a photon. Luminescence is a broad term for the phenomena and is often categorized based on the types of excitation radiation. As mentioned above, PL describes luminescence following short wavelength radiation excitation. Luminescence occurring after excitation by high-energy

electrons is known as cathodoluminescence. Electroluminescence describes luminescence resulting from electrons excited by an applied electric field[7].

Figure 1.1 shows examples of different energy transitions that can lead to photon emission in PL materials. Figure 1.1 shows band-to-band transitions, which can occur by intrinsic or extrinsic luminescence. Intrinsic luminescent (IL) materials are pure semiconductors such as Si and Ge. These three transitions require relatively high (950ºK) or low (77ºK) temperatures in pure crystals to occur[7].

Ionic crystals and crystalline oxides are some examples of extrinsic luminescent (EL) materials. Unlike the bulk semiconductor luminescence, rare-earth activators will be responsible for the photoluminescence in the oxide phosphors of interest to this work. The rare-earth activators, also known as dopants, are intrinsically luminescent; the luminescence occurs on an atomic level due to electrons transitioning between energy levels of the orbitals of the chosen dopant.[9] The rare-earth elements typically are the lanthanide elements plus scandium and yttrium however Sc^{+3}, Y^{3+}, La^{3+} and Lu^{3+} have no 4f electrons and thus do not produce luminescence in the visible spectrum.[9] The remaining elements in the lanthanide series do produce luminescence originating from electronic transitions between 4f levels. These transitions are primarily due to electric dipole or magnetic dipole interactions.[9] In the case of electronic dipole interactions, the f-f transitions are parity forbidden in an isolated dopant element however the overlap of the dopant and host crystal element orbitals makes them partially allowed.[9] Magnetic dipole transitions are parity allowed and thus are not affected by the host crystal symmetry or host element type.

In addition to direct f→f transitions, 4f→5d transitions and charge-transfer states

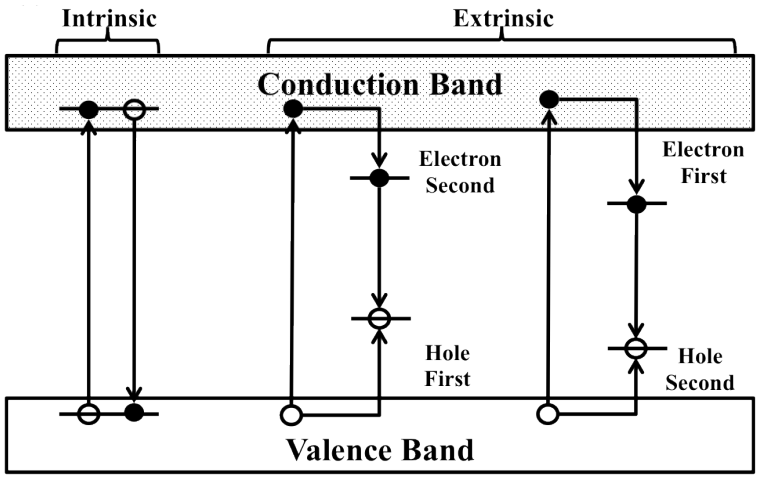

Figure 1.1 Energy levels for various band-to-band luminescent transitions. ○-holes, ●-electrons, adapted from Vij[7].

(CTS) can occur.[9] The 4f→5d transitions are different from the f→f transitions discussed earlier in that the electron must be promoted to a different orbital level. Charge-transfer states occur when an electron in a neighboring anion is transferred to a 4f orbital of the rare-earth activator. Both of these situations are allowed and result in greater optical adsorption since they require energy to promote the electron to a higher energy level. The result of these affects is the potential for more photon emission as the electrons either fall from the 5d→4f orbital in the former case and/or release the energy adsorbed from the CTS to the ground level of the activator in the latter.[9]

Photoluminescent quenching can occur due to energy transfer at high dopant concentrations. When the distance between two dopant ions is sufficiently small (on the order of Angstroms), energy can transfer from an excited ion to a ground state ion.[9] When energy is transferred in this manner, relaxation via non-photonic emission mechanisms becomes more probable.[9] Promoting the traps and decreasing radiative energy relaxation in favor of other mechanisms are the primary consequences of quenching.[9] In addition to quenching, the energy transfer can occur between different types of activators and can result in augmented emission gains or losses. The effect of mixing dopant types will be investigated in this work and will be referred to as co-doping.[9]

The maximum spectral emission intensity depends on the crystal symmetry, crystal field strength, crystal lattice parameter, dopant size, and dopant concentration[7,10]. Because PL depends on the interaction of the host crystal with the dopant strong crystal fields tend to produce longer wavelength light[1-5,7,8,10]. For each material system there is a

dopant concentration where an optimum overlap of the dopant and host orbitals produce the maximum emission intensity[5-7,10].

Ceramic phosphors have been used in the form of bulk materials, thin films and particles. The research presented in this document focuses on ceramic phosphor particles. Particle size can affect the emission spectra the particles[5,7]. As stated above, the PL process is affected by crystal field strength and symmetry as well as dopant size. A dopant atom much smaller or larger than the host atom can induce lattice strain. Crystal field strength, symmetry and strain all can be affected by lattice defects. Since defect formation and annihilation can be affected by the existence of nearby surfaces, interfaces or grain boundaries, the PL of ceramic phosphor powders is likely to depend on the particle size of the powder. In very small particles, on the order of tens of nanometers, electrons and holes can encounter quantum confinement, which can result in an increased band gap[7,8,10]. The change in the host material's band gap changes the electronic structure, and could lead to optical properties different than those of the bulk material. Size phenomena have been well documented in CdSe nanoparticles. The emission spectrum of CdSe particles shifts from blue to red with increasing particle size[7,11,12]. Similar changes are expected in the emission spectrum in nanoscale ceramic phosphors.

Motivation

Feldman and coworkers at Vanderbilt University demonstrated that the PL emission intensity of CdSe nanoparticles decreased up to four orders of magnitude with exposure to 7.5×10^{14} 1 MeV protons/cm^2 and that the decrease was dependent on particle size (unpublished). The ability to damage the particles and use their emission intensity to

indicate radiation exposure is encouraging. However, the instability of CdSe would limit their widespread use as a radiation exposure indicator, especially in extreme temperatures and in corrosive environments.

Like CdSe particles, the PL of oxide-based ceramic phosphors should be sensitive to radiation-induced damage. Radiation-induced defects could cause changes in PL emission intensity, emission wavelength or decay time. If radiation-sensitive PL is observed, oxide-based ceramic phosphors could be useful for radiation detection, and their chemical inertness and high temperature stability would enable them to be deployed in a wide variety of situations.

Synthesis of Ceramic Oxide Phosphors

Sol-gel[6,7,13-16], co-precipitation[7,17,18], hydrothermal[7,10,19], ultrasonic spray pyrolysis[20] and condensed phase[21] or solution phase combustion synthesis[22-25] are a few of the techniques used to synthesize oxide-based ceramic powders. We have chosen to concentrate on solution phase combustion synthesis (CS), as it is a self-propagating reaction that can provide the heat necessary for crystallization upon ignition. Solution combustion synthesis is a reaction between metal nitrates and an organic fuel in an aqueous solution that ignites a combustion to produce an airy polycrystalline solid with grain sizes in the range of 15-60 nm.[15,25-30]

Combustion synthesis combines an oxidizer and a fuel to provide the energy needed for the oxide to form and crystallize. CS uses nitrate ions as the oxidizer and an organic compound as the fuel. Common fuels include but are not limited to urea, carbohydrazide, glycine and citric acid. The fuel to oxidizer ratio of a given reaction is based off the fuel

to oxidizer ratio as described in Equation 1.1[31]. In Equation 1.1 note that the coefficients refer to those of a specific stoichiometric ratio, oxygen is considered the only oxidizing agent and nitrogen is neutral. The fuel to oxidizer ratio will be 1 for stoichiometric reactions, which will result in the maximum amount of energy evolved.

$$\Phi_e = \frac{\Sigma(coefficient\ of\ oxidizing\ elements)x(valency)}{(-1)\Sigma(coefficient\ of\ reducing\ elements)x(valency)} \qquad \text{Eq. 1.1}$$

Fuel selection can have a significant impact on the combustion characteristics. Poor chemical coordination between the fuel and other reactants used can be the difference between a successful and a failed combustion. The importance of the other reactants should not be understated as they can also play a role in combustion effectiveness. Reactants can begin to degrade as the solution is first dehydrated and then heated to the ignition point of the reaction. Degradation of the metal nitrate or the carbonaceous fuel can result in the ignitions of a non-stoichiometric reaction, reducing the amount of energy released. The reduced energy release would affect the product composition, crystallinity and yield.

Fuel selection for the combustion syntheses of YAG with pure fuels like urea, glycine, citric acid, carbohydrazide and hydrazine has been investigated. Each fuel has different combustion characteristics. For instance, combustion with urea produces a high flame temperature while citric acid does not. However, citric acid has been hypothesized to act as a chelating agent, potentially encouraging even dopant distribution in the final product. Literature reports the effect of mixing glycine and urea by Laishram and coworkers and Gupta and coworkers[32,33]. Both groups showed that by mixing glycine and

urea pure YAG could be formed directly from synthesis, which was not possible with either pure fuel[32,33]. These improvements suggest that mixing fuels can change combustion characteristics, motivating the need to investigate other mixed fuel combinations.

The use of a urea and citric acid mixture in CS has not been previously reported. This mixture could leverage the high flame temperature of the urea combustion along with the coordinating affects of citric acid. If mixing the two fuels produces crystalline material with a more even dopant distribution, the need for post-synthesis processing could be removed, saving time and energy. Additionally, uniformly doped material should exhibit optimal PL characteristics for that material.

Thermal degradation of reactant molecules has been studied indirectly through optimization of PL characteristics by changing the combustion furnace temperature. Optimum furnace temperature varies dependent on fuel, material system of interest and experimental reaction vessel. The case where the fuel and material system are the same but optimum furnace temperature changes indicates another mechanism is affecting the combustion. One possible explanation is reactant degradation but requires further investigation to understand why furnace temperature can change the final product when the reactants are the same, in the same proportions.

Approach

Despite the issues with combustion synthesis, it can be an effective method for oxide-based ceramic synthesis. To enable investigations of radiation effects on oxide powders, the synthesis and post-processing needs to be able to produce the same material

batch to batch. Optimizing the process for maximum photoluminescent intensity should not only produce the desired material, but should also provide insight into why the process produces that material. To these ends, combustion syntheses will be examined on two levels: typical lab scale batches (~5mL) and small thermogravimetric/differential scanning calorimetry batches (~25μL).

Providing the desired material for radiation studies was the main goal for optimizing the lab scale process. Characterization of the materials was used to guide decisions on how to improve the process. The characterization techniques included x-ray diffraction for crystallographic studies, x-ray photoelectron spectroscopy for chemical bonding environment studies, high-resolution transmission electron microscopy for morphology, crystallinity and compositional analyses, and photoluminescent spectroscopy as the performance metric.

The syntheses performed in the TGA/DSC provided both quantitative and qualitative insight to the reaction mechanisms through observation of mass loss and heat flow during the reaction. The device used for the reaction measures both thermogravimetric (mass loss) and calorimetric (heat flow) changes of the sample volume that cannot be measured during lab scale reactions. The insight from the thermogravimetric and calorimetric techniques coupled with transmission electron micrographs of the material produced on the small scale provided insight into the lab scale reaction. A better understanding of the combustion synthesis process was gained through the use of both techniques. The improved understanding could eventually help improve understanding of radiation damage mechanisms.

Characterization Techniques

In materials synthesis appropriate techniques must be used to ascertain whether the desired material is produced and if not estimate how the process needs to be changed and then verify if that change created the desired product. Multiple techniques must be used to fully understand a material system. This work used the techniques described below.

X-ray Diffraction

Powder x-ray diffraction (XRD) creates constructive and destructive interference following Bragg's law.[34] Bragg's law can be expressed as shown in Equation 1.2 where d is the spacing between planes in the crystal, λ the energy of the x-rays and θ the angle of incidence and exit commonly referred to as the Bragg angle. The Bragg angle is that which maximizes the intensity of the exiting x-rays due to constructive interference. These variables are shown schematically in Figure 1.2.

$$2dsin\theta = \lambda \qquad \text{Eq. 1.2}$$

To obtain a diffraction pattern, the incident x-ray angle and detector angles are changed equally, resulting in a diffraction pattern as a function of 2θ. From the schematic in Figure 1.2, 2θ represents the angle of entrance and exit, where θ is the Bragg angle. Knowing θ and λ allows for the calculation of d, after which the crystal planes present in the sample can be estimated for crystal identification. From Figure 1.2 it is apparent that if the atoms in a material are not organized with long-term order, or amorphous, Bragg

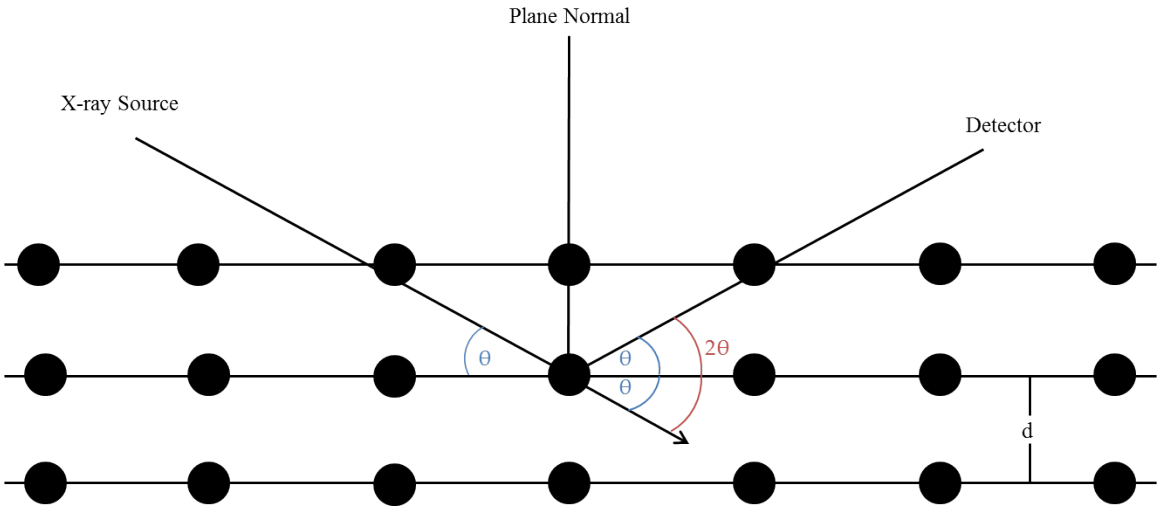

Figure 1.2. Experimental geometry of the x-ray interaction for constructive interference in a crystal- Bragg diffraction.

diffraction will not occur. The scattering from amorphous material contributes to the background, usually with relatively low intensity compared to peaks created from Bragg scattering.

When dealing with powder XRD, the powders are considered to be randomly oriented with no preference for a specific crystal plane. The advantage of using randomly oriented crystalline planes is that the peak intensity ratios from the various planes for a given material should be relatively constant. Thus the relative peak intensities for the various planes are comparable from sample to sample to help identify the desired crystal and peaks present due to undesired crystalline material.

X-ray powder diffraction was conducted using a Scintag X_1 θ/θ automated powder x-ray diffractometer with a Cu target, a Peltier cooled solid-state detector, and a plastic sample support. The XRD patterns were compared to the JCPDS files 33-0040 for YAG, 33-0041 for yttrium aluminum perovskite (YAP, $YAlO_3$), 34-0368 for yttrium aluminum monoclinic (YAM, $Y_4Al_2O_9$), 38-0222 for the $YAlO_3$ material with a cubic garnet structure (YAC) and 16-0277 for YBO_3.[35]The work of Sim[36] and Caponetti[37] was used to identify the yttrium aluminum hexagonal (YAH, $YAlO_3$) phase.

X-ray Photoelectron Spectroscopy

X-ray photoelectron spectroscopy is a technique that utilizes soft x-rays to produce low energy photoelectrons that provide information about the chemical bonding environment. The x-rays (Al Kα=1486.6 eV, Mg Kα=1253.6 eV) penetrate deep into the sample of interest but only the electrons near the surface escape the sample without

losing their characteristic energy. The information depth is approximately 3-15nm depending on the energy of the electron and take-off angle used for the analysis.

In XPS, the x-ray knocks an electron from its orbital in the target atom and is ejected from the sample. The binding energy (BE) of the electron is described Equation 1.3 where E_B is the BE in eV, E_K is kinetic energy of the ejected electron in eV, hν is the energy of the x-ray in eV, and Φ is the work function of the spectrometer in eV.[38,39]

$$E_B = h\nu - E_K - \Phi \qquad \text{Eq. 1.3}$$

XPS peaks provide elemental identification and information on the local chemical bonding environment of the element. XPS can also provide quantitative compositional data. Shifts in BE position for a single elemental transition can indicate a change in the local atomic environment. The peak shifts give insight into how the electrons are being influenced by neighboring atoms.

The sensitivity limit for XPS analyses is roughly 0.1 atomic percent. Handbooks and literature are used to identify peaks. To quantify the composition of the material in the analysis area, the area under each are used with sensitivity factors in Equation 1.4 where C_A is the atomic percentage of element A, I_i is the area of the transition for element i and S_i is the sensitivity factor for element i.

$$C_A = \frac{\frac{I_A}{S_A}}{\sum i \frac{I_i}{S_i}} \qquad \text{Eq. 1.4}$$

S_A will be a function of an the spectrometer and analysis conditions used. To perform accurate quantitative work it is important to have known standards from which sensitivity factors for those materials can be defined.

The surface sensitivity of XPS is a function of the geometry between the sample and the detector and the escape depth of the ejected electron. A schematic of three angle positions and electron origin are shown in Figure 1.3. As the angle between sample-normal and the detector is reduced, electrons originating from deeper in the sample are able to enter the detector. As the angle is increased, only electrons from nearer the surface can enter the detector. Thus to obtain more surface sensitive information from flat surfaces the angle should be large. The downfall to using a large angle is the photoelectron yield goes down, so to get good signal to noise ratio takes longer. Being able to leverage the origin of the photoelectrons has been used in the literature to create non-destructive depth profiles of thin films and has been shown as a method for modeling core-shell nanoparticle structure.[40,41]

A similar methodology is used to determine overlayer thicknesses. An overlayer could be a layer of material unlike that of the substrate of interest, and is often something such as a surface oxide or carbon contamination. This method has been routinely used to calculate the thickness of ultra-thin silicon oxide layers on silicon. The advantage of this technique is that it can provide both bonding information and thickness information where spectroscopic ellipsometry, another often used thin film measurement technique, becomes inaccurate for films below ~2nm thick.[42] Equation 1.5 is used to calculate overlayer thickness, d, where λ_{IMFP} is the inelastic mean free path, θ is the angle between sample normal and the analyzer, I_A and I_B are the intensities of the XPS peak of the

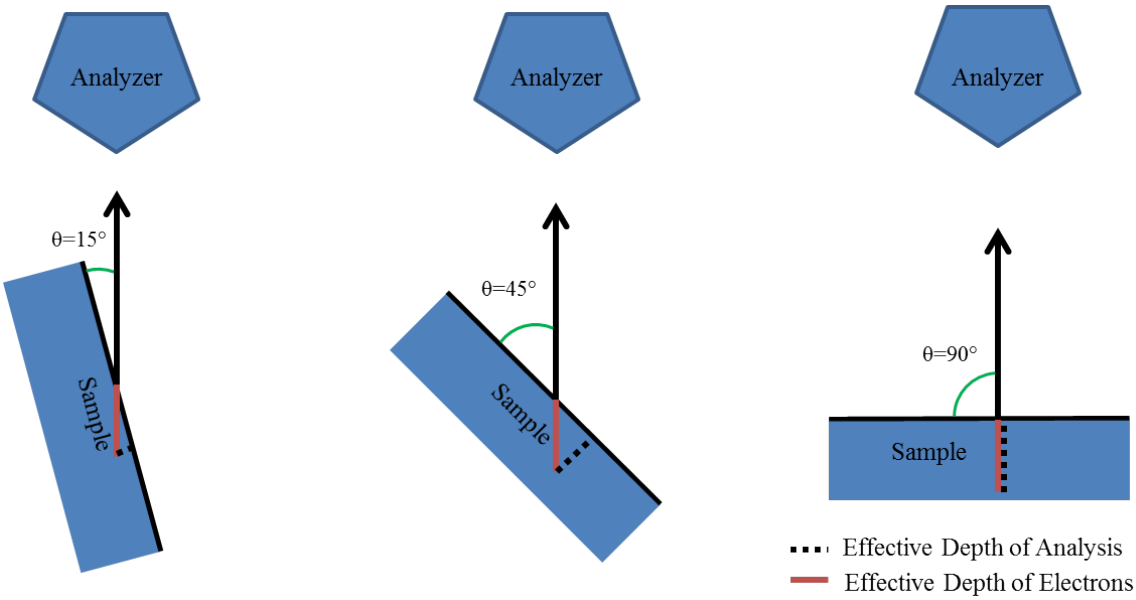

Figure 1.3. The effect of changing the angle between sample normal and the analyzer on the effective depth of analysis for XPS.

overlayer and substrate, respectively, and S_A and S_B are the sensitivity factors of the overlayer and substrate, respectively. Note that Cumpson and coworkers have demonstrated that the attenuation length is a better estimate for thickness than the IMFP alone due to elastic scattering effects that the IMFP ignores.[43]

$$d = \lambda_{IMFP} cos\theta \ln\left(1 + \frac{(I_A/S_A)}{(I_B/S_B)}\right) = \lambda_{IMFP} cos\theta \ln\left(1 + \frac{R_{Expt}}{R_o}\right) \qquad \text{Eq. 1.5}$$

Transmission Electron Microscopy

Transmission electron microscopy (TEM) uses high-energy electrons passing through a very thin sample to image the microstructure of the sample. Electrons passing through the material can be scattered by the host material, creating electron diffraction that can be analyzed to determine crystallinity similar to XRD analyses.

The high-energy electrons can also be used to determine the composition of the sample. The electrons can excite electrons in the sample. The excited electrons must release the excess energy before they can relax. The excess energy can be released in many ways, one of which is to emit an x-ray. The energy of the x-ray is characteristic of the atom from which it originated. Energy dispersive x-ray spectroscopy (EDS) is the analysis of the x-ray energy to determine the sample's composition.

High-resolution TEM images and EDS maps were obtained using a Tecnai Osiris operating at 200 kV. Samples were prepared by drop-casting particle suspensions onto ultrathin carbon-coated TEM grids. Drift-corrected EDS spectral images were acquired using approximately 0.6 nA of beam current and a pixel dwell time of 5 seconds. Data collection and analysis were performed using the TEM Imaging & Analysis software

(FEI). The electron microscopy work done in this dissertation was all performed by Dr. James McBride who gave guidance to best acquisition practices and provided the analyses.

Rutherford Backscattering Spectroscopy

Rutherford backscattering spectrometry (RBS) is a non-destructive depth profiling technique that can determine atomic ratios in thin films and bulk materials. Simple billiard ball physics is often used to describe the particle-target interactions of RBS. RBS measures the effect of backscattering a particle beam, typically He^{+} or He^{++}, of known energy off a solid target. The interaction is considered to be elastic and the energy of the backscattered particle depends on the target atom. This process occurs for all interactions in the sample volume. The sample volume is the projected area of the incident beam times the depth of backscattered particles and interactions are occurring on a per area basis. Thus, the RBS experimental technique effectively measures the areal density of the target atoms and can accurately estimate the stoichiometric ratio of species in the target. An example of and RBS experimental geometry is shown in Figure 1.4 where the incident particle is at energy E_0 and the backscattered particle is at energy E_1. Note the angles involved are referenced to the incident particle angle, θ_1, which is typically normal to the sample.

The kinematic factor is a measure of the energy lost in the interaction between the incident particle and target atoms and is defined in Equation 1.6 where M_i is the mass of element *i,* and θ is the experimental angle as defined in Figure 1.4.[44] The kinematic factor relationship shows that at small masses the energy separation will be greater than at large

masses. The kinematic factor can be used to help identify elements present in the film by using the kinematic factor and the simple relationship for the energy of a backscattered surface element, $E_1=KE_o$[44], which can then be correlated to channel number through use of an appropriate standard.

$$K = \left[\frac{(M_2^2 - M_1^2 sin^2\theta)^{1/2} + M_1 cos\theta}{M_1 + M_2}\right]^2 \quad \text{Eq. 1.6}$$

The peak intensity is described by the Rutherford cross section of the interaction between the incident and target particles. The Rutherford cross-section, σ_R, is provided in Equation 1.7 where Z_i is the atomic number of atom i, E is the experimental energy of the projectile, θ is the angle of the detector as defined by θ_2 in Figure 1.4 and M_i is the atomic mass of element i. Equation 1.7 shows that large target atoms will produce a larger cross-section, resulting in more total interactions. Atoms with higher cross sections produce higher relative signal intensity compared to atoms with smaller cross sections. Using the ratios of σ_R for the elements in a film can be used with the ratio of front edge heights, H_0, to estimate the ratio of the atoms present in the film, m/n, as shown in Equation 1.8. Effects of the ratio of the stopping cross section powers, $[\varepsilon]^{AB}{}_A/[\varepsilon]^{AB}{}_B$, is typically set to one as the ratio seldom departs from one by more than a few percent.[44]

$$\sigma_R(E,\theta) \cong 0.02073 \left(\frac{Z_1 Z_2}{4E}\right)^2 \left[sin^{-4}\left(\frac{\theta}{2}\right) - 2\left(\frac{M_1}{M_2}\right)^2\right] \quad \text{Eq. 1.7}$$

$$\frac{m}{n} = \frac{N_A}{N_B} = \frac{H_{A,0}^{AB}}{H_{B,0}^{AB}} \frac{\sigma_B}{\sigma_A} \frac{[\varepsilon_0]_A^{AB}}{[\varepsilon_0]_B^{AB}} \quad \text{Eq. 1.8}$$

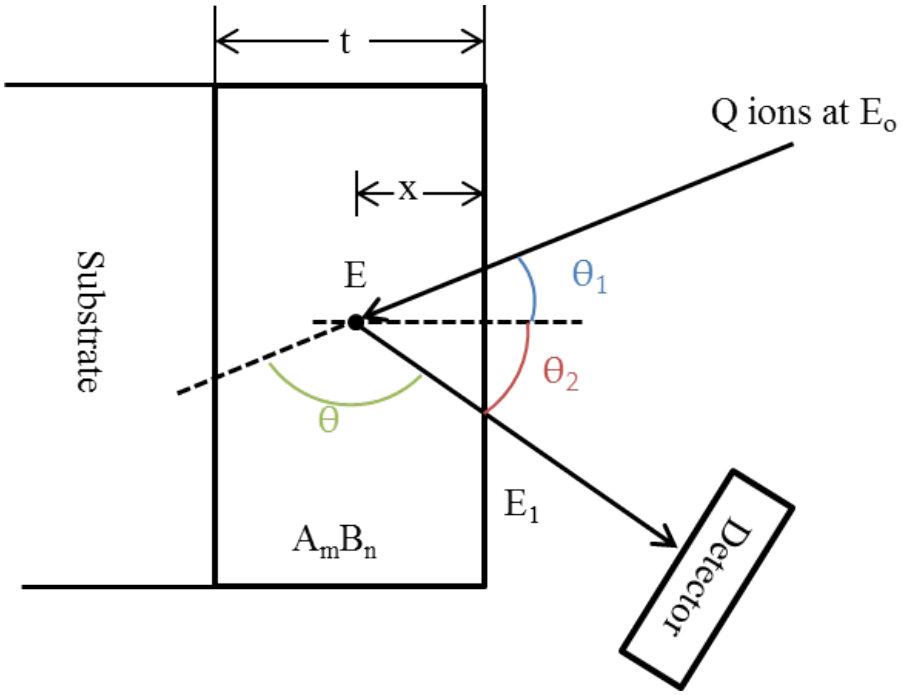

Figure 1.4. Typical experimental geometry for an RBS experiment.

Depth resolution of RBS is influenced by the angle of the detector, with the poorest depth resolution at θ_2=180° and increasing resolution as θ_2 decreases. Studies that use small θ_2 are known as glancing angle studies and can decrease the depth resolution from 20-25nm to 8-12 nm. Depth resolution is limited in RBS because of the increasing energy loss in solids as the projectile and backscattered particle have to traverse more material. In other words, the thicker the material and the longer the particle is in the material, the probability will increase that energy will be lost or other scattering effects encountered. This also means that depth resolution becomes poorer the deeper the interaction occurs.

Calculations of areal density depend on the experimental setup and acquisition settings as shown in Equation 1.9, using Figure 1.4 as a reference. Equation 1.9 is a mathematical description of how the areal density of atom *i*, $(Nt)_i$, relates to the area of the peak, A_i, experimental geometry, θ, charge collected, Q, detector solid angle, Ω, Rutherford cross section, σ_i, and incident particle energy, E. Areal density ratios can be used to find the atomic ratios similar to the peak height method. Once Ω is known via analysis of a known standard, Equation 1.10 can be written to take into account the detector dead time ratio, DTR, effects of non-Rutherford cross sections, σ/σ_R, and a correction factor for a standard sample, C_{Bi}. The corrections are small but useful if a standard is not available for every analysis.

$$(Nt)_i = \frac{A_i cos\theta}{Q\Omega\sigma_i(E,\theta)} \qquad \text{Eq. 1.9}$$

$$(Nt)_i = \frac{A_i \cdot DTR \cdot cos\theta \cdot C_{Bi} \cdot e}{Q\Omega\sigma_R^i(E,\theta)\left(\frac{\sigma}{\sigma_R}\right)_i} \qquad \text{Eq. 1.10}$$

RBS was not a good technique to analyze the oxide-based ceramic particles synthesized for this work. When pressed or dropcast, the particles create a rough surface that scattered the primary particles which skewed the data such that it could not be analyzed. Irradiation experiments were performed in the RBS end station of beamline 6SDH, a NEC Pelletron tandem accelerator equipped with an Alphatross ion source, at Vanderbilt University. Experiments were conducted 1.0 MeV H^+ incident particles up to a total fluence of 5e15 protons/cm^2.

Thermogravimetric Analysis/Differential Scanning Calorimetry

Thermogravimetric analysis (TGA) is the study of material decomposition as a function of temperature. Simply put, the mass of a sample is tracked as a function of temperature using a balance located inside a furnace. Differential scanning calorimetry (DSC) measures the change in heat flow to the sample as a function of temperature. Together TGA and DSC provide complementary information about how a material reacts as a function of temperature. Due to the simplicity of TGA only a detailed explanation of DSC will be provided.

DSC monitors the heat needed to achieve a temperature change in the sample of interest against that of a reference sample. The temperature difference indicates differences in heat capacity, C_p, of the sample of interest and reference sample. Chemical reactions and phase transitions can provide a dramatic change in heat capacity by either releasing or absorbing heat, requiring less or more heat to achieve the temperature change, respectively.

DSC resolution is limited when trying to analyze multiple thermal events close together. Because DSC is attempting to achieve a temperature program, here a constant temperature rise, events that disrupt the constant ramp rate are accounted for by adding more or less heat for endo or exothermic events, respectively. As the ramp rate increases, the demand for heat compensation for endo or exothermic events is greater and recovering from such events takes longer. The added time needed to correct for thermal events at high ramp rates results in broader peaks in the data. For experiments with multiple thermal events, such as in combustion synthesis, the broader peaks run together and result in poor thermal event resolution as a condition known as thermal lag.

TGA and DSC analyses for experiments in Chapter 3 were conducted using a TA Instruments Q600. Argon purge gas was flowed in the system at 10mL/min. The instrument was calibrated to sapphire for heat flow and reference weights over our temperature range for each heat rate chosen. Exothermic events are shown in the positive heat flow direction for all DSC data presented. Heating ramp rates tested were from 2-100ºC/min.

Photoluminescence Spectroscopy

Photoluminescence (PL) spectroscopy is the measurement of the photon emission from photoluminescnet materials. The sample is irradiated with excitation photons and the emitted signal is characteristic of the host material and dopant type and concentration. Measurements were taken with an Avantes 2048 USB2 spectrometer. A xenon light source and Newport Oriel 130 1/8 monochromator provided the excitation. The monochromated light then passed through one leg of a bifurcated fiber optic cable to an

x-y translation sample stage. This leg of the bifurcated cable receives light reflected off of and emitted from the sample in addition to transmitting the excitation light. The sample stage was adjusted to maximize the emission intensity and minimize the reflected excitation peak before spectra were acquired. Sarah Gollub performed all PL acquisitions.

Powders were pressed into a ~1mm deep, 2.5mm diameter hole drilled in a 1cmx1cmx2.5mm aluminum sample holder. The pressed powders were blown off with 20 psi nitrogen to remove any loose particles.

References

[1] K. Du, J. Biesenbach, D. Ehrlichmann, U. Habich, U. Jarosch, J. Klein, P. Loosen, J. Niehoff, and R. Wester, Opt Quant Electron **27**, 1089 (1995).
[2] F. Li, J. West, A. Glushchenko, and C. Cheon, Journal of the Society of Information Display **6**, 523 (2006).
[3] D.-S. Xing, M.-L. Gong, X.-Q. Qiu, D.-J. Yang, and K.-W. Cheah, Mater Lett **60**, 3217 (2006).
[4] Y. Shimomura, T. Honma, M. Shigeiwa, T. Akai, K. Okamoto, and N. Kijima, J Electrochem Soc **154**, J35 (2007).
[5] P. Holister, J. Weener, and C. Vas, Technology White Papers Nr. 3 (2003).
[6] M. Veith, S. Mathur, A. Kareiva, M. Jilavi, M. Zimmer, and V. Huch, J Mater Chem **9**, 3069 (1999).
[7] D. Vij, *Luminescence of Solids* (Plenum Pub Corp, 1998).
[8] C. Feldmann, T. Jüstel, and C. Ronda, Adv Funct Mater **13**, 511 (2003).
[9] S. Shionoya, W.M. Yen, and T. Hase, (1999).
[10] A. Lakshmanan, *Luminescence and Display Phosphors* (Nova Science Pub Inc, 2008).
[11] D. Norris and M. Bawendi, Phys. Rev. B **53**, 16338 (1996).
[12] B. Dabbousi and J. Rodriguez-Viejo, J. Phys. Chem. **101**, 9463 (1997).
[13] D. Jia, Y. Wang, X. Guo, K. Li, Y.K. Zou, and W. Jia, J Electrochem Soc **154**, J1 (2007).
[14] D. Klimm, S. Ganschow, and A. Pajączkowska, Journal of Alloys and … **436**, 204 (2007).
[15] L. Yang, T. Lu, H. Xu, W. Zhang, and B. Ma, J. Appl. Phys. **107**, (2010).
[16] Y. Wu, S. Parola, O. Marty, M. Villanueva-Ibanez, and J. Mugnier, in *Opt Mater* (2005), pp. 1471–1479.
[17] J. Nair, P. Nair, E. Doesburg, J.G. Van Ommen, and J. Ross, Journal of Materials … 4517 (1998).
[18] C.-C. Chiang, M.-S. Tsai, and M.-H. Hon, J Electrochem Soc **155**, B517 (2008).
[19] M. Nyman, L.E. Shea-Rohwer, J.E. Martin, and P. Provencio, Chem. Mater. **21**, 1536 (2009).
[20] Y. Kang, I. Lenggoro, S. Park, and K. Okuyama, Mater Res Bull **35**, 789 (2000).
[21] S. Aruna and A.S. Mukasyan, Current Opinion in Solid State and Materials … **12**, 44 (2008).
[22] L.E. Shea, J. McKittrick, O.A. Lopez, and E. Sluzky, J Am Ceram Soc **79**, 3257 (2005).
[23] N.A. Dhas and K.C. Patil, J Mater Chem **3**, 1289 (1993).
[24] S. Roy, L. Wang, and W. Sigmund, Mater Lett **39**, 138 (1999).
[25] N. Orlovskaya, Y. Chen, N. Miller, H. Abernathy, D. Haynes, D. Tucker, and R. Gemmen, Adv Appl Ceram **110**, 54 (2011).
[26] J. Li, Y. Pan, F. Qiu, Y. Wu, W. Liu, and J. Guo, Ceramics International **33**, 1047 (2007).
[27] R.K. Lenka, T. Mahata, P.K. Sinha, and A.K. Tyagi, J Alloy Compd **466**, 326 (2008).
[28] O. Ozuna, G. Hirata, and J. McKittrick, J Phys-Condens Mat **16**, 2585 (2004).
[29] E.J. Bosze, J. McKittrick, and G.A. Hirata, Materials Science and Engineering: B **97**, 265 (2003).

[30] Y. Tong, J. Zhu, L. Lu, X. Wang, and X. Yang, J Alloy Compd **465**, 280 (2008).
[31] L.E. Shea, J. McKittrick, O.A. Lopez, and E. Sluzky, J Am Ceram Soc **79**, 3257 (1996).
[32] K. Laishram, R. Mann, and N. Malhan, Ceramics International **37**, 3743 (2011).
[33] K.V.K. Gupta, A. Muley, P. Yadav, C.P. Joshi, and S.V. Moharil, Appl. Phys. B **105**, 479 (2011).
[34] Y. Waseda, E. Matsubara, and K. Shinoda, *X-Ray Diffraction Crystallography* (Springer, 2011).
[35] O. Yamaguchi, K. Matui, and K. Shimizu, Ceramics International **11**, 107 (1985).
[36] S.M. Sim, K.A. Keller, and T.I. Mah, J Mater Sci **35**, 713 (2000).
[37] E. Caponetti, M.L. Saladino, F. Serra, and S. Enzo, J Mater Sci **42**, 4418 (2007).
[38] J.F. Moulder, W.F. Stickle, P.E. Sobol, and K.D. Bomben, (1995).
[39] D. Briggs and J.T. Grant, *Surface Analysis by Auger and X-Ray Photoelectron Spectroscopy* (2003).
[40] P. Nachimuthu, S.D. Techane, and D.G. Castner, Analytical and … (2010).
[41] G. Zorn, S.R. Dave, X. Gao, and D.G. Castner, (2011).
[42] H.G. Tompkins and W.A. McGahan, *Spectroscopic Ellipsometry and Reflectometry* (Wiley-Interscience, 1999).
[43] P. Cumpson and M. Seah, Surf Interface Anal (1997).
[44] J.R. Tesmer and M.A. Nastasi, *Handbook of Modern Ion Beam Materials Analysis* (1995).

CHAPTER II

UREA/CITRIC ACID MIXED FUEL COMBUSTION SYNTHESIS OF YAG:CE PARTICLES

Introduction

Oxide-based ceramic phosphors have been used in televisions, LED's, and as laser sources[1-5]. Yttrium aluminum garnet (YAG) and lanthanum zirconate (LZO) are two such oxide-based phosphors that luminesce when doped with rare-earth metals. Recent work at Vanderbilt by the Walker and Rogers research groups has shown that the emitted photoluminescent (PL) spectrum of proton irradiated LZO particles differs from that of non-irradiated LZO particles[6], suggesting these materials may be used in radiation detection. Phosphors with intense photoluminescence are desired to facilitate detection of PL intensity changes or spectral shifts due to radiation exposure.

The synthesis of the phosphors must controllably produce materials with consistent properties to enable us to identify the effects of the radiation damage and to determine damage mechanisms. Sol-gel[7-11], co-precipitation[12,13], hydrothermal[14], ultrasonic spray pyrolysis,[15] and condensed phase[16] or solution phase combustion synthesis[17-20] are a few of the techniques used to synthesize oxide-based ceramic powders. We have chosen to concentrate on solution phase combustion synthesis (CS). Solution combustion synthesis combusts an aqueous solution of metal nitrates and an organic fuel to produce an airy polycrystalline solid with grain sizes in the range of 15-60 nm.[10,20-25]

The fuel to oxidant ratio, type of fuel, pressure, and water content[26] are some of the parameters affecting solution phase combustion synthesis.[17,23,24,26] Deganello and coworkers studied the effects of the citric acid to metal nitrate ratio and solution pH on the crystal structure, phase, and morphology of perovskites produced by solution phase CS.[27] They found that using a stoichiometric fuel to oxidant ratio provides the most vibrant combustion, but that varying the fuel to oxidant ratio can cause cerium oxide segregation in some material systems. The fuel to oxidant ratio also changed the morphology of the final material, with high fuel to oxidant ratios producing a coarser microstructure than low fuel to oxidant ratios. They conclude that the optimal citric acid to nitrate ratio for combustion synthesis strongly depends on the desired product..

We have observed that crystallinity of YAG and LZO produced from solution phase CS strongly depends on the fuel used, as shown in Figure 2.1. As-synthesized YAG produced using urea (Figure 2.1a) produces an x-ray diffraction pattern indicative of crystalline YAG. After a two-hour 900ºC heat treatment in air the diffraction pattern remains nearly identical. As-synthesized YAG produced using glycine (Figure 2.1b) produces an x-ray diffraction pattern indicative of amorphous material. After a two-hour 900ºC heat treatment the diffraction pattern contains peaks indicative of YAG and yttrium aluminum hexagonal(YAH) phases. LZO as synthesized from glycine produces an x-ray diffraction pattern indicative of crystalline pyrochlore LZO. After a two-hour 900ºC heat treatment the diffraction pattern remains identical to that produced by the as-synthesized material. LZO as synthesized using urea produces an x-ray diffraction pattern indicative of amorphous material. After a two-hour, 900ºC heat treatment some

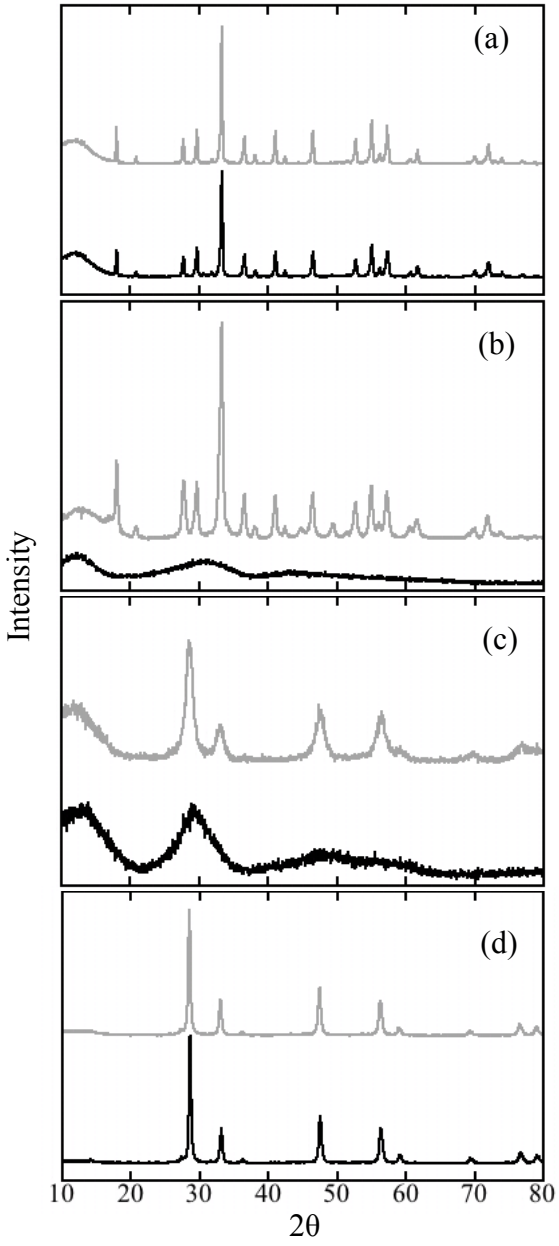

Figure 2.1. XRD spectra of as-synthesized (black) and 900 °C heat treated (grey) samples (a)YAG synthesized using urea, (b) YAG synthesized using glycine, (c), LZO synthesized using urea, and (d) LZO synthesized using glycine.

peaks consistent with lanthanum oxide and zirconium oxide phases appear in the x-ray diffraction pattern. Other researchers have also shown that formation of YAG and LZO phases and that the extent of post-synthesis heat treatment needed for crystallization can depend on the fuel used in solution CS.[18,20,28]

In this paper we report the results of studies on the effects of fuel composition (mixtures of urea and citric acid) and post-synthesis heat treatments (as-synthesized and two hours at 900ºC, 1000ºC or 1100ºC) on the physical, chemical and photoluminescent properties of solution combustion synthesized YAG:Ce1%. Mixing the fuels could provide the combustion conditions for optimal performance by providing a high flame temperature from the urea[28] with well-distributed dopant ions due to citric acid's chelating properties. [29,30] Some mixed fuel work using a variety of fuels for different systems has been reported. [31-35] YAG synthesis using a mixture of urea and glycine has been studied[36,37], but a systematic study of YAG synthesis using a mixture of urea and citric acid has not been reported. Our results suggest that crystallinity, grain size, and chemical composition do not explain the observed trends in photoluminescent emission.

Experimental Details

Material Synthesis

The process procedures used in this work were based on a variety of previously reported studies.[21,22,25,29] The metal nitrates and fuel [$Y(NO_3)_3 \bullet 6H_2O$ (Sigma Aldrich, 99.9%), $Al(NO_3)_3 \bullet 9H_2O$ (Sigma Aldrich, 99+%), $Ce(NO_3)_3 \bullet 6H_2O$ (Sigma Aldrich, 99.5%), urea (CH_4N_2O, Sigma Aldrich 99.0-100.5%), and citric acid (CA, $C_6H_8O_7$,

Sigma Aldrich ACS Reagent, ≥99.5%)] were mixed in stoichiometric ratios in a 50 mL high temperature crucible. The cerium dopant was added by pipetting an appropriate volume of a 0.199 M $Ce(NO_3)_3 \bullet 6H_2O$ aqueous solution. Five milliliters of deionized water (≥12.5 MΩcm) was then added to enhance mixing. The solution was then heated on an 80ºC hot plate, continuously stirring with a PTFE coated stir bar until a viscous solution was obtained. Mixing during dehydration is needed to uniformly distribute the dopant throughout the final product. The stir bar was removed and the crucible placed in a 600°C vented muffle furnace in air. The reaction was complete within 90 seconds after being placed in the furnace. Each batch was mixed to produce 0.003 moles of the nominally $Y_{2.97}Ce_{0.03}Al_5O_{12}$ (YAG:Ce1%) powder.

After cooling, the product was crushed into a powder using a mortar and pestle. Heat treatments were conducted in an air ambient at 900, 1000 and 1100 °C for two hours. Literature suggests that YAG crystallizes from amorphous YAG synthesized using citric acid at approximately 850ºC.[19,21,38,39] 1100ºC was the maximum capability of our furnace.

The urea and citric acid were mixed in ratios based on their appropriate reactions to form YAG. We will define the variable CA% as the amount of the YAG made with RXN2. A fuel mixture of X CA% contains 0.0667*X moles of citric acid and 0.20*(100-X) moles of urea. The fuels were mixed together and added to the other reactants before combustion.

$$3Y(NO_3)_3 + 5Al(NO_3)_3 + 20CH_4N_2O \rightarrow Y_3Al_5O_{12} + 20CO_2 + 40H_2O + 32N_2 \quad \textbf{RXN1}$$

$$3Y(NO_3)_3 + 5Al(NO_3)_3 + 6.67C_6H_8O_7 \rightarrow Y_3Al_5O_{12} + 40CO_2 + 26.67H_2O + 12N_2 \quad \textbf{RXN2}$$

XPS

X-ray photoelectron spectroscopy (XPS) data were collected using a Physical Electronics (PHI) VersaProbe 5000 equipped with a monochromatic Al Kα x-ray source. A 200 μm diameter, 50 W x-ray beam was used with a takeoff angle of 45° off sample normal. Charge neutralization was accomplished using 1.1 eV electrons and 10 eV Ar^+. Survey and high-resolution spectra were taken with pass energies of 187.85 eV and 11.75 eV, respectively. All spectra were energy normalized to carbon at 284.8 eV. Data reduction was performed using CasaXPS with PHI handbook sensitivity factors.[40] Peaks were fit using 70%-30% Gaussian-Lorentzian peaks with a Shirley background.

XRD

X-ray powder diffraction (XRD) was conducted using a Scintag X_1 *θ/θ* automated powder x-ray diffractometer with a Cu target, a Peltier cooled solid-state detector, and a plastic sample support. The XRD patterns were compared to the JCPDS files 33-0040 for YAG, 33-0041 for yttrium aluminum perovskite (YAP, $YAlO_3$), 34-0368 for yttrium aluminum monoclinic (YAM, $Y_4Al_2O_9$), and 38-0222 for the $YAlO_3$ material with a cubic garnet structure (YAC).[41] The work of Sim[42] and Caponetti[43] was used to identify the yttrium aluminum hexagonal (YAH, $YAlO_3$) phase.

PL

Photoluminescence (PL) measurements were taken with an Avantes 2048 USB2 spectrometer. A xenon light source and a Newport Oriel 130 1/8 monochromator

provided the excitation. The monochromated light then passed through one leg of a bifurcated fiber optic cable to an x-y translation sample stage. This leg of the bifurcated cable receives light reflected off of and emitted from the sample in addition to transmitting the excitation light. The sample stage was adjusted to maximize the emission intensity and minimize the reflected excitation peak before spectra were acquired.

To ensure the same areas were analyzed in both XPS and PL, the powders were pressed in an ~1mm deep, 2.5 mm diameter hole drilled in a 1cmx1cmx2.5mm aluminum sample holder. The pressed powders were blown off with 20 psi nitrogen to remove any loose particles.

Results and Discussion

PL Normalization

PL emission spectra can be affected by a series of both material and acquisition parameters. Since we are using PL as our performance metric, variation between PL spectra due to sample preparation and instrumental variations must be minimized. Figure 2.2 contains an example PL spectrum. The size of the reflected excitation peak will depend on the sample reflectivity, surface roughness, alignment of the fiber optic cable, sample preparation, and other variables. PL spectra were normalized by dividing the intensity at each wavelength by the integral under the reflected excitation peak to remove these non-material specific variations in the spectra.

Effect of mixing fuels on maximum PL

The maximum intensities of normalized PL spectra from materials synthesized in

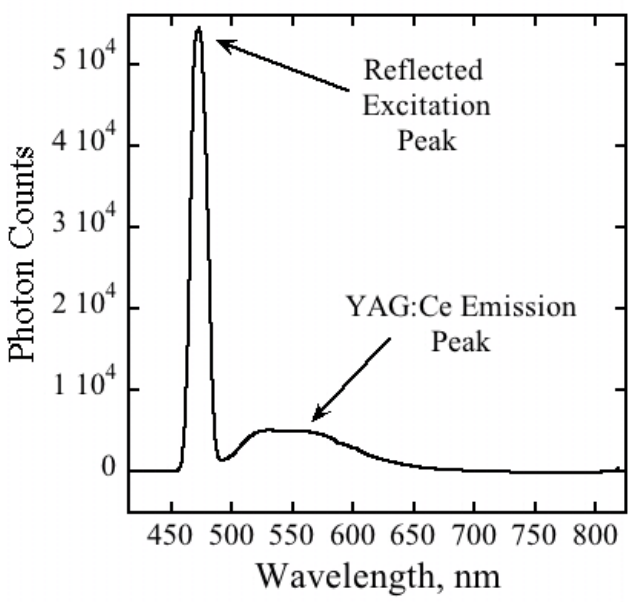

Figure 2.2. Photoluminescence emission spectrum collected from YAG:Ce1% using 470 nm excitation.

this study are plotted versus fuel mixture composition in Figure 2.3. Materials synthesized from the pure fuels (0 and 100 CA%) have the highest normalized PL for all materials that received a post-synthesis heat treatment. Only the material synthesized from pure urea (0 CA%) had a measureable PL without post-synthesis heat treatment. Maximum PL intensity increases with post-synthesis heat treatment temperature for all materials synthesized using citric acid. The PL of the 0 CA% case drops as the heat treatment increases to 1000 °C, then increases to have the overall maximum when heat-treated at 1100 °C. These PL measurements do not support our hypothesis that using a mixture of urea and citric acid would increase the photoluminescent intensity of YAG:Ce.

XRD

X-ray diffraction was used to compare crystallinity of the as-synthesized and heat treated YAG:Ce powders. Figure 2.4a presents the XRD patterns for as-synthesized powders as a function of fuel mixture composition. The as-synthesized powder produced using pure urea (0 CA%) contained YAG, YAP and YAC phases. Shoulders on the low 2θ side of the (420) and other major YAG peaks correspond to YAC[41] peaks. The as-synthesized powders produced using 25 and 35 CA% fuel mixtures were mostly amorphous with small amounts of the YAH phase. The as-synthesized powders made using 50 and 100 CA% were amorphous.

Figure 2.4b presents the XRD patterns for the powders after a 2 hour, 900ºC heat treatment. The diffraction patterns indicate that the heat-treated powders all contain YAG

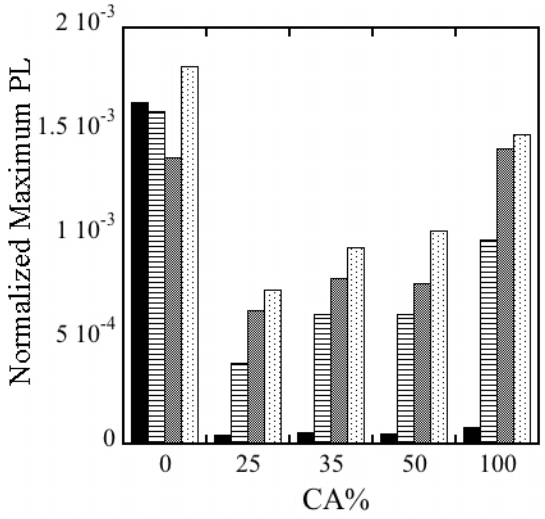

Figure 2.3. Maximum photoluminescence emission intensity of YAG:Ce1% spectra normalized by the integral of the reflectance peak as function of fuel mixture composition and two hour post-synthesis heat treatment: ■ as-synthesized, ▤ 900 °C, ▨ 1000 °C, ▩ and 1100 °C.

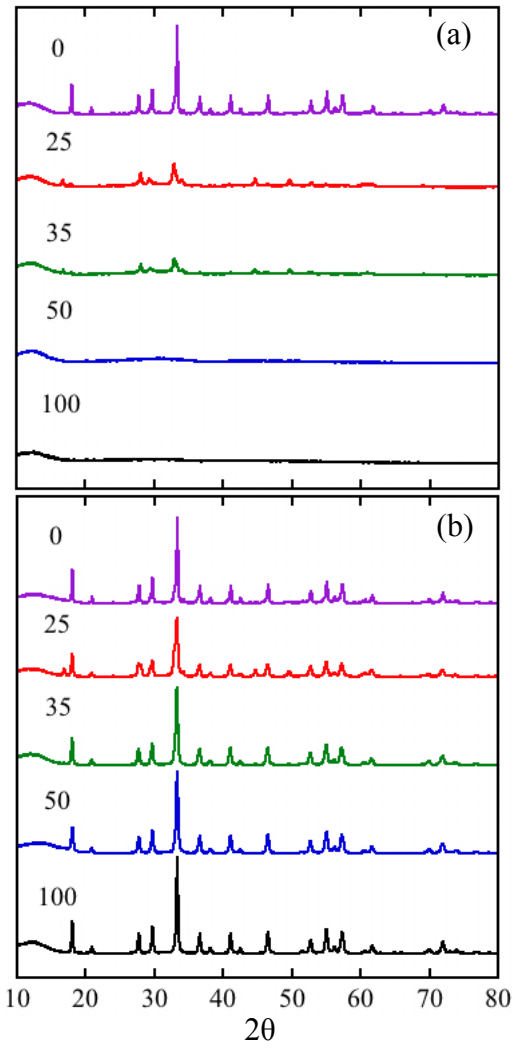

Figure 2.4. XRD spectra of YAG:Ce as a function of fuel mixture composition (a) as-synthesized and (b) after 900 °C, two hour post-synthesis heat treatment.

structure. The heat-treated powder produced using a 25 CA% fuel mixture also contains the YAH phase. YAP and YAC phases remain in the heat-treated powder produced using pure urea (0 CA%).

We used the Scherrer equation with a shape factor of 0.9 to estimate the grain sizes of the as-synthesized and heat-treated powders.[44] We used an average of the grain size determined from the YAG (210), (220) and (420) planes. Figure 2.5 plots the grain size of the as-synthesized and heat-treated powders as a function of fuel mixture composition. The error bars were generated from the standard deviation of the average grain size for multiple YAG/urea syntheses. The standard deviation was then turned into a percentage of the average for each heat treatment case then applied as the error bars. As shown in Figure 2.4a, as-synthesized powders produced using fuel compositions of 50 or 100 CA% were amorphous, and thus their gran sizes are 0 nm in Figure 2.5. The grain sizes of the YAG phase in as-synthesized powders increase with decreasing citric acid content in the fuel (lower CA%). In all cases the grain sizes of the as-synthesized powders increase with increasing heat treatment temperature. The powder produced using pure urea fuel (0 CA%) has the largest grains of all the similarly heat treated powders.

The range of 2θ around the YAG (420) peak also contains many of the major peaks for the YAP, YAH and YAC phases. Figure 2.6 shows the XRD peaks in the range $32 \leq 2\theta \leq 35$ for the (a) as-synthesized, (b) 900 ºC, and (c) 1100 ºC heat-treated powders produced from pure urea (0 CA%), pure citric acid (100 CA%), and from a 35 CA% fuel mixture. As shown in Figure 2.6a, the material made using pure urea contains the most YAG phase of the three as-synthesized materials. The shoulder on the low 2θ side of the

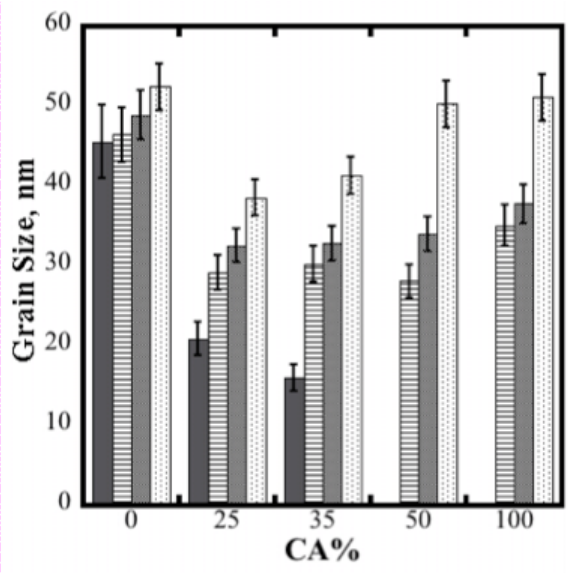

Figure 2.5. YAG:Ce powder grain sizes calculated using the Scherrer equation as functions of fuel mixture composition and post-synthesis heat-treatment temperature. ■ as-synthesized, ▤ 900°C, ▨ 1000°C, and ▩ 1100°C.

YAG peak is likely due to the presence of the YAC phase, while the peak at 2θ of 34.2 suggests the presence of the YAP phase. The as-synthesized material made with pure citric acid is amorphous (see Figure 2.4), and therefore contains no XRD peaks in this region. The XRD pattern of the as-synthesized material made with a 35 CA% fuel mixture contains the (102) and (004) peaks of the YAH[42] phase.

The XRD peaks in patterns acquired from all three samples heat-treated at 900 ºC for two hours shift toward the (420) YAG peak, as shown in Figure 2.6b, compared to their positions in the as-synthesized XRD patterns. The material produced from pure urea (0 CA%) contains the YAC and YAP phases present in the as-synthesized material. The relatively broad peak from the sample produced with a 35 CA% fuel mixture suggests the presence of both YAG and YAH phases. The relatively sharp peak from the material produced from pure citric acid (100 CA%) suggests that this sample contains only the YAG phase.

The shape of the XRD peaks in the $32 \leq 2\theta \leq 35$ range suggests that after heat-treating the samples at 1100 ºC for two hours (Figure 2.6c) all three of the materials contain primarily the YAG phase. The XRD pattern of the materials made from pure urea (0 CA%) suggests the presence of small amounts of YAP and YAC phases. The need to heat-treat for longer time or higher temperature to eliminate the YAP phase from YAG synthesized using pure urea has been reported.[42,45] Yamaguchi proposes that the YAC phase begins to transition into the YAG phase between 1080 and 1200ºC.[41] Our observations are consistent with these results.

If differences in grain size, crystal phase, and/or the extent of mixed phases present in the YAG:Ce powders were the causes of differences in their photoluminescent

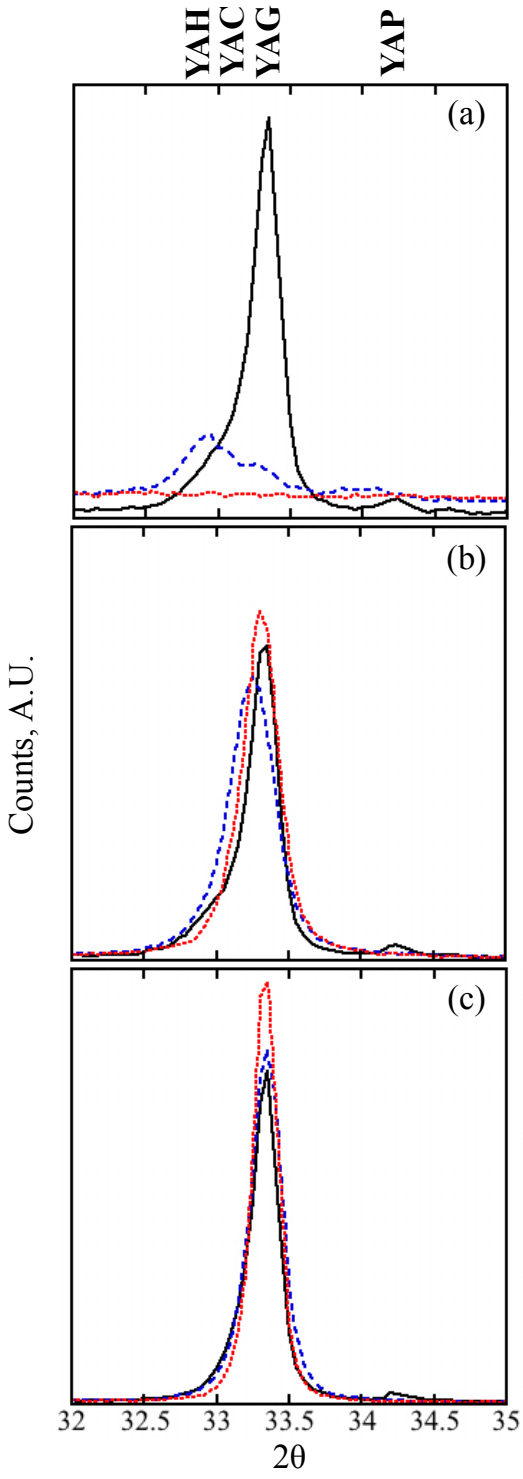

Figure 2.6. XRD spectra in the region of the YAG (420) peak acquired from YAG produced from fuel compositions 0 (-), 35 (– – –) and 100 (---) CA%. (a) as-synthesized, (b) 900°C, and (c) 1100°C post synthesis heat-treatments.

emission intensities, the data in Figures 3 through 6 should be correlated. If grain size controlled PL emission, powders with similar grain sizes should have similar PL emission. The minimal PL intensity emitted from as-synthesized powders produced using fuel composition of 50 or 100 CA% is consistent with these samples' lack of crystallinity. Powders produced using fuel compositions of 0, 50, and 100 CA% and heat-treated at 1100ºC have similar grain sizes, but differing PL emission intensity. Powders produced using fuel compositions of 25, 35, and 50 CA% have similar grain sizes, but differing PL emission intensities.

If the intensity of the PL emission is controlled by the crystal phases present in the powder all of the samples heat-treated at 1100ºC should have similar PL emission intensity as they contain mainly the YAG phase. If the presence of mixed crystalline phases controlled PL emission intensity, the sample produced from pure citric acid and heat treated at 1100ºC should have the highest PL intensity. However, the sample produced from pure citric acid and heat-treated to 1100ºC has a lower PL emission intensity than the as-synthesized and 900ºC heat-treated powders produced using pure urea, both of which contain mixed crystalline phases.

XPS

Since the XRD data do not explain the differences in trends in PL emission intensities of the as-synthesized and heat-treated materials, the elemental composition and bonding structure were investigated. As-synthesized and 1100°C heat-treated materials produced using pure citric acid (100 CA%) were analyzed by XPS**.** We focused on these materials because of the wide variation in crystallinity (amorphous to nearly pure YAG phase) and PL emission intensity (zero to second highest) between the as-

synthesized and 1100°C heat-treated materials. Survey spectra acquired from these materials contained only Al, Y, Ce, O, and C peaks. High-resolution spectra were acquired for the Al2p, O1s, Y3d and C1s transitions. The position of the carbon peak was used for energy scale correction due to charging.

Aluminum atoms in the YAG phase occupy both tetrahedral and octahedral lattice sites in a ratio of 3:2.[46] The binding energy of 2p electrons of aluminum atoms a in tetrahedral site is approximately 73.5 eV, while the 2p electrons of aluminum atoms in octahedral sites is approximately 73.9 eV.[46] Figure 2.7b presents the Al2p spectrum for the as-synthesized powder. The XRD pattern from this material, shown in Figure 2.7a, indicates this sample is amorphous. Curves representing tetrahedral and octahedral bonding do not fit the broad Al2p spectrum of the as-synthesized powder. This observation, along with the XRD pattern, suggests this sample does not contain the YAG phase.

The XPS spectrum of the Al2p transition for the 1100ºC heat-treated sample is presented in Figure 2.7f. Curves representing tetrahedral and octahedral bonding fit this spectrum well. The areas under the tetrahedral and octahedral bonding curves are in the proper ratio for the YAG phase. These observations are consistent with the XRD pattern acquired from this material shown in Figure 2.7e.

The oxygen atoms in the YAG phase are present in only one electronic environment, located in a tetrahedral lattice site surrounded by two yttrium and two aluminum atoms.[47] The O1s spectrum of the as-synthesized sample (Figure 2.7c) suggests the presence of a mixture of bonding types, including $Y(OH)_x$, $Al(OH)_x$, alumina and yttria bonding, along with some carbonaceous bonding.[48-51]

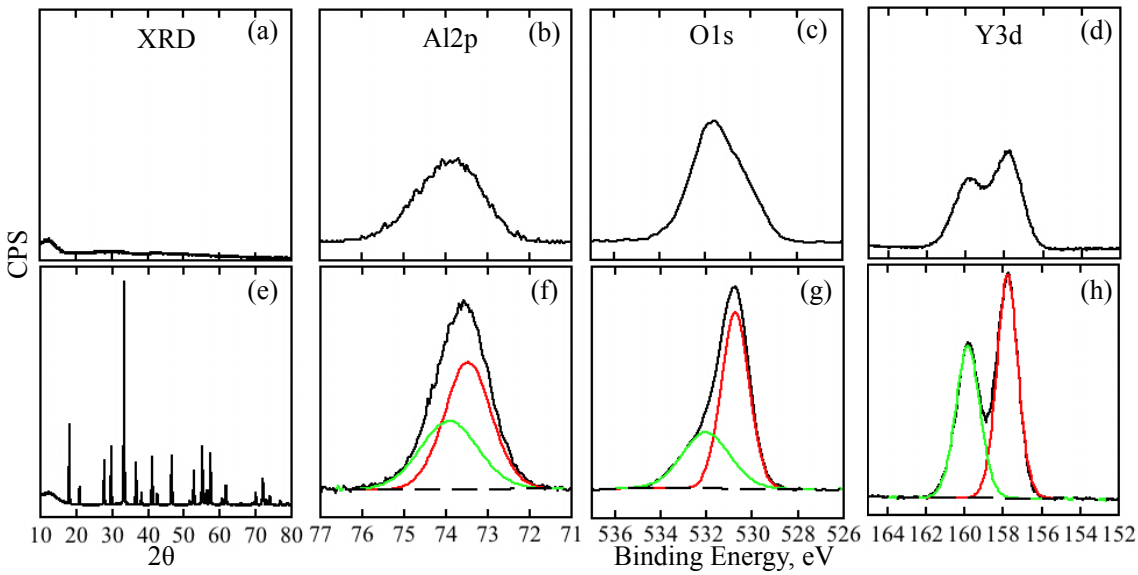

Figure 2.7. XRD patterns and high-resolution XPS spectra acquired from as-synthesized (top) and 1100°C post-synthesis heat-treated (bottom) material synthesized using pure citric acid (100 CA%). Plots of corresponding data from as-synthesized and heat-treated materials are plotted using the same y-axis scale.

The O1s spectrum of the heat-treated sample (Figure 2.7g) suggests the oxygen has two bonding states in this sample. Pawlak and coworkers contribute the presence of a second oxygen bonding configuration in YAG to the formation of a dipole around the oxygen atoms created by the iconicity difference between Al and Y atoms.[46] Cerium atoms would create another electronic environment for the oxygen in our cerium-doped YAG. However, the low concentration of cerium present (approximately 0.15 atomic%) in our materials would only account for a small fraction of the area under the curve for the observed second bonding state.

Yttrium atoms in the YAG phase are all located in a dodecahedral site.[46] The high-resolution Y3d spectrum acquired from the as-synthesized powder is presented in Figure 2.7d. The high-resolution Y3d spectrum acquired from the 1100ºC heat-treated powder is presented in Figure 2.7h. Curves representing the $3d^5/_2$ and $3d^3/_2$ spin orbital splitting describe the Y3d spectra from both the as-synthesized and heat-treated samples. The fitting was constrained by fixing the areas under the $3d^5/_2$ and $3d^3/_2$ curves at a ratio of 3:2. Note that while the area ratios of the $3d^5/_2$ and $3d^3/_2$ curves were fixed at the same ratio for fitting the as-synthesized and heat-treated materials, they are much more intense and narrow in the case of the heat-treated material compared to that of the as-synthesized material. Since the XRD analyses showed that the as-synthesized material was amorphous while the heat-treated material was crystalline in the YAG phase the XPS analyses show that the full width half maximum (FWHM) and intensity of the Y3d XPS peak change with crystallinity of these materials.

The FWHM of the $Y3d^5/_2$ transition can be used as a qualitative measure of the presence of mixed binding states of yttrium in the Y/Al/O system. Figure 2.8 plots the

FWHM of the $Y3d^5/_2$ transition as a function of heat treatment and fuel mixture composition. The as-synthesized materials have the broadest $Y3d^5/_2$ transitions, suggesting the presence of more than one yttrium binding state in these materials. The $Y3d^5/_2$ binding energies in the as-synthesized materials are different than of the $Y3d^5/_2$ binding energy in YAG. The binding energy of Y in materials synthesized from pure citric acid or from a fuel mixture with composition of 50 CA% suggests $Y(OH)_x$ type bonding. Yttrium in the material produced from pure urea has a lower binding energy than that in YAG. XRD showed that there was mainly YAG phase present in material produced from pure urea, but also indicated the presence of YAC and YAP phases. Due to the surface sensitivity of the analysis, the XPS data suggest that the YAC and/or YAP phases are present on the surface of the as-synthesized material produced from pure urea, and that yttrium in YAC and/or YAP has a lower binding energy than yttrium in YAG. The breadths of the $Y3d^5/_2$ transitions decrease with post-synthesis heat-treatment temperature, suggesting that higher temperatures reduce the number of yttrium binding states in heat-treated materials. The $Y3d^5/_2$ binding energy in all heat-treated materials approached 157.3 eV, which is consistent with the reported $Y3d^5/_2$ binding energy in YAG.[46,52] This agrees with the XRD data, which showed that the heat-treated materials primarily consisted of the YAG phase.

The XPS data do not explain the observed differences in PL emission intensity. A higher PL emission is expected from material with yttrium in only one bonding state, that of YAG. Materials made with pure citric acid (100 CA%) heat-treated at 1100ºC had the sharpest $Y3d^5/_2$ transition of all the materials in this study, yet its PL emission intensity was not the highest. The breadth of the $Y3d^5/_2$ transition in materials made from pure

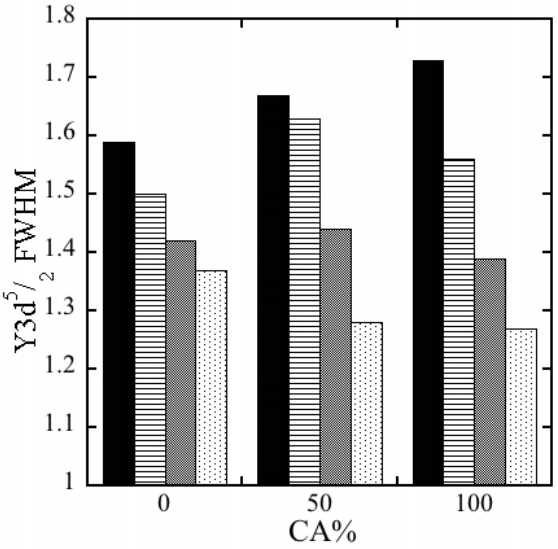

Figure 2.8. FWHM of the $Y3d^5/_2$ transition as functions of fuel composition and two hour post-synthesis heat-treatment temperature. (■) as-synthesized, (▤) 900°C, (▨) 1000ºC, and (▩) 1100ºC.

urea (0 CA%) decreased with 900ºC and 1000ºC heat-treatments, while the corresponding PL emission intensity decreased. The distribution of the dopant in the YAG crystal lattice could significantly affect the PL emission intensity of these materials. The XRD and XPS analyses do not address dopant distribution. The color of the synthesized materials can be qualitative indication of dopant incorporation into the crystal. The as-synthesized powders made from pure urea (0 CA%) were yellow. All other as-synthesized powders were black or brown. All heat-treated materials were yellow to varying degrees, with the materials produced from pure urea (0 CA%) and pure citric acid (100 CA%) being the most yellow. These color observations are consistent with the PL emission intensity trends. The materials with the more yellow color have higher PL emission intensities. Therefore, differences in fuel mixture composition and post-synthesis heat treatments may effect the distribution of the Ce dopant through the YAG phosphors produced, which in turn results in differing PL emission intensities of these phosphors.

Summary and Conclusions

Table 2.1 summarizes the results from PL, XRD, XPS analyses along with other experimental observations. Our data do not support the hypothesis that using a fuel mixture of urea and citric acid in combustion synthesis of YAG:Ce produces phosphors with increased emission intensity. Crystallinity, phases present, nor elemental bonding explain the observed trends in PL emission intensity with fuel composition. Interestingly, the highest PL emission intensity was produced from a material with mixed phases

(synthesized using pure urea) heat treated at 1100°C, not from the material with the most pure YAG phase(synthesized using pure citric acid). Qualitative observations of the color of the synthesized material seem to suggest that materials with the most intense yellow color have the most intense PL emission. Color can be correlated to dopant incorporation in the crystal, which suggests dopant incorporation may be affected by fuel composition and post-synthesis heat treatment. Follow–on work to investigate dopant distribution in the phosphors will be pursued.

Table 2.1. Summary of data from XRD, PL, XPS and experimental observations from studies of solution phase combustion synthesis of YAG:Ce. Grain sizes listed from top to bottom: as-synthesized, 900 °C, 1000 °C, and 1100 °C post-synthesis heat treatment. AS= as-synthesized, HT= heat-treated.

Fuel Composition (CA%)	Color AS/HT	Phases	Grain Size (nm)	Summary
0	Yellow/ Yellow	AS: YAG, YAP, YAC 1100 °C: YAG, YAP, YAC	47 47 50 54	PL: All cases highest emission intensity AS: overall smallest $Y3d^5/_2$ FWHM 1100 ºC: overall largest $Y3d^5/_2$ FWHM
25	Black/ Pale Yellow	AS: YAH, YAG 1100 ºC: YAG	17 29 33 39	PL: Emission intensity similar for all 25, 35, and 50 CA% materials
35	Black	AS: YAH, YAG 900 ºC: YAG	12 31 34 42	PL: Emission intensity similar for all 25, 35, and 50 CA% materials
50	Black/ Pale Yellow	AS: Amorphous 900 ºC: YAG	N/A 29 35 51	PL: Emission intensity similar for all 25, 35, and 50 CA% materials AS: $Y3d^5/_2$ suggests $Y(OH)_x$
100	Brown/ Pale Yellow	AS: Amorphous 900 ºC: YAG	N/A 34 39 53	AS: $Y3d^5/_2$ suggests $Y(OH)_x$ AS: overall largest $Y3d^5/_2$ FWHM 1100 ºC: overall smallest $Y3d^5/_2$ FWHM

References

[1] K. Du, J. Biesenbach, D. Ehrlichmann, U. Habich, U. Jarosch, J. Klein, P. Loosen, J. Niehoff, and R. Wester, Opt Quant Electron **27**, 1089 (1995).
[2] F. Li, J. West, A. Glushchenko, and C. Cheon, Journal of the Society of Information Display **6**, 523 (2006).
[3] D.-S. Xing, M.-L. Gong, X.-Q. Qiu, D.-J. Yang, and K.-W. Cheah, Mater Lett **60**, 3217 (2006).
[4] Y. Shimomura, T. Honma, M. Shigeiwa, T. Akai, K. Okamoto, and N. Kijima, J Electrochem Soc **154**, J35 (2007).
[5] P. Holister, J. Weener, and C. Vas, Technology White Papers Nr. 3 (2003).
[6] S.L. Weeden-Wright, (2012).
[7] M. Veith, S. Mathur, A. Kareiva, M. Jilavi, M. Zimmer, and V. Huch, J Mater Chem **9**, 3069 (1999).
[8] D. Jia, Y. Wang, X. Guo, K. Li, Y.K. Zou, and W. Jia, J Electrochem Soc **154**, J1 (2007).
[9] D. Klimm, S. Ganschow, and A. Pajączkowska, Journal of Alloys and … **436**, 204 (2007).
[10] L. Yang, T. Lu, H. Xu, W. Zhang, and B. Ma, J. Appl. Phys. **107**, (2010).
[11] Y. Wu, S. Parola, O. Marty, M. Villanueva-Ibanez, and J. Mugnier, in *Opt Mater* (2005), pp. 1471–1479.
[12] J. Nair, P. Nair, E. Doesburg, J.G. Van Ommen, and J. Ross, Journal of Materials … 4517 (1998).
[13] C.-C. Chiang, M.-S. Tsai, and M.-H. Hon, J Electrochem Soc **155**, B517 (2008).
[14] M. Nyman, L.E. Shea-Rohwer, J.E. Martin, and P. Provencio, Chem. Mater. **21**, 1536 (2009).
[15] Y. Kang, I. Lenggoro, S. Park, and K. Okuyama, Mater Res Bull **35**, 789 (2000).
[16] S. Aruna and A.S. Mukasyan, Current Opinion in Solid State and Materials … **12**, 44 (2008).
[17] L.E. Shea, J. McKittrick, O.A. Lopez, and E. Sluzky, J Am Ceram Soc **79**, 3257 (2005).
[18] N.A. Dhas and K.C. Patil, J Mater Chem **3**, 1289 (1993).
[19] S. Roy, L. Wang, and W. Sigmund, Mater Lett **39**, 138 (1999).
[20] N. Orlovskaya, Y. Chen, N. Miller, H. Abernathy, D. Haynes, D. Tucker, and R. Gemmen, Adv Appl Ceram **110**, 54 (2011).
[21] J. Li, Y. Pan, F. Qiu, Y. Wu, W. Liu, and J. Guo, Ceramics International **33**, 1047 (2007).
[22] R.K. Lenka, T. Mahata, P.K. Sinha, and A.K. Tyagi, J Alloy Compd **466**, 326 (2008).
[23] O. Ozuna, G. Hirata, and J. McKittrick, J Phys-Condens Mat **16**, 2585 (2004).
[24] E.J. Bosze, J. McKittrick, and G.A. Hirata, Materials Science and Engineering: B **97**, 265 (2003).
[25] Y. Tong, J. Zhu, L. Lu, X. Wang, and X. Yang, J Alloy Compd **465**, 280 (2008).
[26] J. McKittrick, L. Shea, and C. Bacalski, Displays **19**, 169 (1999).
[27] F. Deganello, G. Marci, and G. Deganello, Journal of the European Ceramic Society **29**, 439 (2009).
[28] L.E. Shea, J. McKittrick, O.A. Lopez, and E. Sluzky, J Am Ceram Soc **79**, 3257 (1996).

[29] M. Blosi, S. Albonetti, M. Dondi, A.L. Costa, M. Ardit, and G. Cruciani, J Sol-Gel Sci Techn **50**, 449 (2009).
[30] T. Xueyan, Z. Xiyan, L. Yinzhu, and Y. Peizhi, J Rare Earth **24**, 443 (2006).
[31] S. Aruna and K. Rajam, Mater Res Bull **39**, 157 (2004).
[32] C. Xu, S. Liu, C. Liu, W. Ding, S. Peng, and W. Chai, Micro Nano Lett **6**, 855 (2011).
[33] R. Ianoş, I. Lazău, C. Păcurariu, and P. Barvinschi, Eur J Inorg Chem **2008**, 931 (2008).
[34] P.S. Devi and S. Banerjee, Ionics **14**, 73 (2008).
[35] S. Sasikumar and R. Vijayaraghavan, Ceramics International **34**, 1373 (2008).
[36] K. Laishram, R. Mann, and N. Malhan, Ceramics International **37**, 3743 (2011).
[37] K.V.K. Gupta, A. Muley, P. Yadav, C.P. Joshi, and S.V. Moharil, Appl. Phys. B **105**, 479 (2011).
[38] J. Li, Y. Pan, F. Qiu, Y. Wu, and J. Guo, Ceramics International **34**, 141 (2008).
[39] G. Xia, S. Zhou, J. Zhang, and J. Xu, J Cryst Growth **279**, 357 (2005).
[40] J.F. Moulder, W.F. Stickle, P.E. Sobol, and K.D. Bomben, (1995).
[41] O. Yamaguchi, K. Matui, and K. Shimizu, Ceramics International **11**, 107 (1985).
[42] S.M. Sim, K.A. Keller, and T.I. Mah, J Mater Sci **35**, 713 (2000).
[43] E. Caponetti, M.L. Saladino, F. Serra, and S. Enzo, J Mater Sci **42**, 4418 (2007).
[44] Y. Waseda, E. Matsubara, and K. Shinoda, (2011).
[45] Y. Pan, M. Wu, and Q. Su, Materials Science and Engineering: B **106**, 251:256 (2004).
[46] D. Pawlak, K. Wozniak, Z. Frukacz, T. Barr, D. Fiorentino, and S. Seal, J. Phys. Chem. B **103**, 1454 (1999).
[47] D.A. Pawlak, K. Woźniak, and Z. Frukacz, Acta Crystallogr B Struct Sci **55**, 736 (1999).
[48] M. Giza, P. Thissen, and G. Grundmeier, Langmuir **24**, 8688 (2008).
[49] S.A. Barve, Jagannath, N. Mithal, M.N. Deo, A. Biswas, R. Mishra, R. Kishore, B.M. Bhanage, L.M. Gantayet, and D.S. Patil, Thin Solid Films **519**, 3011 (2011).
[50] X.-H. Guan, C. Shang, and G.-H. Chen, Journal of Environmental Sciences **19**, 312 (2007).
[51] J.A. Rotole and P.M.A. Sherwood, Surf. Sci. Spectra **5**, 32 (1998).
[52] E. Talik, M. Szubka, D. Skrzypek, W. Zarek, J. Kusz, and T. Łukasiewicz, Cryst. Res. Technol. **44**, 823 (2009).

CHAPTER III

EFFECT OF HEAT FLUX ON COMBUSTION SYNTHESIS OF YAG

Introduction

Solution combustion synthesis has been used to produce ceramic oxide powders since the early 1990's.[1-4] Of particular interest are phosphor oxide particles. Phosphor particles are materials that respond to being irradiated by light by emitting a photon.[5] The process of emitting a photon after irradiation with light is photoluminescence (PL). The emitted photon is typically lower in energy than the irradiation energy due to a process known as the Stokes shift.[5] This phenomena is used to produce light in a variety of applications such as televisions, LED's, and as laser sources.[6-10]

We have observed that the properties of YAG:Ce1% ($Y_{2.97}Ce_{0.03}Al_5O_{12}$) depend on the size of the crucible in which the combustion synthesis were performed. All other factors being the same, the YAG:Ce1% produced in 125 mL crucibles contained multiple crystal phases of the Y-Al-O system while only the YAG phase was present in YAG:Ce1% synthesized in the 225 mL crucibles. These results are shown in the x-ray diffraction patterns in Figure 3.1. The grain sizes of the materials produced in the two crucibles were similar, as were the intensities of their PL emission.

A lumped capacitance model was developed to investigate potential heating rate differences in the two crucibles. The crucibles are not only different volumes but also have different shapes. The 225 mL crucible is a cylinder, whereas the 125 mL is cylindrical at the top but narrows to a smaller base than its top. The thermal time

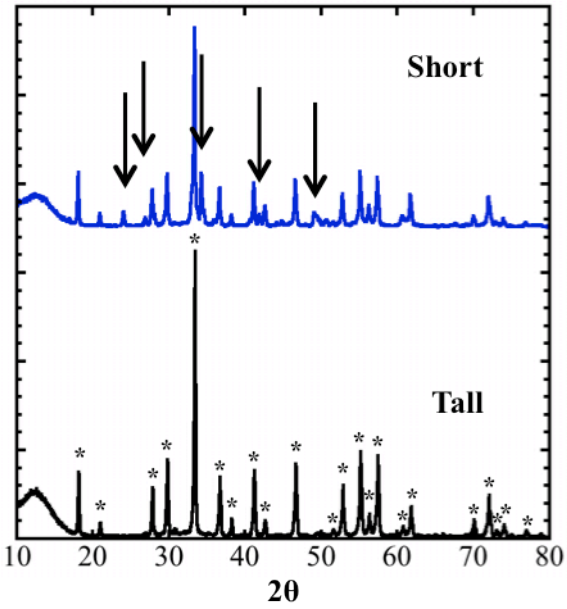

Figure 3.1. X-ray diffraction pattern of YAG material made in a 225 mL (bottom) and 125 mL (top) crucible. Lines indicate major imperfections in 125 mL crucible material not present in 225 mL crucible material. * indicate YAG reference JCPDS 33-0040, arrows indicate peaks not YAG from reference.

constant, τ, was derived from a transient heat transfer model for the system shown in Figure 3.2a. In the model the temperature at the interface of the hot plate and crucible was assumed to be 873°K and the resistance between the hot plate and crucible was assumed to be negligible. Equation 3.1 is the resulting transient thermal model and Equation 3.2 is the solution as a function of time. The variables and values used for the calculations are shown in Table 3.1.

$$q_3 - q_1 - q_2 \equiv (T_H - T)\frac{k_3 A_3}{L_3} - (T - T_\infty)\frac{1}{R_{tot}} = \rho V c \frac{dT}{dt} \quad , \; R_{tot} = \frac{k_2 + L_2 h_2}{hA(k_2 + L_2 h_2) + k_2 A_2 h_2} \tag{3.1}$$

$$T(t) = s + (T_\infty - s)e^{-Bt}, \text{ where } s = \frac{k_3 A_3 T_H R_{tot} + T_\infty L_3}{k_3 A_3 R_{tot} + L_3} \text{ and } \frac{1}{\tau} = B = \frac{1}{\rho V c\left[\frac{k_3 A_3 R_{tot} + L_3}{R_{tot} L_3}\right]} \tag{3.2}$$

Solving these equations allows for a simulation of the temperature profile for each crucible. For simulation the density (ρ), volume (V) and specific heat (c) of the control volume had to be defined. All three values could be a function of temperature and in a combustion synthesis would be expected to change due to chemical composition changes and phase transformations. For the sake of simulation, the control volume was assumed to have the properties of water at 298°K and that they were constant throughout the simulation. Figure 3.2b shows the calculated temperature of the control volme in each crucible as a function of time. The 225 mL crucible heats faster than the 125 mL crucible. Note that the temperature approaching 873°K is not true since a water control volume would not reach the ultimate temperature as modeled; however, the difference in temperature of the two crucibles is of interest to this analysis. The model shows the

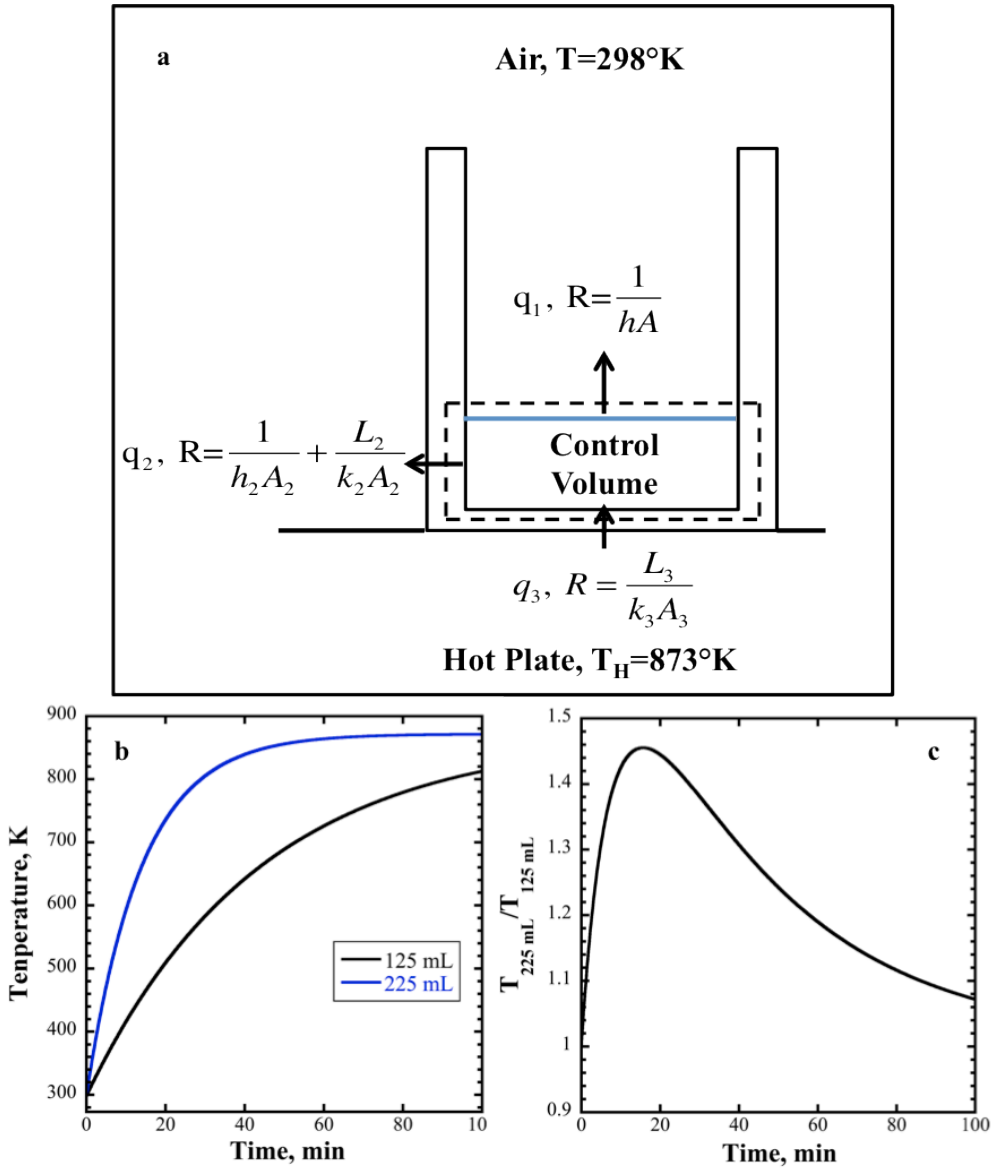

Figure 3.2. (a) Energy balance model used in the lumped capacitance model, (b) evaluation of model for 225 and 125 mL crucibles and (c) the ratio of the temperatures for the 225 and 125 mL crucibles. The model assumes the heat is coming from a hot plate and leaving from all other surfaces.

225 mL crucible heat faster than the 125 mL. The ratio of the temperature for the 225 and 125 mL crucibles is plotted in Figure 3.3c. The ratio shows that at its maximum the 225 mL crucible is ~1.45 times hotter than the 125 mL crucible. This model suggests that the reactant will experience different heating rates depending on crucible size chosen and could be responsible for the differences seen in Figure 3.1.

Previous researchers have investigated heating effects on combustion synthesis have been investigated by evaluating material combusted at various furnace temperatures. Shea and coworkers investigated YAG:Cr and found a furnace temperature of 500°C produced material with the maximum brightness[11]. The group claimed that by increasing furnace temperature there will be residual water would be present at ignition which would lower the flame temperature and hinders the formation of YAG.[11] Yao and coworkers investigated combustion synthesis of $(Zn_x,Sr_{1-x})_y(Al_a, B_{1-a})_2O_4:Eu_{1-y}$ at furnace temperatures from 400-900°C.[12] Yao showed that PL intensity increased with furnace temperature up to 600°C and then decreased with further increase in furnace temperature.[12] They did not suggest a mechanism to explain their observations. Song and coworkers used x-ray diffraction to compare the $SrAl_2O_4$ made at combustion furnace temperatures of 400-900°C.[13] Song found furnace temperatures up until 600°C produced increasingly more intense peaks of the monoclinic phase, a mixture of monoclinic and hexagonal phases at 700°C, and pure hexagonal phase at temperatures above 700°C.[13] These investigations suggest that heating flux can influence both the performance (PL) and the phases present in the synthesized material, but the mechanisms of why the furnace temperature affects the end product is not fully understood.

This work investigated heat flux effects on the material produced by combustion synthesis. A lumped capacitance model suggested a hypothesis that heating rate would be different between the 225 mL and 125 mL crucibles and indicated a need for further investigation. Thermogravimetric analysis (TGA) with differential scanning calorimetry (DSC) experiments were used to further investigate the effects of heating rate. The TGA/DSC experiments identified an optimal heating rate that maximized the heat of reaction. Transmission electron microscopy (TEM) imaging of the materials made in the TGA/DSC experiments supported the findings from the DSC data, showing heating rates produce material with different crystallinity and different grain sizes.

Experimental Details

Material Synthesis and TGA/DSC

The synthesis procedures for the batches in the large crucibles were the same as in our previous work. In short, the reactants are dissolved in water then dehydrated to a viscous solution on an 80ºC hot plate. The viscous solution is then placed in a furnace at 600ºC to initiate combustion as per reactions 1-3. For TGA/DSC experiments the viscous solution cooled to room temperature (~25ºC) before adding to the instrument. The reactant metal nitrates and fuel [$Y(NO_3)_3 \bullet 6H_2O$ (Sigma Aldrich, 99.9%), $Al(NO_3)_3 \bullet 9H_2O$ (Sigma Aldrich, 99+%), $La(NO_3)_3 \bullet 6H_2O$ (Sigma Aldrich, 99.999%), $ZrO(NO_3)_2 \bullet 2H_2O$ (Noah Labs, 99.99%), urea (CH_4N_2O, Sigma Aldrich 99.0-100.5%), and glycine ($C_2H_5O_2N$, Sigma Aldrich, ≥99.0%)] were added in stoichiometric ratios to make 0.001 mol of the desired material. Five milliliters of deionized water (≥12.5

MΩcm) were added to enhance mixing of the reactants. The solution was then heated on an 80ºC hot plate, continuously stirring with a PTFE coated stir bar until a viscous solution was obtained. Solutions were constantly mixed during the entire experiment.

$$3Y(NO_3)_3 + 5Al(NO_3)_3 + 20CH_4N_2O \rightarrow Y_3Al_5O_{12} + 20CO_2 + 40H_2O + 32N_2 \quad \textbf{RXN1}$$

$$3Y(NO_3)_3 + 5Al(NO_3)_3 + 13.3C_2H_5O_2N \rightarrow Y_3Al_5O_{12} + 26.7CO_2 + 33.3H_2O + 18.7N_2 \quad \textbf{RXN2}$$

$$2La(NO_3)_3 + 2ZrO(NO_3)_2 + 5.6C_2H_5O_2N \rightarrow La_2Zr_2O_7 + 11.1CO_2 + 13.9H_2O + 7.8N_2 \quad \textbf{RXN3}$$

Thermogravimetric analysis (TGA) and differential scanning calorimetry (DSC) were conducted in a TA Instruments Q600. Argon purge gas was flowed in the system at 10mL/min. The instrument was calibrated with sapphire for heat flow and with reference weights over our temperature range for each heat rate chosen. Exothermic events are defined to be in the positive heat flow direction for all DSC data presented. Initial reactant masses of approximately 25 mg were used in each run for thermal analysis. The amount provided enough material to produce thermal events but not enough to blow the sample cup off the balance arm**.**

X-ray Diffraction

Powder x-ray diffraction (XRD) was conducted using a Scintag X_1 *θ/θ* automated x-ray diffractometer with a Cu target, a Peltier cooled solid-state detector, and a plastic sample support. The XRD patterns were compared to the JCPDS files 33-0040 for YAG, 33-0041 for yttrium aluminum perovskite (YAP, $YAlO_3$), 34-0368 for yttrium aluminum monoclinic (YAM, $Y_4Al_2O_9$), and 38-0222 for the $YAlO_3$ material with a cubic garnet

structure (YAC). The work of Sim and Caponetti was used to identify the yttrium aluminum hexagonal (YAH, $YAlO_3$) phase[14,15].

Transmission Electron Microscopy

High resolution transmission electron microscopy (TEM) images were obtained using a Tecnai Osiris operating at 200 kV. Samples were prepared by drop-casting nanoparticle suspensions onto ultrathin carbon-coated TEM grids. Data were collected and analyzed was performed using the TEM Imaging & Analysis software (FEI).

Results

TGA

TGA measures how the mass of a system changes as a function of temperature or time. An example of a TGA profile and its corresponding time derivative profiles are shown in Figure 3.3a for YAG synthesis using urea as the fuel. Ideally, the solution would lose mass first due to water evaporation followed by a loss due to the combustion reaction, after which the mass would remain constant. The mass profile in Figure 3.3a is consistent with what would be expected through the water loss phase, but includes losses in addition to that due to the expected combustion reaction.

The gradual decline in mass from the starting temperature to the first differential peak is the temperature range in which the ignition is expected to occur. The slow decline in mass around 100°C is due to the loss of water. The decline in mass continues until there is a fast mass loss event due to combustion. The mass lost prior to combustion but

after water evaporation was due to an alternative, non-combustion processes. There is another sharp mass loss event around 240°C, indicating another potential reaction occurring that drove off a significant amount of mass quickly. Our analysis concentrates on the first mass loss event.

The reactants in the combustion synthesis of YAG using urea as the fuel have different thermal decomposition behaviors. The two reactants with the lowest thermal decomposition temperature are urea and $Al(NO_3)_3$. Urea has been found to begin decomposition in a range from 103 to 155°C, decomposing into a mixture of cyanic acid, biuret, and cyanuric acid before completely converting to biuret acid at 230°C.[16-20] The decomposition range suggests the testing environment can have a significant impact on the degradation behavior. The amount of oxygen appears to impact the initial degradation, the low end of the range was found in a closed system and the high end of the range in an open vessel. The open vessel number is more akin to our system, but the presence of the nitrate molecules and adsorbed waters of hydration could have affects on the degradation temperature not demonstrated in literature. The $Al(NO_3)_3$ molecule breaks down by first shedding the waters of hydration, then forms aluminum hydroxide until finally producing alumina at approximately 400°C.[21,22] The nitrate decomposition to hydroxide is nearly complete by 170°C.[21] Nitrates act as the oxidizer for the urea, so as $Al(NO_3)_3$ that converts to alumina the fewer nitrate molecules will be available for combustion, resulting in a fuel-rich combustion. Oxidizer loss due to degradation should increase with increasing combustion (or ignition) temperatures, which could further compromise the properties of the synthesized material.

We identify the ignition point of our combustions at the temperature where there

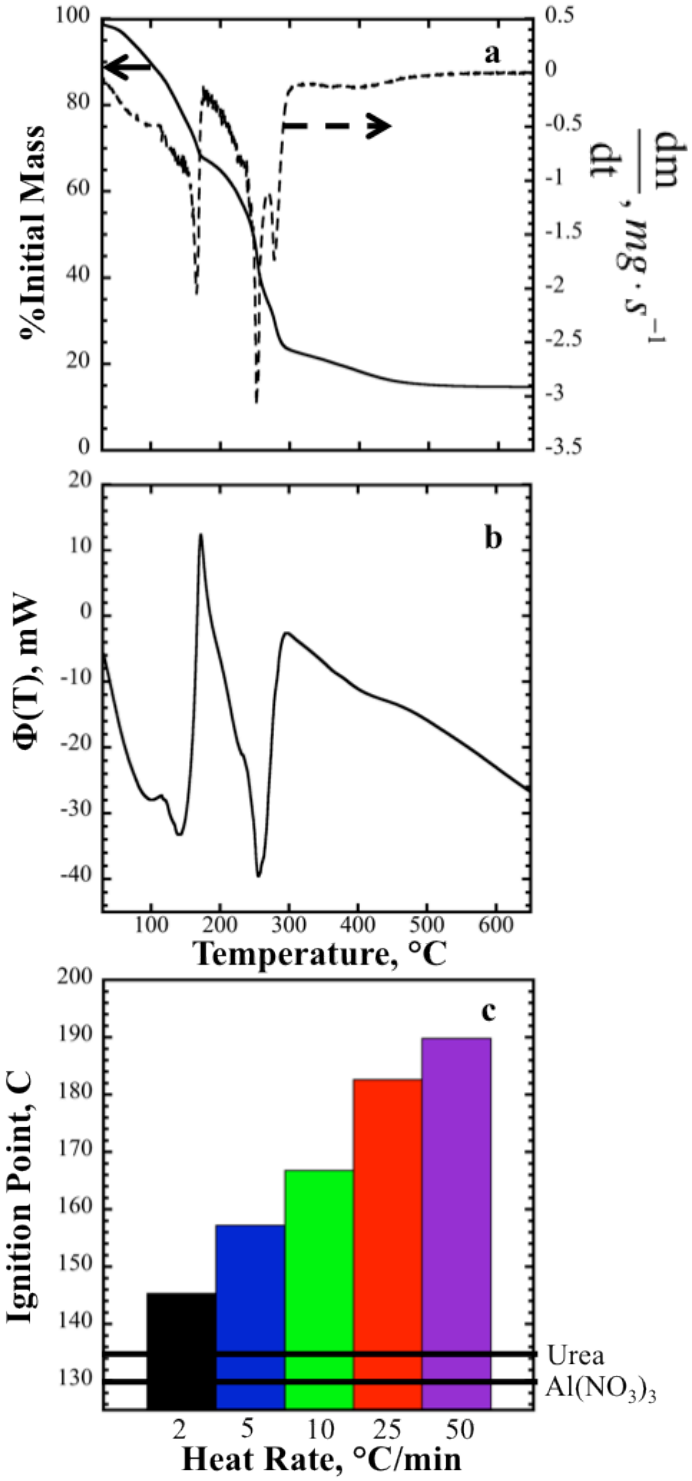

Figure 3.3. (a) TGA at a heating rate of 10°C/min, (b) DSC curve at a heating rate of 10°/min and (c) experimentally determined ignition point as a function of temperature ramp rate for YAG combusted from urea as the fuel.

is a minimum in the time derivative of the mass data and a corresponding maximum in the heat flow data. In Figure 3.3a the ignition point is approximately 145°C. There are two minima in the urea reaction TGA profile but only the first can be associated with a maximum in the heat flow data.

The externally determined ignition points and degradation temperatures of the molecules of interest are shown in Figure 3.3c. The ignition point increases with temperature ramp rate and is always higher than the degradation temperatures of urea and aluminum nitrate. The shift in the ignition temperature is likely due to the competing decomposition and reaction processes taking place in the solution.

DSC

DSC measures the heat flow (Φ) required by a sample system to maintain a specific heating schedule. Figure 3.3b is the DSC profile for YAG synthesis using urea as the fuel at a heating rate of 10°C/min. The heat released by the reaction (ΔH_{rxn}) was calculated from the DSC data. The integral of the heat flow (Φ) as a function of time, as shown in Equation 3.3, was used to calculate the experimental ΔH_{rxn}. Figure 3.4a is a typical exothermic peak for YAG combusted with urea at 10°C/min integrated using this method including the background.

$$\Delta H_{rxn} = \int_{t_1}^{t_2} \Phi(t)\, dt \qquad \textbf{Eq. 3.3}$$

The ΔH_{rxn} was normalized against the theoretical enthalpy of reaction (ΔH_t). Hess's law was used to calculate the energy needed to make one mole of product, ΔH_t.

The values in Table 3.3 along with Hess's law and the balanced reactions above, ΔH_t, the theoretical heat of reaction, for RXN 1-3 have been calculated and are shown in Table 3.4. The mass at the end of the sharp mass loss event was assumed to be YAG and was used to calculate the moles of material produced to scale ΔH_t to the actual moles of product formed. The percent of theoretical heat was calculated and is shown in Figure 3.4b for heating rates between 2 and 50°C/min. The 10°C/min ramp rate produced the closest energy release compared to theoretical.

The experimental values of ΔH_{rxn} are expected to be below ΔH_t for three reasons. First, the actual combustion was not adiabatic. Second, there are inaccuracies in the measurement technique at high temperature ramp rates. Thermal lag causing multiple thermal events to overlap due to the speed of the temperature rise is the primary issue with high temperature ramp rates. Third, and most important to processing considerations, would be due to a non-stoichiometric combustion. The reaction can be non-stoichiometric due to reactant degradation before ignition or different product phases produced than those used in theoretical calculations. Intuition from the TGA data suggests thermal degradation of reactants is the primary mechanism producing non-stoichiometric reaction conditions at low ramp rates. At high ramp rates there could also be non-stiochiometric ratios occurring at ignition but the mechanisms should be different at high ramp rates than the low ramp rates since the issue of precursor degradation should become less a factor as temperature ramp rate increases.

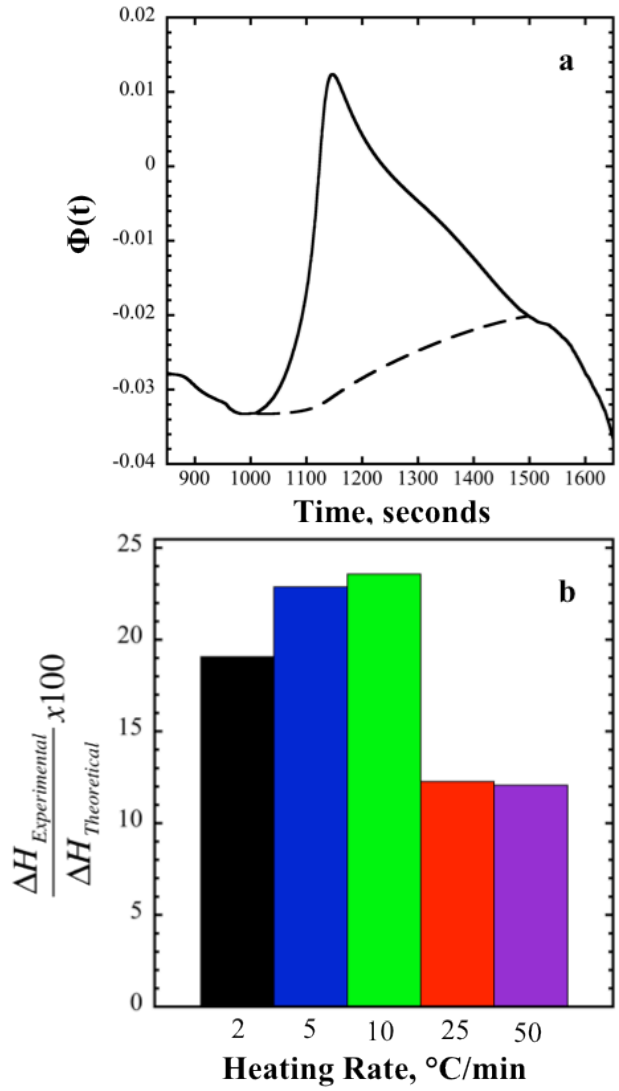

Figure 3.4 (a) Heat flow as a function of time with the background used to calculate ΔH_{rxn}. (b) Percent of theoretical heat released by the reaction as a function of heating rate.

TEM

TEM images were acquired of the material generated in the TGA/DSC runs at ramp rates of 5, 10, 25 and 100°C/min. Micrographs of the materials produced using the various heating rates are shown at two magnifications in Figures 3.5a-d. The images indicate that the heat flux from the TGA experiments influence the amount of crystalline material present in the final product. At 5°C/min the material is amorphous with no crystalline grains. At 10°C/min, the material is crystalline with relatively large grains. A heat rate of 25°C/min produces polycrystalline material with small grains. Lastly, the 100°C/min sample showed only a few small grains

Grain sizes cannot be determined from this analysis. The materials began to crystallize during analysis and grains generated by synthesis versus the electron beam could not be differentiated. Qualitatively, these crystalline trends agree with the TGA/DSC data.

Discussion

Suggested Mechanisms

The TGA/DSC data suggests that at low temperature ramp rates reactant degradation lowers the heat of reaction by igniting a fuel-rich mixture. If the reactant solution heats uniformly and only reactant degradation was responsible for differences in the heat of reaction, the ΔH_{rxn} should increase with increasing temperature ramp rates due to decreased reactant degradation. The decrease ΔH_{rxn} with increasing heat rates suggests that an additional mechanism becomes significant at temperature ramp rates above

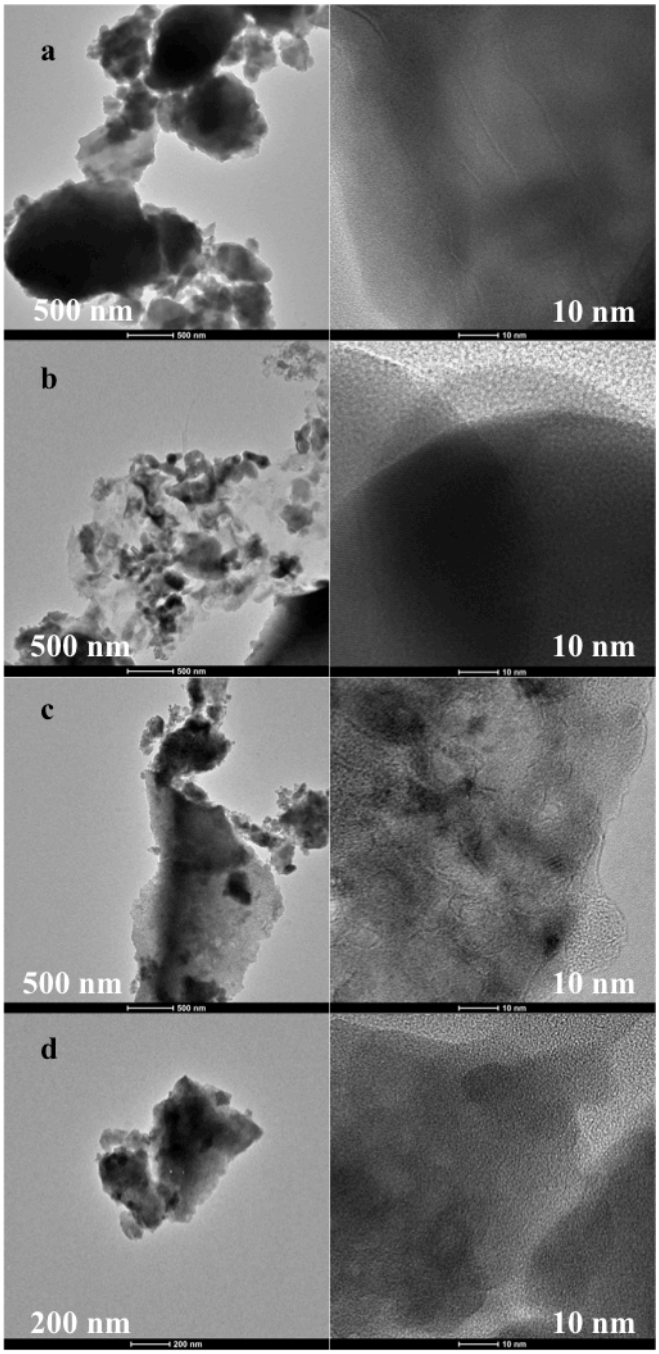

Figure 3.5. HRTEM images of material created by running the YAG/urea reaction at (a) 5, (b) 10, (c) 25 and (d) 100°C/min. Low magnification is on the left, high magnification on the right as indicated by the scale bars.

10°C/min.

At high ramp rates thermal gradients could form in the reactant volume. Thermal gradients could cause issues by causing non-uniform ignition and drive concentration gradients across the bulk. A uniform ignition would release the energy from the whole reactant volume at once, producing a maximum amount of energy experienced by the whole reactant system. Reactions igniting non-uniformly, ie only small portions of the reactant combust at a time, could produce localized heating and some of that heat will be used to heat nearby reactant, reducing the amount of energy to increase the temperature needed for crystal formation. Compounding on the ignition issues, localized heating could change the solubility characteristics of the solution. Reactants leaving solution would contribute to non-stoichiometric ratios of oxidizers and fuels at the localized ignition points, lowering ΔH_{rxn}.

These mechanisms are dependent on the system studied and will change with the ignition temperature of the reactants involved. For instance, in systems where the reactants do not degrade below the ignition temperature should not exhibit the low temperature ramp rate dependence exhibited by the YAG system combusted using urea. The low temperature ramp rate resistant system could still be affected at high ramp rates if the thermal gradient mechanism is correct.

Application to Analogous System: LZO/Glyicne

The LZO combustion synthesis using glycine as the fuel has been shown to be a vibrant reaction that produces crystalline material in the desired pyrochlore crystal structure directly from synthesis on the large scale.[2,23] We performed similar TGA/DSC

experiments to those described above to find the heat of reaction for LZO synthesis. Figure 3.6 shows a TGA curve, DSC curve and normalized ΔH_{rxn} at various ramp rates. The trend seen in Figure 3.6 is similar to that of YAG synthesis using urea.

The LZO system is similar to the YAG/urea system because it has an ignition temperature (~230°C) above a reactant degradation temperature. $ZrO(NO_3)_2$ has been shown to begin degrading toward ZrO_2 around 185°C.[24] In the TGA curve in Figure 3.6a the second mass loss starting at ~150°C corresponds to attached water detachment and then at ~175°C for nitrate degradation towards ZrO_2. The second mass loss is slight and begins leveling off before ignition indicating the degradation effect is ending before the ignition. The maximum heat of reaction for the LZO chemistry occurs with a temperature ramp rate of 10°C/min. The analogous study of the crystal structure with TEM was not performed. If the TEM study was conducted we expect results similar to the YAG system based on the both chemistries producing highly crystalline material on the large scale.

The LZO/glycine reaction has a much steeper mass loss on ignition than the YAG/urea reaction and a more well-defined exothermic event upon ignition. The YAG/urea reaction had many competing processes occurring simultaneously, blurring the independent thermal events into a broad peak. Lacking defined thermal events made choosing endpoints for the integrals difficult for the YAG experiments. For LZO, the endpoints were more well-defined, suggesting the endpoints may be more accurate for the LZO system. The similar shapes of the well-defined LZO system and less well-defined YAG system supports the conclusions drawn from the YAG data, even though it is less defined.

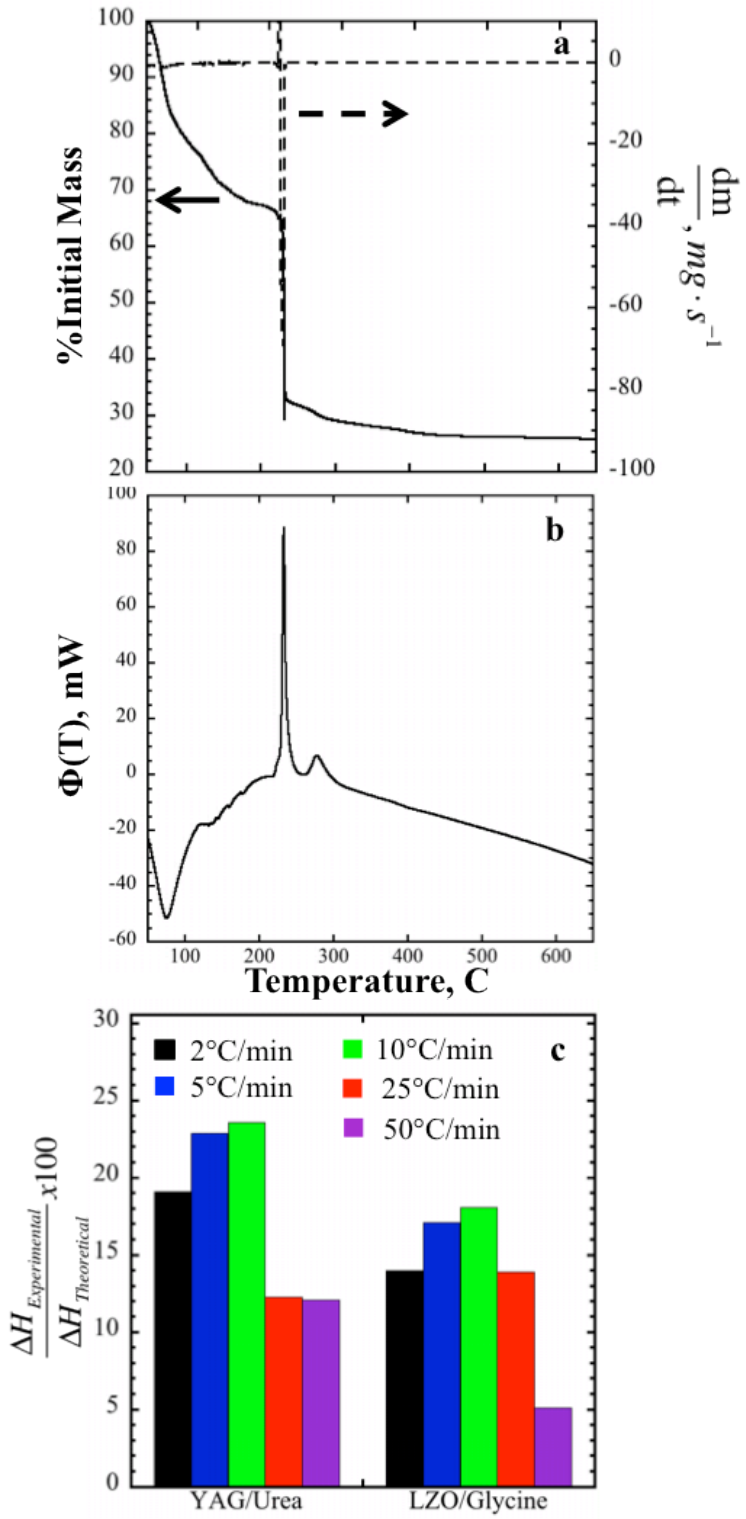

Figure 3.6. (a) TGA and (b) DSC curves for the LZO/glycine system at 10°C/min and (c) energy released by the reaction compared to theoretical.

Application to Incongruous System: YAG/glycine

YAG combustion from glycine fuel does not produce a vibrant flame; the reaction produces a slow moving ignition front without a significant flame when combusted on the large scale. The product of a glycine reaction is an ashy black solid. The black residue is carbon which can be removed with calcining. Diffraction patterns of the as-synthesized YAG/glycine system show no crystalline features and produce no features until the material has been annealed at temperatures of 850°C or above.[11,25]

Corresponding TGA/DSC studies were conducted for YAG combusted using glycine fuel and the results are summarized in Figure 3.7. Figure 3.7 shows the TGA and DSC curves are similar to those produced by the LZO/glycine reaction. However Figure 3.7c shows the energy generated by the reaction does not have a maximum at 10°C/min as in the previous two examples. Instead, the energy released decreases with increasing heating rate. The ignition temperature for these reactions were ~230°C, the same as the LZO/glycine reactions. The mechanisms for the urea reaction indicate significant reactant degradation before ignition, but two reactants were simultaneously degrading. Unlike the urea reaction, the glycine reaction only faces potential $Al(NO_3)_3$ degradation since here the ignition point is roughly the glycine degradation temperature. The increasing reaction energy with decreasing ramp rate suggests that the reactant mixture may have another aspect to it not apparent in the data collected.

Authors have suggested that fuels could have a coordinating affect on reactants in the gel phase.[25-29] The coordination effect was apparent when attempting to produce LZO from glycine or urea. When mixed, the glycine reactant was a clear, homogeneous solution. The urea reactant mixture was a granular white paste that did not combust to

produce LZO. Combustions for LZO used $ZrO(NO_3)_2$ as the Zr source. The $ZrO(NO_3)_2$ has a low solubility in water, explaining the white paste was produced when mixed with urea; the oxynitrate did not dissolve[30,31]. When mixed with glycine the clear appearance and homogeneous nature demonstrates the coordinating impact of fuel on the other reactants by solubilizing the oxynitrate.

For YAG both the urea and glycine mixtures form homogeneous solutions so there is not a visible difference between the two fuels as with LZO. The lack of optical differences does not indicate a lack of coordination. Glycine could be coordinating the reactants in such a way that the degradation of $Al(NO_3)_3$ is slowed and a reaction can take place at a temperature well above the thermal degradation temperature. Why the coordination effect decreases with increasing ramp rates is not apparent from the data presented.

Authors have suggested that fuels could have a coordinating affect on reactants in the gel phase.[25-29] The coordination effect was apparent when attempting to produce LZO from glycine or urea. When mixed, the glycine reactant was a clear, homogeneous solution. The urea reactant mixture was a granular white paste that did not combust to produce LZO. Combustions for LZO used $ZrO(NO_3)_2$ as the Zr source. The $ZrO(NO_3)_2$ has a low solubility in water, explaining the white paste produced when mixed with urea. When mixed with glycine the clear appearance and homogeneous nature demonstrates how important the coordinating effect of a fuel can be.

For YAG both the urea and glycine mixtures form homogeneous solutions so there is not a visible difference between the two fuels as with LZO. The lack of optical differences does not indicate a lack of coordination. Glycine could be coordinating the

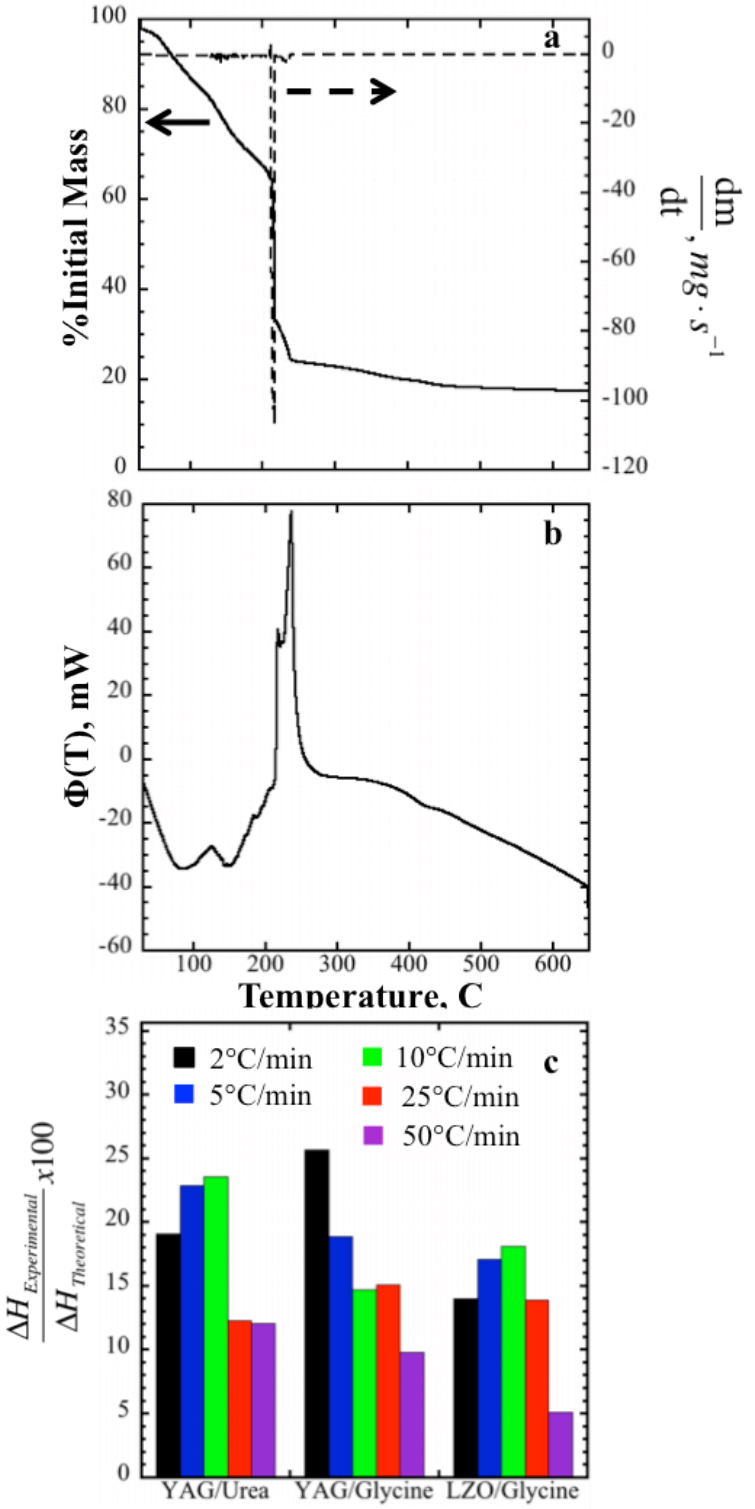

Figure 3.7. (a) TGA and (b) DSC curves for the YAG/glycine system at 10°C/min and (c) energy released by the reaction compared to theoretical.

reactants in such a way that the degradation of $Al(NO_3)_3$ is slowed and a reaction can take place at a temperature well above the thermal degradation temperature. Why the coordination effect decreases with increasing ramp rates is not apparent from the data presented.

Conclusions

Synthesizing YAG:Ce1% in two different sized crucibles produced different crystal phases. We have investigated why the reaction vessel affected the final material using a lumped capacitance model, TGA/DSC and TEM techniques. The analyses suggest that heat rate will change the crystalline material present after a combustion synthesis reaction.

The techniques to understand the YAG/urea system were employed to investigate the LZO/glycine and YAG/glycine systems. LZO/glycine reactions showed a similar optimum heat rate while the YAG/glycine system produced more energy at low heating rates. These data suggest that for new materials systems and fuels the optimum heating rate will likely be different. When developing combustion synthesis processes for new material, similar experimental parameters should be varied to identify optimum heating requirements for the material system and fuel desired to produce high quality crystals.

Tables

Table 3.1. Variable table, with references for actual values used in estimating thermal time constant and the results.

Variable	Description	Value
A	Surface area, top of lump (exposed to air), m^2	See Table 4
A_2	Surface area, sides of lump, m^2	
A_3	Surface area, between lump and hot plate, m^2	
L_2, L_3	Characteristic length; cup thickness	0.003 m
h	Natural convection heat transfer coefficient of air at 298°K, $W/m^2/K$	25[32]
k_2, k_3	Alumina thermal conductivity at 298°K, W/m/K	32.7[32]
τ	Thermal time constant	
t	Time	
T	Temperature of the lump	
T_{600}	Temperature of furnace/bottom of cup	873°K
T_∞	Temperature of surrounding air,	298°K
V	Specific volume, m^3	$5x10^{-6}$
c	Specific heat of lump, J/kg/K	4181[33]
ρ	Density of lump, kg/m^3	1000

Table 3.2. Equations for the various surface areas used in the cup modeling with values used for calculation.

Parameter	Expression	Value
Volume		5 mL
	125 mL Crucible	
A	πr_2^2	989.8 mm^2
A_2	$\pi(r_1+r_2)\sqrt{h_{125}^2+(r_2-r_1)^2}$	654.4 mm^2
A_3	πr_1^2	730.6 mm^2
h_{125}	$\frac{3V}{\pi(r_1^2+r_1r_2+r_2^2)}$	5.8 mm
r_1		15.25 mm
r_2	$r_1+h\tan(23.2)$	17.75 mm
	225 mL Crucible	
A	πr^2	2290.2 mm^2
A_2	$2\pi rh_o$	369.8 mm^2
A_3	A	2290.2 mm^2
r		27 mm
h_o		2.2 mm

Table 3.3. ΔH_f for various reagents in the combustion synthesis reaction.

Chemical	Enthalpy of Formation (kJ/mol)
$Y(NO_3)_3$	-1424[11]
$Al(NO_3)_3$	-1160[11]
$La(NO_3)_3$	-1254.4[34]
$ZrO(NO_3)_2$	-1948.6[2]*
$C_2H_5O_2N$	-527.8[35]
CH_4N_2O	-333[35]
N_2	0
CO_2	393.5[35]
$H_2O_{(v)}$	-241.8[35]
LZO	-4102[36]
YIG (Substitute for YAG)	-4810[11]

*This value was derived by the authors based on the proposed reaction of $ZrO(NO_3)_2$ with urea to make ZrO_2 as given by Dhas.[2]

Table 3.4. ΔH_{rxn} for the two material systems with various fuels. Calculated with ideal stoichiometry; i.e. to make 1 mole of product material.

Product/Fuel	Enthalpy of Reaction (kJ)
YAG/urea	-5620.0
YAG/glycine	-6256.3
LZO/glycine	-2491.8

References

[1] K. Suresh and K.C. Patil, Journal of Materials Science Letters **12**, 572 (1993).
[2] N.A. Dhas and K.C. Patil, J Mater Chem **3**, 1289 (1993).
[3] J.J. Kingsley, N. Manickam, and K.C. Patil, B Mater Sci **13**, 179 (1990).
[4] P.S. Devi and H.S. Maiti, J Solid State Chem **109**, 35 (1994).
[5] D. Vij, *Luminescence of Solids* (Plenum Pub Corp, 1998).
[6] K. Du, J. Biesenbach, D. Ehrlichmann, U. Habich, U. Jarosch, J. Klein, P. Loosen, J. Niehoff, and R. Wester, Opt Quant Electron **27**, 1089 (1995).
[7] F. Li, J. West, A. Glushchenko, and C. Cheon, Journal of the Society of Information Display **6**, 523 (2006).
[8] D.-S. Xing, M.-L. Gong, X.-Q. Qiu, D.-J. Yang, and K.-W. Cheah, Mater Lett **60**, 3217 (2006).
[9] Y. Shimomura, T. Honma, M. Shigeiwa, T. Akai, K. Okamoto, and N. Kijima, J Electrochem Soc **154**, J35 (2007).
[10] P. Holister, J. Weener, and C. Vas, Technology White Papers Nr. 3 (2003).
[11] L.E. Shea, J. McKittrick, O.A. Lopez, and E. Sluzky, J Am Ceram Soc **79**, 3257 (1996).
[12] S.-S. Yao, Y.-Y. Li, D.-H. Chen, W.-J. Tang, and Y.-H. Peng, Cent Eur J Phys **7**, 96 (2009).
[13] H. Song and D. Chen, Luminescence **22**, 554 (2007).
[14] S.M. Sim, K.A. Keller, and T.I. Mah, J Mater Sci **35**, 713 (2000).
[15] E. Caponetti, M.L. Saladino, F. Serra, and S. Enzo, J Mater Sci **42**, 4418 (2007).
[16] J.P. CHEN and K. ISA, J. Mass Spectrom. Soc. Jpn. **46**, 299 (1998).
[17] L. Stradella and M. Argentero, Thermochim Acta **219**, 315 (1993).
[18] S. Biamino and C. Badini, Journal of the European Ceramic Society **24**, 3021 (2004).
[19] P.M. Schaber, J. Colson, S. Higgins, D. Thielen, B. Anspach, and J. Brauer, Thermochim Acta **424**, 131 (2004).
[20] C.-C. Hwang, T.-Y. Wu, J. Wan, and J.-S. Tsai, Materials Science and Engineering: B **111**, 49 (2004).
[21] B. Pacewska and M. Keshr, Thermochim Acta **385**, 73 (2002).
[22] J. Mu, Thermochim Acta (1982).
[23] N. Orlovskaya, Y. Chen, N. Miller, H. Abernathy, D. Haynes, D. Tucker, and R. Gemmen, Adv Appl Ceram **110**, 54 (2011).
[24] W. Wendlandt, Anal. Chem. **32**, 848 (1960).
[25] M.B. Kakade, S. Ramanathan, and S.K. Roy, Journal of Materials Science Letters **21**, 927 (2002).
[26] K. Patil, Current Opinion in Solid State and Materials Science **2**, 158 (1997).
[27] J. McKittrick, L. Shea, and C. Bacalski, Displays **19**, 169 (1999).
[28] S. Zhao, H. Wu, L. Song, and O. Tegus, J Mater Sci (2009).
[29] S. Rasouli and S.J. Moeen, J Alloy Compd **509**, 1915 (2011).
[30] B.S.B. Reddy, I. Mal, S. Tewari, K. Das, and S. Das, Metall Mater Trans A **38A**, 1786 (2007).
[31] A.W.L. Dudeney, M. Abdel-Ghani, G.H. Kelsall, A.J. Monhemius, and L. Zhang, Powder Technol **65**, 207 (1991).
[32] F.P. Incropera, A.S. Lavine, and D.P. DeWitt, *Fundamentals of Heat and Mass*

Transfer, 6th Edition, 6 ed. (John Wiley & Sons Incorporated, 2006).
[33] R.C. Reid, J.M. Prausnitz, and B.E. Poling, *The Properties of Gases and Liquids*, 4 ed. (McGraw-Hill Companies, 1987).
[34] J.A. Dean, (1985).
[35] P.J. Linstrom and W.G. Mallard, (2001) (2001).
[36] A.V. Radha, S.V. Ushakov, and A. Navrotsky, J Mater Res (2009).

CHAPTER IV

COMBUSTION SYNTHESIS OF YTTRIUM BORATE FOR PROTON RADIATION DAMAGE STUDIES

Introduction

Scintillator materials convert ionizing radiation into visible light that can be used in a variety of analyses.[1] Materials used for scintillation are routinely exposed to radiation so must interact with but be resistant to damage from the radiation of interest. In this research luminescent materials are being developed with the opposite attributes of an ideal scintillator. We want to find a material that is robust in extreme temperatures and corrosive environments but whose luminescent properties are sensitive to radiation. Ceramics are often used in high-temperature, corrosive environments and are the focus of this work. Ceramic oxide phosphors have a large range of atomic compositions and crystal systems and can be doped with rare-elements to produce unique emission characteristics. [2-7]We have investigated yttrium aluminum garnet doped with cerium, due to its high photon yield, as a candidate for proton radiation detection. However the photoluminescent emission of this material did not change when irradiated with protons up to a fluence of $1x10^{16}$ protons/cm^2, prompting the investigation into new material systems.

The radiation sources of interest to the overall project include x-rays, protons, alpha particles, gamma rays and neutrons. The types of radiation can be used to help decide on new candidate materials to test. In particular, the susceptibility of a material to neutron

damage can help narrow the field of candidate materials. Our goal is to choose materials in which radiation will create displacement damage, resulting in long-term changes in their luminescent emission. Materials composed of elements with large neutron cross sections should have an increased probability of displacement damage from neutron radiation.

Gadolinium and boron, specifically the isotope B^{10}, have large cross sections for neutron interactions. Gadolinium is a large element and has been shown to efficiently capture thermal neutrons.[8] The inclusion of B^{10} is attractive because it has a relatively large cross section to neutrons, has a small range of reaction products, and is naturally present as ~20% of all boron.[8] Taking this information into account, yttrium borate (YBO_3, YBO) was chosen as a candidate material. The YBO framework can easily be adapted into $GdBO_3$, which would theoretically increase the sensitivity to neutrons over YBO_3, as discussed above.

YBO doped with cerium has been shown to be a poor material for both neutron scintillation and neutron storage.[8] However the authors admitted they did not optimize the synthesis, suggesting the material used for their conclusion could have been a poor representation of the material for that application. The work included a cursory radiation study, but did not systematically investigate the material's photoluminescence change with radiation exposure. We report results of a systematic study on the effect of proton irradiation on YBO PL emission intensity. The YBO used in this study was synthesized using a process optimized for PL emission intensity.

We have previously reported various aspects of synthesizing yttrium aluminum garnet (YAG) and lanthanum zirconate (LZO) using combustion synthesis. Combustion

synthesis leverages the effect of reacting a fuel and an oxidizer to produce a highly exothermic reaction to crystallize metal oxides into desired phases. Typically, metal nitrates, the oxidizers, are reacted with an organic fuel to produce ceramic oxide powders with crystal grains in the range of 15-60nm.[4,9-13] No metal nitrate is available to use in combustion synthesis of YBO. Therefore, the YBO process requires additional development beyond that used to optimize the YAG and LZO syntheses.

The lack of a boron nitrate corresponds to a reactant mixture with a decreased oxidizer to metal ratio. Therefore, less fuel could be completely combustion per metal atom, thus providing less energy to form crystalline YBO. Boric acid (HBO_3) and ammonium pentaborate ($NH_4B_5O_8$) have been used as boron sources in combustion synthesis.[14-18] Combustion syntheses using these boron sources required a secondary oxidizer and fuel. The methods for choosing the amounts of the secondary oxidizer and fuel were not reported.

This work investigated the optimization of the combustion synthesis of YBO doped with Ce and/or Eu for use in radiation studies. YBO doped with cerium was used to select the processing conditions that produce the highest normalized photoluminescence intensity. Quenching curves for YBO:Eu and YBO:Ce were developed based on materials synthesized with the optimized process. The two dopants were then co-doped into YBO to find the maximum PL emission intensity and how the dopants affect the quenching curve. Proton irradiation experiments showed both YBO:Eu and YBO:Ce have decreasing emission intensity with increasing 1 MeV proton irradiation. Radiation experiments on the co-doped material demonstrated the same trend.

Experimental Details

Material Synthesis

The combustion synthesis procedures here were similar to previous works. In short, the reactants are dissolved in water then dehydrated to a viscous solution on an 80ºC hot plate in a 125mL alumina crucible. The viscous solution is then placed in a 600°C furnace for combustion. The reactant metal sources and fuel [$Y(NO_3)_3$•$6H_2O$ (Sigma Aldrich, 99.9%), $Ce(NO_3)_3$•$6H_2O$ (Sigma Aldrich, 99.5%), $Eu(NO_3)_3$•$6H_2O$ (Pfaltz & Bauer, 99.9%), $NH_4B_5O_8$•$8H_2O$ (Sigma Aldrich, ≥99%) and glycine ($C_2H_5O_2N$, Sigma Aldrich, ≥99.0%)] were added in stoichiometric ratios to make a 0.006 mol batch according to RXN1. Pilot studies of the fuel choice looked at using urea or glycine. In those studies glycine reactions produced a porous solid where the urea reaction did not, so was chosen for this optimization study. Additionally, in previous works we have shown that glycine has a higher thermal degradation temperature than urea and due to the lack of knowledge of the ignition temperature of this new reaction the high degradation temperature could be advantageous. The optimization process will consider the use of additional oxidizer and fuel to add energy to the combustion. The oxidizer will be provided by ammonium nitrate (NH_4NO_3, Macron Chemicals, >99%). A stoichiometric reaction between ammonium nitrate and glycine was assumed to occur to add to the energy of the reaction as shown in RXN 2. For all oxidizer additions described below, fuel was added according to RXN 2.

$$Y(NO_3)_3 + 0.2NH_4B_5O_8 + 1.6C_2H_5O_2N \rightarrow YBO_3 + 2.4N_2 + 3.2CO_2 + 4.4H_2O \quad \textbf{RXN1}$$

$$4.5NH_4NO_3 + C_2H_5O_2N \rightarrow 2CO_2 + 11.5H_2O + 5N_2 \quad \textbf{RXN2}$$

Appropriate dopant amounts were added from solutions of cerium and europium nitrate at concentrations of 0.199 and 0.200 M, respectively. Two milliliters of deionized water (≥12.5 MΩcm) was added to enhance mixing and make a uniform reactant solution. The solution was then heated on an 80ºC hot plate for 15 minutes, continuously stirring with a PTFE coated stir bar producing a white paste. The crucible with the reactant was the put into a 600°C furnace for combustion.

XRD

X-ray powder diffraction was conducted using a Scintag X_1 *θ/θ* automated powder x-ray diffractometer with a Cu target, a Peltier cooled solid-state detector, and a plastic sample support. JCPDS file 16-0277 was used to identify the desired vaterite phase.

PL

Photoluminescence (PL) measurements were taken with an Avantes 2048 USB2 spectrometer. A xenon light source and a Newport Oriel 130 1/8 monochromator provided the excitation. The monochromated light then passed through one leg of a bifurcated fiber optic cable to an x-y translation sample stage. This leg of the bifurcated cable receives light reflected off of and emitted from the sample in addition to transmitting the excitation light. The sample stage was adjusted to maximize the emission intensity and minimize the reflected excitation peak before spectra were acquired.

Powders were pressed into a ~1mm deep, 2.5mm diameter hole drilled in a 1cmx1cmx0.25cm aluminum sample holder. The pressed powders were blown off with 20 psi nitrogen to remove any loose particles. These sample holders were also used during irradiation experiments.

Results and Discussion

PL Normalization

PL conditions were chosen to maximize the PL emission intensity of the synthesized material. Therefore, variations between PL spectra due to sample preparation, measurement set-up and instrumental variations must be minimized. Figure 4.1 contains an example PL spectrum. The size of the reflected excitation peak depends on the sample reflectivity, surface roughness, fiber optic cable alignment, sample preparation and other variables.

We performed a repeatability study of the PL measurement procedure using five sample holders, each containing a sample of YAG:Ce1% powder produced in one batch. Five spectra were randomly acquired from the powder in each sample holder. Thus, the study included fiber optic cable alignment, packing the sample holder, sample holder mounting and stage translation to maximize emission. The integral under the reflected excitation peak was used as the metric for this study. The variability of the area under the reflected peak for material within one sample holder was approximately ±1.1% (standard deviation divided by the mean). The variability of the area under the reflected peak for material across several sample holders was approximately ±1.6% (standard deviation

divided by the mean). This study suggests that the measurement procedure is repeatable and the majority of any observed variation in the size of the reflected peak is due to differences in sample reflectivity and surface roughness. The integral under the reflected excitation peak was used to normalize the PL spectra. The intensity at each wavelength was divided by the integral under the reflected excitation peak to facilitate a quantitative comparison of spectra.

Process Optimization

The combustion synthesis process was optimized using the addition of ammonium nitrate as secondary oxidizer for combustion and post-synthesis heat treatment of the product. The number of nitrate molecules added was based on the number of boron atoms in the batch. The ratio of ammonium nitrate molecules to boron atoms were varied from 0 (standard stoichiometry, RXN1) to 4. The corresponding stoichiometric amount of fuel was added per RXN2.

Post-process heating was performed to crystallize amorphous material and remove carbonaceous residue, which resulted from incomplete combustion of the fuel. Heat treatments were performed at 900, 1000 or 1100°C for two hours. The dopant concentration for this study was fixed at YBO:Ce4% ($Y_{0.96}Ce_{0.04}BO_3$). The cerium concentration was chosen based on quenching curves found in literature.[19]

Figure 4.2 plots normalized emission intensity as a function of nitrate to boron atom ratio and heat treatment temperature. Material synthesized using a ratio of one molecule of ammonium nitrate for every boron atom and a two-hour 1100°C heat treatment produced the highest normalized emission intensity. Without heat treatments

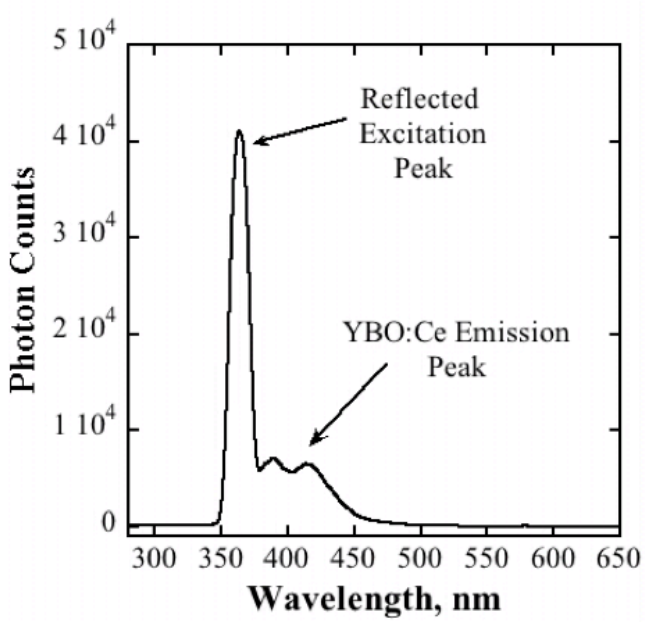

Figure 4.1. An example raw emission spectrum for YBO:Ce1% excited at 365 nm.

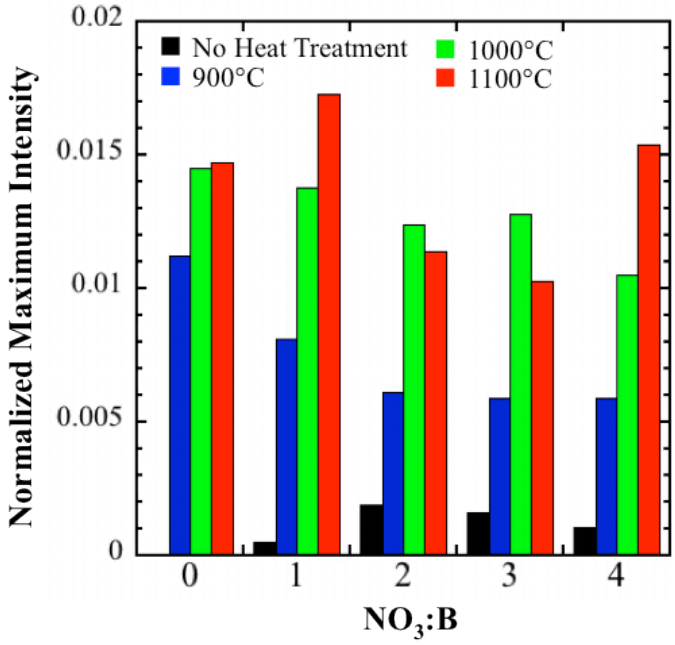

Figure 4.2. Normalized PL maximum shown as a function of chemistry and post-synthesis heat treatment performed at various temperatures for two hours.

the signal is very low for all cases. It is difficult to conclude if the low PL is due to poor crystallization or residual carbonaceous species on the powder surface. All combustions resulted in a black residue on the white YBO material. The residue could be removed after heat treatments above 700°C.

Synthesized materials were analyzed using x-ray diffraction to correlate crystal structure to their PL emission intensities. Figure 4.3a plots the as-synthesized samples' XRD patterns. The patters show varying degrees of YBO_3 are formed initially. Adding no ammonium nitrate produced material with only a small amount of vaterite as evidenced by the low signal intensity (<100 counts per second) and peak ratios do not match those expected from the standard. Chemistry ratios above zero were all primarily vaterite but none of the ratios produced the ideal YBO_3 pattern compared to JCPDS 16-0277. Intensities can be compared in this case since the sample preparation was the same for all acquisitions and each acquisition used the same amount of material. The signal intensity for ratios greater than zero were all greater than 2000 counts per second, suggesting significantly more of the vaterite crystal present after combustion with additional oxidizer. A ratio of 3 produced the smallest amount of secondary phases. From Figure 4.2, the emission intensity is weak even in the materials primarily composed of the desired vaterite crystal. While the data cannot suggest mechanisms, it does suggest the residue is having an adverse effect on PL. PL performance of heat treated samples will not have to overcome interactions with the black residue since treatments were conducted above carbon decomposition temperatures and could explain the significant jump in PL maxima shown in Figure 4.2.

The XRD of the heat-treated samples all produced YBO patterns compared to

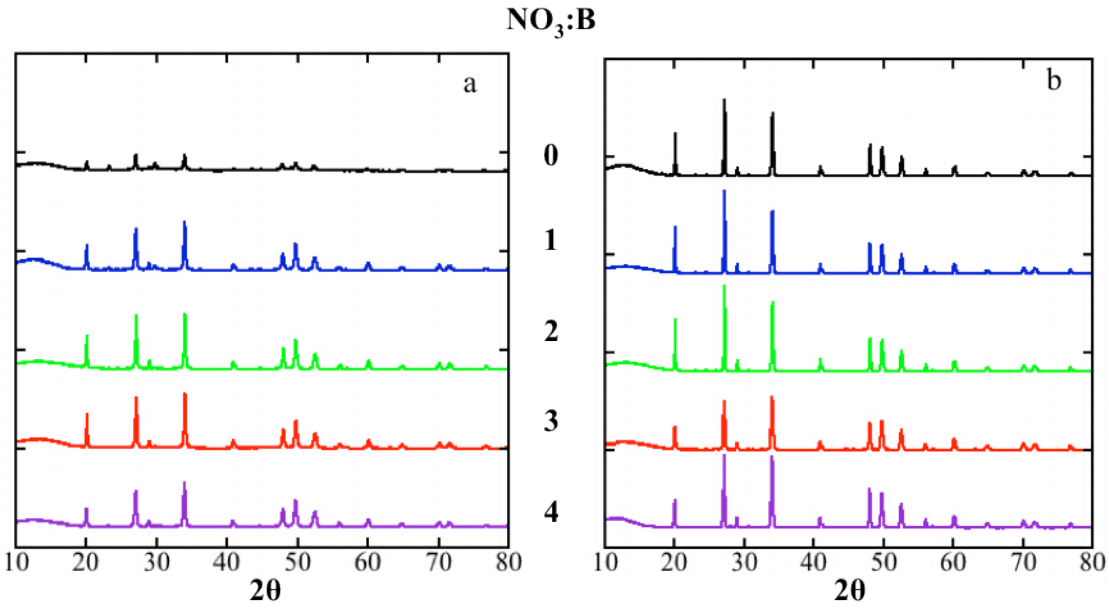

Figure 4.3. XRD patterns for (a) as-synthesized material and (b) after 1100°C heat treatment for chemistry ratios zero through four.

JCPDS 16-0277. Figure 4.3b shows the results of the 1100°C samples to compare to the non-heat-treated samples. Samples for ratios of 0-2 showed only the vaterite phase after heat treatment at any temperature. For chemistry ratios three and four, an additional peak was seen in the 900°C heat treatment data, but at 1000°C and 1100°C the peak is not present.

The lack of extra peaks at high temperatures suggests that additional crystal phases transforms to the desired vaterite phase with heating. When present, impurity signals were small compared to signal from the vaterite phase, suggesting the differences in PL are not due to undesired crystal phases. The differences in PL of the heat-treated samples could be due to other contributions such as non-uniform dopant distribution or crystal grain size. The two plots in Figure 4.3 were plotted with the same distance between baselines of the various heat treatments for both sets of data to show the relative intensity changes before and after the 1100°C heat treatment. The increase in intensity after heat treatment indicates more crystalline material, and potentially larger grains, which could contribute to increased PL intensity.

PL Quenching Curves

Quenching curves were developed for cerium and europium doped YBO synthesized using a process adding one ammonium nitrate molecule for each boron atom. A quenching curve is made to find the amount of dopant that produces the maximum photoluminescent emission from a specific crystal. In general, materials will have a different quenching curve for each dopant.

The quenching curves for YBO:Eu and YBO:Ce are shown in Figure 4.4. The 4% Ce doping level used for process optimization is also the peak of the Ce quenching curve

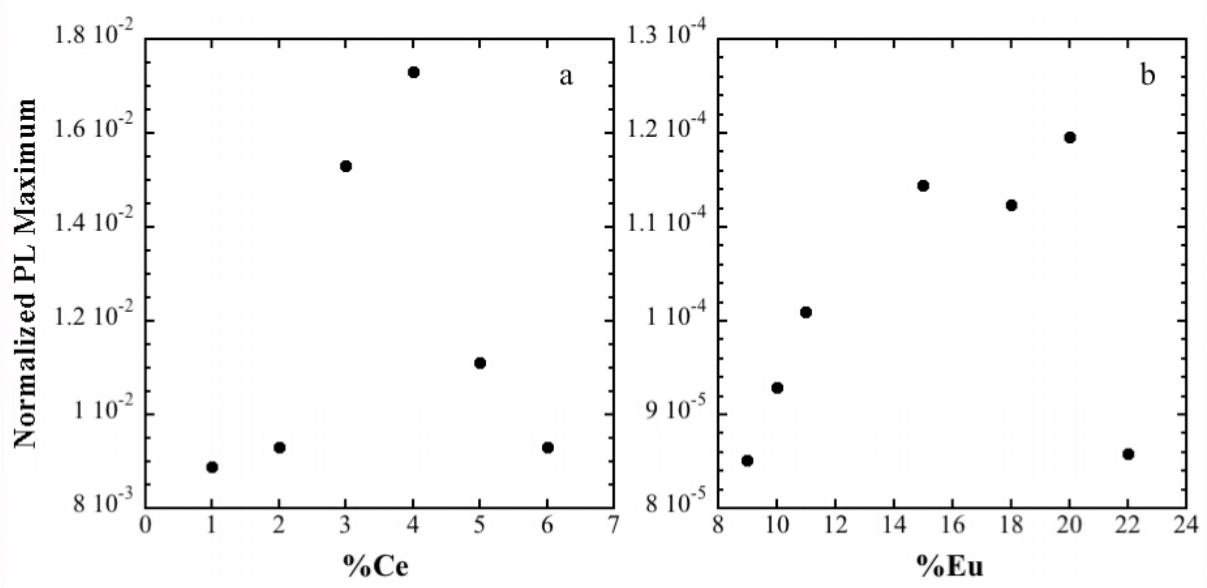

Figure 4.4. Dopant quenching curves for (a) $Y_{1-x}BO_3:Ce_x$ and (b) $Y_{1-x}BO:Eu_x$.

(Figure 4.4a). The europium quenching curve shows an optimum dopant concentration of 20%.

Quenching curves for YBO have been previously investigated and the optimal dopant concentration has been shown to depend on the size of single crystal particles. Ogata and coworkers showed that the optimum cerium concentration was 5% for large particles, but for nanoparticles (~50nm) the optimum cerium concentration was 1.25-2.5 %.[19] Similarly, Jiang and coworkers showed that for large particles an optimum europium concentration was 10% and for nanoparticles (~20nm) the optimum europium concentration was 22%.[20] The optimum Ce concentration identified by this work falls between those identified by Ogata and the Eu concentration is similar to the nanoparticle value found by Jiang. Combustion synthesis creates polycrystalline particles with a size range from the micro- to the nano- scale. The grains inside the particles are in the size range of the nanoparticles in both the Ogata and Jiang reports. The mixed particle size and grain size make drawing a parallel to the single crystal results difficult. Since these particles are polycrystalline compositions of small grains, it is not unsurprising these results do not directly correlate with large or small single crystals.

The difference between Ce quenching concentration for large and small particles is only a few percent whereas the variation for Eu is 12%. Comparing our Ce data to that of literature would suggest our quenching number is directly between large and small particles. The same comparison for the Eu curve would suggest our particles act more akin to the nanoparticles. If the combustion synthesis particles are acting more like nanoparticles it suggests the size of the particles has less of an effect on the PL performance than the grain size. This is a reasonable conclusion since PL in these

materials is generated by the interaction of a rare-earth core and the local crystal environment. However the effect of the adjacent grains and particle size on PL should not be understated. There is a significant difference between the surface area to crystal size in the nanoparticles and our polycrystalline particles. In our materials grains in the center of the particle may not emit photons that escape the bulk of the particle whereas the equivalently sized nanoparticle will emit photons from all surfaces. The described differences likely contribute to differences in the quenching curves generated here and the single crystal studies.

Radiation Damage of Single Dopant YBO

A step-stress radiation experiment was performed by taking the performance metric measurement, here PL, exposing the material to radiation to a predetermined dose and then acquiring new performance metric data for comparison. Fluence, or protons/cm^2, is how dose will be measured. Fluence is a cumulative number based on the previous dose. Tests here were conducted from 1x10^{14} to 5x10^{15} protons/cm^2. Irradiations were performed using a NEC tandem pelletron accelerator (beamline 6SDH) equipped with an Alphatross ion source to produce 1 MeV protons. A 4mm diameter beam was used in these studies so the beam diameter was greater than the powder sample size to irradiate the sample evenly.

Figure 4.6 shows the results of a step-stress irradiation experiment on YBO:Ce4%. The normalized signal intensity decreases with sample radiation above a dose of 1x10^{14}. These effects were repeatable as shown by the two samples in Figure 4.5, as well as irradiations on multiple days. A similar decrease in normalized maximum PL intensity with irradiation is seen for YBO:Eu20% which is not shown here for brevity. The

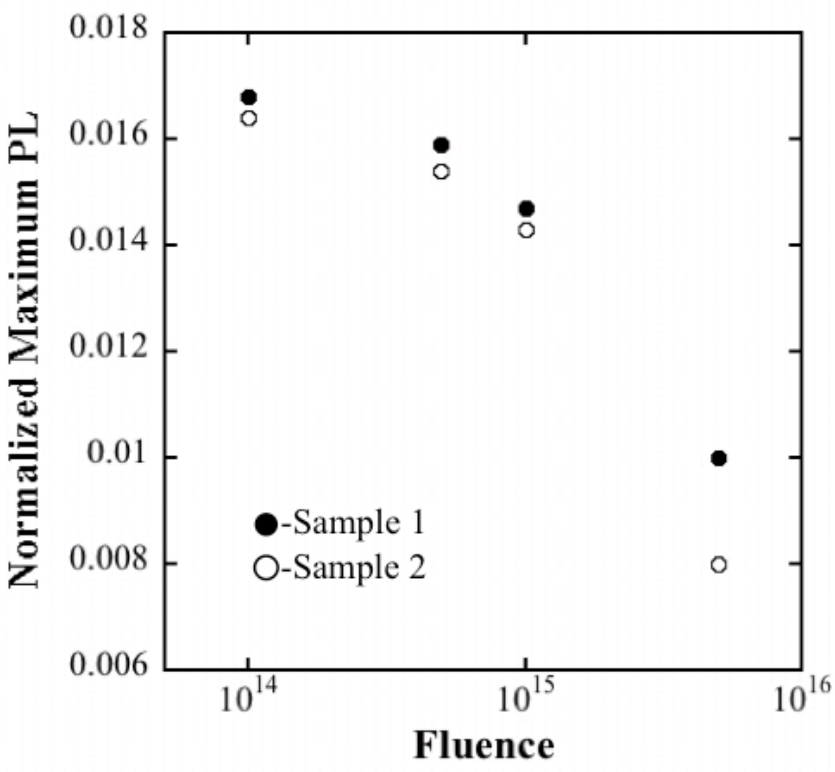

Figure 4.5. The maximum intensities of YBO:Ce4% of proton radiation for two samples irradiated on the same day.

decrease in PL intensity as a function of dose suggests protons are damaging the YBO. The data does not suggest the type of damage but the mechanisms are the interest of future work.

Co-doped YBO

Introducing a second dopant to the host crystal can change the local environment around existing luminescent cores. If the secondary dopant does influence the environment around the primary dopant its photoluminescence could change. The three possible outcomes of co-doping are for the signal to remain the same, change intensity or shift the energy of emission. To increase the signal, the new dopant must somehow constructively impact the electron network of the existing host/dopant structure that encourages energy absorbed be relaxed by emitting more photons instead of relaxing via alternative means. The neutral case would indicate the two photonic processes are completely independent of one another. The negative case indicates that the two processes actually interfere destructively, decreasing the photonic emission of both transitions.

The co-doping relationships could be used to understand radiation damage mechanisms. We showed that the normalized PL emission intensity of singly doped YBO decreases with proton irradiation. If adding a second dopant that decreases photon emission is irradiated and PL increases, then the radiation is somehow affecting the electronic network between the two dopants. If the irradiation decreases PL as seen in the singly doped material, the damage is likely affecting the entire electronic network, not just the relationship between the dopants.

Before irradiations were performed the effect of co-doping on the emission intensity of YBO was determined. Material was synthesized with 20% Eu and a range of Ce concentrations. The PL spectra were acquired using the excitation wavelength for each dopant. The results of varying the Ce concentration are summarized in Figure 4.6. The data shows that the co-doping produced a maximum for each dopant at different Ce concentration. The Eu emission reached a peak at 0.15%Ce and the Ce signal peaked at 0.75% Ce.

Europium and Ce have been shown to quench each other when incorporated into a LaB_3O_6 crystal. Pei reported the effect of Eu and Ce concentrations on the PL intensity and how PL decreases when both dopants are present. However Pei did not investigate the optimized signal intensity for either dopant so the advantageous effects of co-doping may have been overlooked.

Radiation experiments were conducted on YBO:Eu20%Ce0.75%. At these concentrations the Eu PL intensity is partially quenched and the Ce PL intensity is at its maximum. If the radiation damages the crystal near the dopants, the quenching effect of the dopants may be reduced, and a change in the relative intensities of the Eu and Ce emission may change. After irradiation both Ce and Eu PL intensities decreased similar to the singly doped materials. This suggests for these concentrations the radiation is affecting the material uniformly and does not affect the electronic network in such a way to change the interaction between dopants. Co-doped material with higher concentrations of Eu and Ce may be more amenable to radiation damage resulting in increased PL intensity. Higher concentrations would place dopant atoms in closer proximity to each other, increasing the probability of radiation damage that may interfere with the dopants'

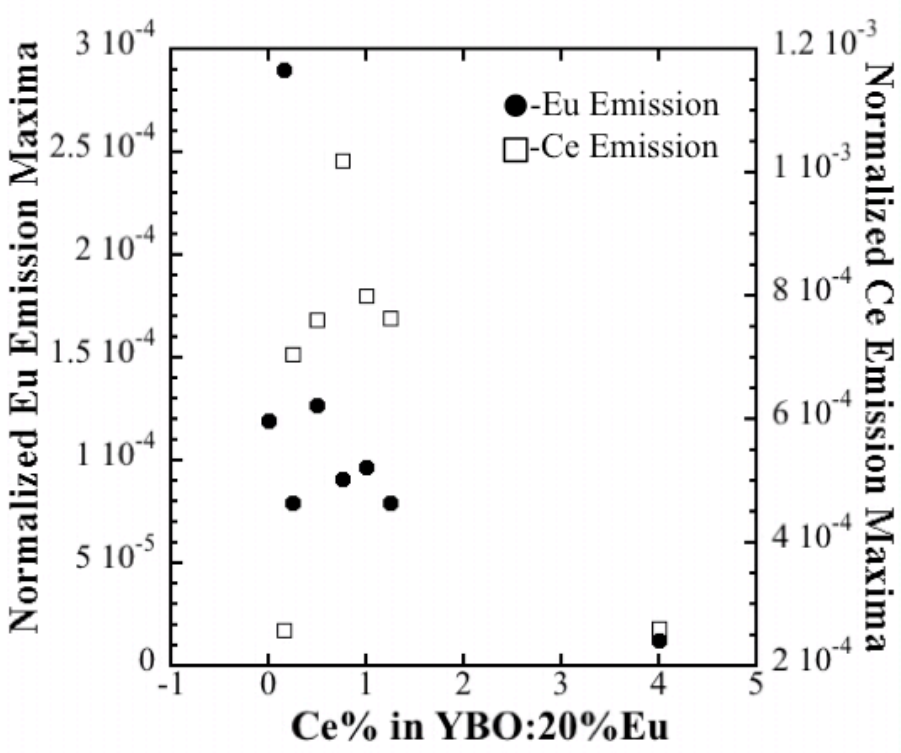

Figure 4.6. Normalized maxima for the cerium and europium emission spectra in the co-doped YBO:Eu20%CeX% materials as a function of the amount of cerium added, X.

quenching mechanism.

Conclusions

A YBO combustion synthesis process has been developed that incorporates ammonium nitrate and corresponding amount of fuel to compensate for the lack of a boron-based nitrate and corresponding amount of fuel to compensate for the lack of a boron-based oxidizer. Post-process heat treatments were also investigated. This work showed that one ammonium nitrate molecule should be added for every boron atom in the product plus a corresponding amount of fuel must be added to the synthesis followed by a two-hour 1100°C heat treatment to produce YBO with a maximum normalized PL emission intensity. Yttrium borate consists of boron and yttrium in a 1:1 atom ratio. A higher ratio of ammonium nitrate to boron atom may be needed to optimally synthesize materials with higher boron to metal atom ratios, such as LaB_3O_6.

We demonstrated that proton irradiation damaged YBO, resulting in a decrease in normalized PL emission intensity for both Ce and Eu doped YBO. Co-doping YBO with Eu and Ce increased overall photon yield over singly doped materials. Proton irradiation resulted in PL intensity decreases similar to that observed in singly doped YBO. but radiation experiments showed the same trend as mono-doped YBO. Future work is needed to understand the mechanisms of how the radiation damage decreases PL emission intensity. Other experiments that would be interesting include investigations into whether the boron is responsible for the damage or if an analogous material, such as $YAlO_3$, would be equally sensitive to the protons.

References

[1] C. Greskovich and S. Duclos, Annual Review of Materials Science (1997).
[2] S. Zhan, C. Gao, Y. Liu, and H. Zhong, J Rare Earth **30**, 995 (2012).
[3] A.L.A. da Silva, G.G.G. Castro, and M.M.V.M. Souza, J Therm Anal Calorim **109**, 33 (2012).
[4] N. Orlovskaya, Y. Chen, N. Miller, H. Abernathy, D. Haynes, D. Tucker, and R. Gemmen, Adv Appl Ceram **110**, 54 (2011).
[5] S. Rasouli and S.J. Moeen, J Alloy Compd **509**, 1915 (2011).
[6] R.P. Sonekar, S.K. Omanwar, S.V. Moharil, P.L. Muthal, S.M. Dhopte, and V.K. Kondawar, J Lumin **129**, 624 (2009).
[7] R.P. Sonekar, S.K. Omanwar, S.V. Moharil, S.M. Dhopte, P.L. Muthal, and V.K. Kondawar, Opt Mater **30**, 622 (2007).
[8] M. Knitel, P. Dorenbos, C. van Eijk, B. Plasteig, B. Viana, A. Kahn-Harari, and D. Vivien, Nucl Instrum Meth A **443**, 364 (2000).
[9] L. Yang, T. Lu, H. Xu, W. Zhang, and B. Ma, J. Appl. Phys. **107**, (2010).
[10] J. Li, Y. Pan, F. Qiu, Y. Wu, W. Liu, and J. Guo, Ceramics International **33**, 1047 (2007).
[11] R.K. Lenka, T. Mahata, P.K. Sinha, and A.K. Tyagi, J Alloy Compd **466**, 326 (2008).
[12] O. Ozuna, G. Hirata, and J. McKittrick, J Phys-Condens Mat **16**, 2585 (2004).
[13] Y. Tong, J. Zhu, L. Lu, X. Wang, and X. Yang, J Alloy Compd **465**, 280 (2008).
[14] M. Tukia, J. Holsa, M. Lastusaari, and J. Niittykoski, Opt Mater (2005).
[15] D.S. Thakare, S.K. Onlanwar, S.V. Moharil, S.M. Dhopte, P.L. Muthal, and V.K. Kondawar, Opt Mater **29**, 1731 (2007).
[16] S.-S. Yao, Y.-Y. Li, D.-H. Chen, W.-J. Tang, and Y.-H. Peng, Cent Eur J Phys **7**, 96 (2009).
[17] J. Thakur, D. Dutta, and H. Bagla, Journal of the American … (2012).
[18] S.M. Borisov, K. Gatterer, B. Bitschnau, and I. Klimant, J Phys Chem C **114**, 9118 (2010).
[19] H. Ogata, S. Takeshita, T. Isobe, T. Sawayama, and S. Niikura, Opt Mater (2011).
[20] X.C. Jiang, C.H. Yan, L.D. Sun, Z.G. Wei, and C.S. Liao, Journal of Solid State … (2003).

CHAPTER V

CONCLUSIONS AND FUTURE WORK

Introduction

This work investigated the combustion synthesis of three potential ceramic oxide phosphors for radiation detection. Desired characteristics for the materials were the opposite of scintillators in that we wanted interactions between radiation and our materials to produce long-term damage. We used the photoluminescence emission intensity as the metric for process optimization and to indicate radiation damage. The materials investigated were yttrium aluminum garnet (YAG), lanthanum zirconate (LZO) and yttrium borate (YBO). Each material provided unique opportunities for process optimization. Radiation studies were conducted on materials produced by their respective optimized processes.

Summary of this Work

YAG and LZO Processing

Combustion synthesis leverages the highly exothermic reaction between a fuel and oxidizer to heat the material of interest to crystallization temperatures. The fuel and oxidizer mixture can impact the energy released by the reaction, leading to differences in crystal phases formed directly from the reaction. The fuels can also coordinate with other reactants, such as metal nitrates, to solubilize the reactant or help distribute the dopant more evenly in the final material.

Urea and citric acid were mixed to investigate the effect of fuel selection on the synthesis of YAG:Ce1%. Urea typically combusts with the YAG reactants to provide a high flame temperature and citric acid is considered a chelating agent, assisting in dopant distribution in the final product. We hypothesized that mixing the fuels would lead to a higher normalized PL emission intensity than either pure fuel could produce. To fully understand the implications of the synthesis chemistry on final product, post-synthesis heat-treatments were also investigated up to 1100°C.

Materials were synthesized with both pure fuels and several mixtures of fuels and the PL dropped for all fuel mixtures. Mixing fuels decreased PL emission intensity from the pure fuels. To understand why, powder x-ray diffraction (XRD) and x-ray photoelectron spectroscopy (XPS) were used to characterize the materials and understand the impact of the processing conditions on the material. XRD indicated that without heat treatment the pure citric acid material was amorphous but after heating produced pure-phase YAG crystals. Pure urea initially creates a mixture of phases that can be driven to the YAG phase with heat-treatments. XPS provided insight into the chemical bonding environment and showed that the most pure phase material is the material produced form citric acid heat-treated at 1100°C. However the highest PL material came from the urea reaction after an 1100°C heat treatment. We argued that because crystal grains were of similar size, being both made primarily of YAG and no impurities identified that the differences in PL are likely due to dopant distribution issues.

When synthesizing materials it was found that changing the reaction vessel could change the phases formed the YAG formed directly from combustion with urea. A lumped capacitance model described differences in heating, showing more heat would

enter the 225 mL crucible but less heat would leave the 125 mL crucible. This result, along with literature suggesting furnace temperature can affect the synthesized material, prompted a study of the heat released by the reaction via thermogravimetric analysis (TGA) and differential scanning calorimetry (DSC). The TGA data suggested that reactants degrade before ignition, which should negatively affect the reaction energy. From the DSC data, energy released by the reaction was calculated and at ramp rates below 10°C/min the energy is below the optimum that occurs at 10°C/min. Above 10°C/min reaction energy decreased. We suggest that the reaction energy decreases due to thermal gradients producing small ignitions at various points across the reactant volume instead of one large combustion. The non-uniform ignition would decrease the reaction energy, as the energy would not entirely go towards material crystallization but to other processes such as heating the neighboring reactant material.

Higher reaction energies should correspond to materials with more crystalline material. Transmission electron microscopy (TEM) investigated the material produced in TGA/DSC experiments and found that the 10°C/min produced the most crystalline material.

This analysis was compared to LZO and YAG combusted with glycine to compare the effects of heating rate. The LZO system was found to be analogous to YAG combusted with urea, producing a maximum amount of energy released at 10°C/min. Similar thermal degradation of reactant materials could be occurring in the LZO system, and then at high temperature ramp rates suffers from non-uniform ignition. YAG combusted with glycine produced a maximum amount of energy at the lowest ramp rate tested of 2°C/min. This system should suffer from significant reactant degradation of the

$Al(NO_3)_3$ molecule since the ignition point is higher than that of the urea combustion, but appears to produce the most energy by heating slowest. It is unclear why the trend is different.

YBO Synthesis and Irradiation

The synthesis of YBO was different from the others due to the lack of a boron nitrate. Ammonium pentaborate was substituted and the process optimized for the addition of ammonium nitrate (oxidizer) and appropriate amount of fuel. The optimized processing was then used to investigate a quenching curve for YBO:Eu, YBO:Ce and found the maximum emission intensity was at 20%Eu and 4% Ce, respectively. Co-doped material was also investigated and found to increase PL emission intensity. Singly-doped and co-doped material was damaged with proton irradiation, but they were both damaged the same and mechanisms could not be proposed.

Future Work

Based on the experiments and experience gained in this work, we make the following suggestions for follow-up work:

(1) Synthesis of $GdBO_3$ for proton and neutron radiation experiments. The optimization processes described here should produce $GdBO_3$ just as YBO but the larger gadolinium could help increase the sensitivity of the material to proton radiation.

(2) Synthesis of LaB_3O_5 to investigate the effect of additional boron atoms on the radiation response. Intuitively, adding boron to the host crystal should decrease sensitivity to protons since the cross-section for interaction is low. However, the

additional boron could increase neutron sensitivity. Some pilot processing studies would need to be conducted similar to Chapter IV to understand the effect of additional boron atoms with no associated oxidizer for reaction.

(3) Further transmission electron microscopy studies to understand why there are differences in YAG produced with different fuels. Pilot EDS studies have been conducted but are inconclusive. Even though inconclusive, the data shows the applicability of the technique to our materials and when the analysis process is optimized for our materials should yield more information.

(4) Particle size control is and should continue to be investigated. The particle size can have an effect on the PL emission characteristics but may also make the material more sensitive to radiation. Currently, the large particles could be hindering radiation sensitivity as measured by PL due to the polycrystalline nature of the particles and decreased surface area of the existing grains. If particles size could approach the grain size the radiation may provide a more pronounced effect on the PL emission.

(5) Investigation of oxide ceramics for catalysis purposes could continue this work with new purpose. The materials here were all valued as phosphor materials, but the synthesis framework could be applied to catalysis oxides opening research collaborations and field of study.

APPENDIX I

X-RAY PHOTOELECTRON SPECTROSCOPY STUDY OF CHARGE EFFECTS ON IONIC LIQUID THIN-FILMS

Introduction

Room temperature ionic liquids (ILs) are ionic compounds that are liquids at ambient conditions. These compounds are comprised of bulky, asymmetric organic ions that cannot pack effectively, resulting in low melting temperatures[1, 2]. Many properties of these ionic compounds are determined by the structure of the ions and the cation-anion combination. ILs are non-combustible, have a wide electrochemical window[1], and have a negligibly low vapor pressure[3-5]. ILs have been used as nonvolatile solvents, electrolytes, and lubricants[1, 2, 6].

The efficacy of an ionic liquid in many applications is dependent on the liquid's surface chemistry and the packing of the ions. For example, in tribological applications, the surface chemistry of a room temperature ionic liquid can influence frictional interactions between the film and moving parts. Additionally, the packing of the ions in the ionic liquid could affect the wear resistance of the film in tribological applications.

X-ray photoelectron spectroscopy (XPS) can determine the surface chemistry and the elemental composition with depth into thin films. Since XPS is an electron spectroscopy, it is carried out under ultra-high vacuum conditions. Even though IL films are liquids, the very low vapor pressure of many of the IL compounds enables them to be

vacuum compatible, and therefore amenable to XPS analysis. XPS analysis involves irradiating a sample with soft x-rays, often Al kα (1486.6 eV). These x-rays ionize a core shell of a target atom, ejecting a photoelectron whose kinetic energy is related to the characteristic binding energy of an electron in the atomic orbital from which it was ejected. This binding energy can identify the element from which the electron was ejected as well as, in many cases, the bonding environment of that atom. For example, the binding energy of a C 1s electron emitted from a carbon atom in a $(–CH_2\text{-}CH_2\text{-})_n$ type bonding is approximately 284.8 eV, while the binding energy of a C 1s electron from a carbon atom in SiC is approximately 281.3 eV.

The surface of a sample can build up charge during XPS analysis due to the loss of photoelectrons from the sample. Electrically isolated samples can accumulate a significant amount of positive charge, resulting in electron kinetic energies less than their theoretical values. Thus, the entire binding energy spectrum would be systematically offset from theoretical values. In extreme cases, surface charging can result in undecipherable XPS spectra. If surface charging is uniform, sufficiently small, and the sample contains a known elemental transition, the resulting spectrum can be shifted in energy such that the known elemental transition occurs at it theoretical binding energy. Typically the C 1s in adventitious hydrocarbon transition is used and set to approximately 284.6 eV. Instrumental techniques have also been developed to neutralize sample charging during XPS analyses. The majority of currently used charge neutralization techniques involve flooding the sample surface with low energy electrons to replace the electrons ejected from the sample. Some XPS instruments are equipped to with low energy Ar^+ ion guns, and/or UV lamps to be used in in concert with the low energy

electron guns for improved charge neutralization. These instrumental technics are very effective. However, fine-tuning of a spectrum's energy scale is typically accomplished by shifting the spectrum to a known elemental transition.

One might expect that XPS analysis of ionic liquid films would be more challenging than the analysis of typical solid samples. The ionic nature of ILs might make them react to ion, electron, and/or x-ray beams due to coulombic interactions. Also, since ILs are fluids, IL films could migrate due to various driving forces. We have observed unusual behavior of a thin 1-butyl-3-methylimidazolium hexafluorophosphate film on silicon during XPS analysis. The overall photoelectron signal intensity significantly decreased throughout the collection of high-resolution spectra. A survey spectrum showed that the intensities of the fluorine and carbon peaks were less intense than those in a survey collected prior to collecting the high-resolution spectra, while the silicon peaks were more intense than those in the initial survey spectrum.

The observed changes in peak intensities between the two survey spectra could be explained by x-ray decomposition of the IL into volatile species, resulting in a thinner film and a more intense signal from the silicon substrate. Keppler and coworkers showed using mass spectrometry that a monochromatic x-ray beam can cause ionic liquid fragmentation and desorption[7]. However, if species were volatilizing off our sample the pressure in the analysis chamber should increase, which was not seen. The chamber pressure stayed constant at 9.0×10^{-9} Torr, providing no evidence of film degradation.

Since there was no evidence of film desorption, we investigated if the IL had flowed away from the analysis area, or balled-up to expose the silicon substrate. Optical observation around the x-ray spot suggested the film pulled away from analysis area

during the analyses. We hypothesize the ionic liquid moves due to interactions with the charged species used for charge neutralization (electrons and Ar^+) and the photoelectrons induced by x-rays during the XPS analysis. XPS analyses of thick IL films have been reported, but neither bulk liquid movement nor ion rearrangement in the IL film during XPS analysis has been reported[1-5, 7-13].

In this work we investigate the interactions between nominally 150 nm thick 1-butyl-3-methylimidazolium hexafluorophosphate films with the x-ray beam, the electron beam and the argon ion beam during XPS analysis. The anion and cation in this IL contain different elements, enabling us to determine the relative orientation of the cations and anions in the film from the XPS spectra. We show that the initial films are not continuous, but the drops can be spread via Ar^+ irradiation. We also show that the cation preferentially segregates to the liquid/vacuum surface upon negative surface charging. Tribological measurements performed on the droplet and smoothed films showed the smoothed films had increased durability over the droplet films.

Experimental

Materials and Methods

Water used in all experiments was deionized (DI) and purified to 16.7 MΩ·cm with a Modu-Pure system. All reagents were used as-received. 2-Propanol (>99.8%, IPA), ethanol (99.5%) and 1-butyl-3-methylimidazolium hexafluorophospate ([BMIM][PF_6]) were purchased from Sigma Aldrich. Sulfuric acid (H_2SO_4, 17.8 M) and hydrogen peroxide (35 wt% H_2O_2/65% H_2O) was purchased from Fisher Chemicals. (100) Silicon wafers were cut into approximately 1 x 1 cm samples, sonicated in ethanol for 30 min,

rinsed with ethanol, and dried in a stream of nitrogen before being treated with piranha solution (70% H_2SO_4/30% H_2O_2) for 30 min, rinsed with water, and dried in a stream of nitrogen. To form a nominally 150 nm films, 20 μL of a 3.609 mM [BMIM][PF_6] in 2-propanol solution was drop cast on freshly piranha-cleaned silicon and placed in a vacuum chamber. The chamber was sealed and left under vacuum for 2 hours. Optical images were taken through a Nikon L-UEPI microscope with Scion Viscapture version 1.1 software and a Scion 1394 camera with 10x magnification.

XPS Analysis

XPS analyses were performed using a Physical Electronics (PHI) 5000 VersaProbe. Monochromatic Al Kα x-rays (1486.6 eV) were used. Analysis was done on a 200μm, 50W x-ray spot with photoelectrons collected into a spherical capacitor analyzer in constant pass energy mode at a take-off angle of 45 degrees to sample normal. The linearity was adjusted such that the $Au4f^7/_2$ and $Cu2p^3/_2$ peaks were separated by 848.6 eV and work function adjusted such that the $Ag3d^5/_2$ peak was at 368.28 eV. High resolution and survey spectra were collected using 23.5 and 187.8 eV pass energies, respectively. 1.1 eV electrons and 10eV Ar^+ ions were used to irradiate the samples. The Ar^+ beam was rastered over a 1.0 x 1.0 cm area to irradiate the entire substrate. The Ar^+ beam current density was approximately $5x10^{-5}$ pA/μm^2 as measured into an 800 μm diameter Faraday cup. Data reduction was performed using CasaXPS and PHI Multipak.

Tribology

Microscale friction measurements were performed in a Center for Tribology (CETR) UMT-2 Micro-Tribometer equipped with a DFM-0.5 sensor and interfaced to a

personal computer. The stainless steel ball bearing probe (4 mm in diameter and root mean square roughness of 15 ± 3 nm) was attached to the sensor via a suspension-mounting cantilever. A normal load of 400 g (3.92 N) was applied on all samples. Experimental conditions were set as follows: testing distance = 4 mm, speed = 0.1 mm•s^{-1}, temperature = 22 ± 1 °C.

Results and Discussion

Film Formation

Figure 1 contains optical photographs of nominally 150 nm thick [BMIM][PF_6] films drop cast at different times. We define film thickness as the nominal thickness that would be created by a known volume of [BMIM][PF_6] uniformly wetting a 1 x 1 cm sample surface. While a similar procedure was used to create both batches, a larger vacuum chamber was used to dry Batch 2 than that used for Batch 1.

The average surface coverage of droplets was determined from 5 points across a sample for films from each batch. The average droplet surface coverage of Batch 1 and Batch 2 films was 35±4% and 15.8±3%, respectively. Figure 2 contains an XPS survey spectrum of an as-deposited sample from Batch 1 and sketches of the PF_6 and BMIM ions' structures. The survey spectrum only contains peaks from elements present in the [BMIM][PF_6] molecule, and oxygen and silicon from the substrate. XPS survey spectra of all as-deposited samples contained silicon peaks, confirming that the films were not continuous. The intensity of the silicon peak in the survey spectrum of the film from Batch 1 was less than that of the silicon peak in the spectrum of the film from Batch 2.

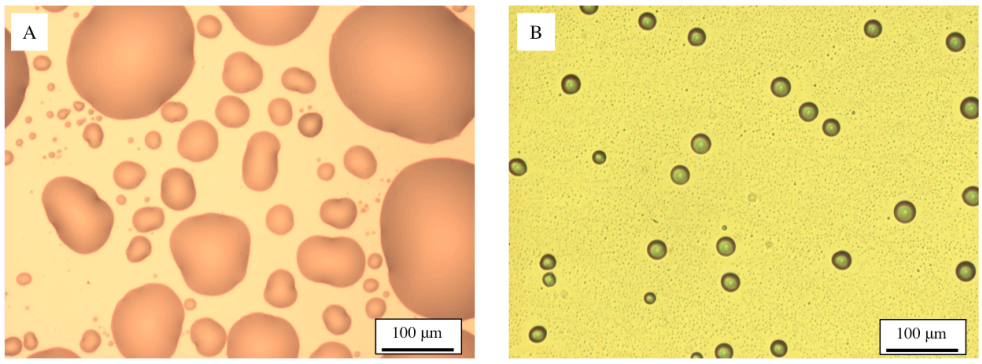

Figure 1. Comparison of droplet distribution from (A) batch 1 and (B) batch 2.

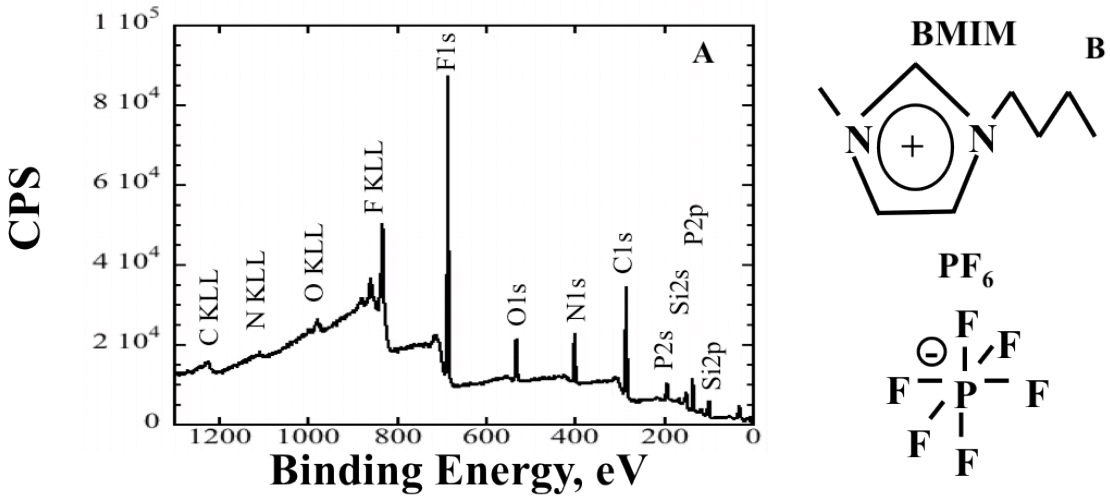

Figure 2. (A) Survey of a dropcast IL droplet film. (B) Example schematic of the molecules [BMIM] and [PF_6].

This is consistent with the surface coverage measurements and suggests there is no IL between the droplets on these samples.

XPS Induced Charging

We investigated the time dependence of high-resolution F1s, C1s, and Si2p spectra acquired from [BMIM][PF_6] films irradiated under four conditions: 1) with x-rays, 2) with x-rays and electrons, 3) with x-rays and Ar^+ ions, or 4) with x-rays, electrons, and Ar^+ ions. Spectra were acquired approximately every ten minutes for up to ten hours. Spectra were acquired using the same radiation conditions under investigation. Figure 3 plots the areas under the F 1s, C1s, and Si2p spectra as a function of irradiation time and conditions. Areas were normalized using handbook sensitivity factors[14] to compensate for possible changes in total photoelectron current due to instrumental drift over the extended irradiation time.

The changes in the relative intensities of the F1s, C1s, and Si2p signals over time can indicate bulk flow of the IL droplets and/or rearrangement of the ions within the droplets. In the case of irradiation by x-rays only (Figure 3A) the Si2p intensity slowly increases approximately 11% throughout the analysis. This suggests the surface coverage of the IL drops decreased during the experiment. This decrease in surface coverage could be due to Ostwald-type ripening of the droplets, where small drops are driven by surface energy minimization forces to incorporate into larger droplets. The ratio of the C1s to F1s signal intensities remain roughly constant during the analysis, suggesting the orientation of the ions within the drops also remained constant. In the case of irradiation with x-rays and electrons (Figure 3B) the intensities of the Si2p, C1s, and F1s signals are

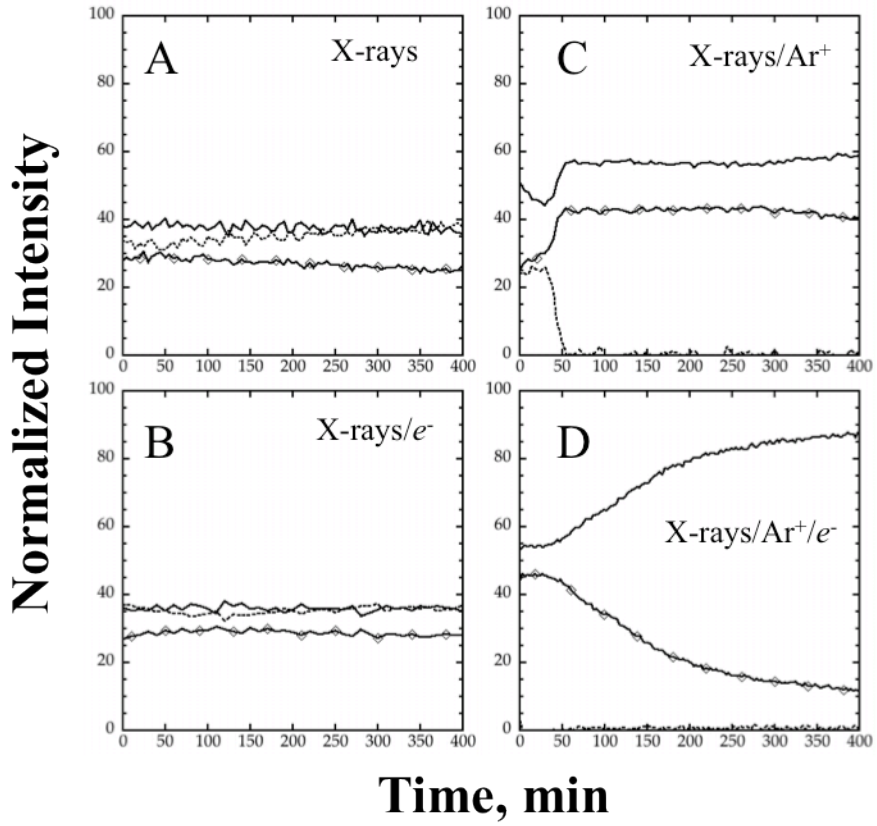

Figure 3. Time dependent spectra of various charging regimes on the ionic liquids. X-rays alone (A), with electrons (B), with Ar^+ (C), and with electrons and Ar^+ (D). XPS transitions shown are C1s (-), F1s (—◇—), and Si2p (---).

all roughly constant throughout the experiment. These data suggest that under both x-ray and electron beam irradiation neither bulk flow of the droplets nor rearrangement of the PF_6 and BMIM ions inside the droplets occurs.

Argon ion irradiation induces significant changes in the F1s, C1s, and Si2p signal intensities over time. The Si2p signal intensity drops to zero within approximately 80 minutes of irradiation with x-rays and argon ions (Figure 3C). The Si2p intensity drops to zero immediately upon irradiation with x-rays, electrons, and argon ions (Figure 3D). The loss of the Si2p signal intensity in both of the radiation scenarios including argon ions suggests that the IL droplets have spread to cover the entire analysis area with a film thickness on the order of 9.5 nm [15] or greater. In the cases of irradiation that includes argon ions, we believe bulk fluid flow and not Ostwald-ripening effects due to the significant amount of mass transfer needed to cover the analysis area. Figure 4 contains an optical photograph of an Ar^+ irradiated sample from Batch 2 that confirms the droplets have spread. The bottom left corner of the image is an area outside the analysis area, and therefore not irradiated. This portion of the sample appears similar to the sample shown in Figure 1B. The top right part of the image was within the analysis area and was irradiated. The distinct droplets seen outside the analysis area are not present within the analysis area. We believe that the darker, hazy spots seen in the analyzed area are droplets that have not entirely spread, and thus are areas where the film is thicker than those around them. While the change in surface morphology is induced by argon ion irradiation, the films do not spontaneously revert to the as-deposited droplet form when the radiation is stopped. Samples have been observed with the "spread film" morphology more than three months after being removed from the XPS chamber.

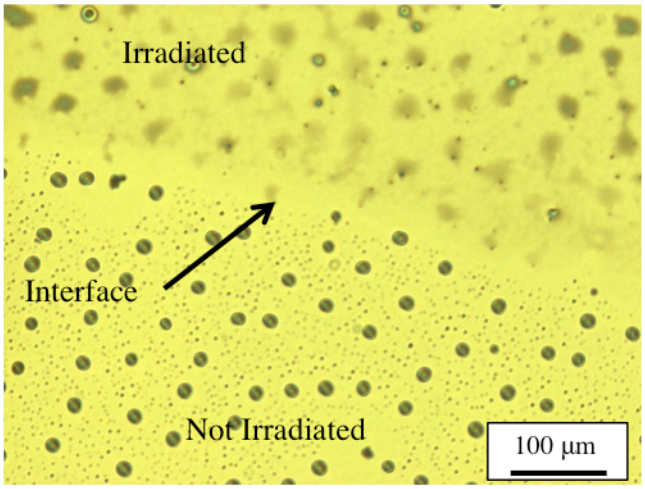

Figure 4. Optical image of IL film after irradiation. The Ar^+ only interacted with the top right of the picture, showing the droplets are unaffected unless irradiated with Ar^+.

The equilibrium composition of the surface of ILs has been previously reported. Faulkner and coworkers showed that fluorinated species preferentially populate liquid/vapor (l/v) interfaces[1]. Lockett and Palacio showed that anions prefer the l/v surface and BMIM the liquid/solid (l/s) interface[12, 13]. Therefore, the PF_6 ion in our system should preferentially populate the l/v interface, and the BMIM should preferentially populate the l/s interface. However, during the first 80 minutes of x-ray and argon ion irradiation the ratio of the C1s and F1s signal intensities vary, but this ratio remains constant throughout the remainder of the experiment. In the case of x-ray, electron, and ion irradiation the C1s to F1s signal intensity ratio is roughly constant for the first approximately 50 minutes, but then increases roughly linearly throughout the remainder of the experiment. The changing C1s to F 1s signal intensities in these two ion irradiation cases suggests that the PF_6 and BMIM ions are rearranging within the droplets along with the bulk fluid flow discussed above.

Accumulation of charge on the droplets' surfaces could drive the rearrangement of the ions in the drops. Accumulation of positive charge on the droplets' surfaces should attract the PF_6 anions to the l/v surface. However the PF_6 ions preferentially populate the l/v surface so we should not observe a change in surface chemistry with a positive charge accumulation on the droplets' surfaces. This suggests that irradiation with just x-rays or x-rays and electrons either accumulates positive charge or no net charge. If a negative charge accumulates on the droplets' surfaces the positive BMIM ions should be attracted to the l/v surface and the PF_6 ions should be repulsed away from l/v interface. The C1s to F1s signal intensity ratio for the case of irradiation with x-rays and ions decreases from 1.7 to 1.3 over the first 80 minutes of the experiment. The decrease in this ratio could be

due to accumulation of a small positive charge on the droplets' surfaces, which would attract the PF_6 ions towards the surface. Another explanation for the decrease in the C1s to F 1s signal intensity ration is tied to the bulk flow discussed above. The surface of the exposed silicon substrate would most likely have adsorbed hydrocarbons, which would increase the C1s signal intensity. As the fluid flowed from the droplets to cover the silicon substrate the contribution of this adventitious carbon to the C1s signal would decrease. The covering of the exposed silicon substrate would lead to a decrease in the C1s to F1s signal intensity ratio. Once the surface was completely covered the ratio would remain constant if the ions did not rearrange inside the fluid. The data in Figure 3C supports this explanation. The continuously increasing C1s to F1s signal intensity ratio for the case of x-ray, electron, and ion irradiation suggests that a negative charge is accumulating on the fluid's surface, even after it spread across the silicon substrate. The negative surface charge drives the BMIM ions toward the l/v surface, displacing the PF_6 ions.

The spectra collected at different time points during the irradiation experiments support the conclusions about surface charge accumulation. Figure 5 contains C1s spectra acquired after 0 and 180 minutes of irradiation and an hour after the end of irradiation for the cases of irradiation with x-rays and ions and x-rays, ions, and electrons. Figure 5A is a C1s spectrum collected from bulk [BMIM][PF_6] acquired under no charge accumulation conditions. The spectrum of the bulk liquid is fitted with peaks representing C-C bonding (284.8 eV) and three C-N bonding configurations (286.4, 286.0 and 287.2 eV) corresponding to the molecular structure shown in Figure 2.

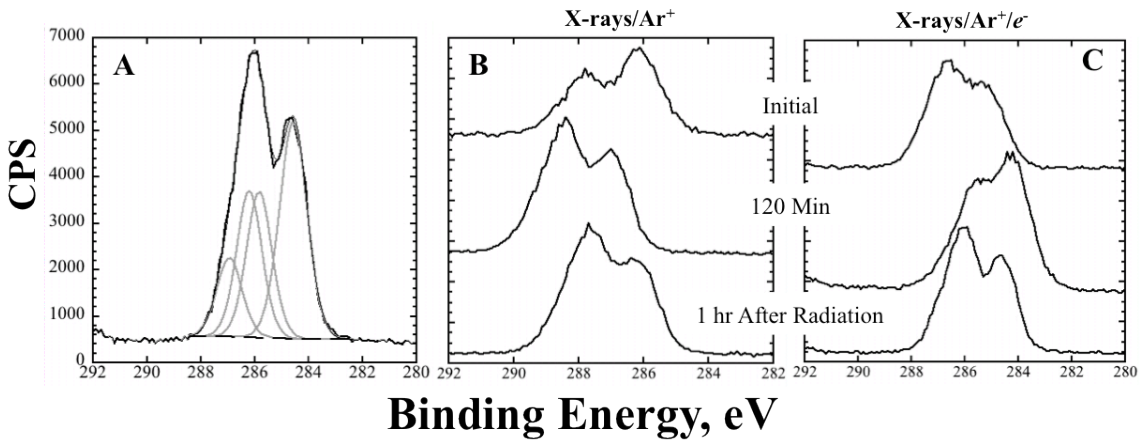

Figure 5. A deconvoluted C1s spectra for a bulk [BMIM][PF_6] film (A) and C1s spectra for x-rays/Ar^+ (B) and x-rays/e^-/Ar^+ (C) at various times of irradiation.

Figure 5B contains the C1s spectra collected during the x-ray and ion irradiation experiment. Before irradiation the contribution of C-C bonding (around 284.2 eV) has a greater contribution to the spectrum compared to the reference spectrum (Figure 5A). The increased C-C contribution is most likely due to adventitious hydrocarbon adsorbed to the exposed silicon surface. The entire spectrum's binding energy scale has shifted positively by approximately 0.8 eV after 180 minutes of irradiation. However, this spectrum exhibits the same general shape as that of the reference spectrum. The corresponding F1s spectrum's (not shown) binding energy range also shifted by approximately 0.8 eV, which is consistent with the conclusion that the energy shift is due to positive charge accumulation on the droplets' surfaces due to photoelectron emission and the argon ion bombardment. The accumulation of a positive charge indicated was also reported by Villar-Garcia[10]. The shape change in the spectrum is due to the spreading that occurs, covering the silicon surface and other adventitious hydrocarbon species. The spectrum acquired 60 minutes after irradiation returned to the pre-irradiation binding energy range but with a shape similar to the reference spectrum. The shape of the post irradiation spectrum supports the assumption that initial high C-C bonding contribution was due to adventitious hydrocarbon adsorbed to the exposed silicon surface.

Figure 5C contains C1s spectra collected during the x-ray, ion, and electron irradiation experiment. The spectrum's initial shape is consistent with that of the reference spectrum. The C1s binding energy range and the corresponding F1s binding energy range (not shown) shift negatively approximately 1.2 eV after 180 minutes of irradiation. The reduction in binding energy is consistent with negative charge

accumulation on the liquid's surface. After 180 minutes of irradiation the C1s spectrum shows increased C-C contribution and decreased C-N contribution compared to spectrum acquired before irradiation. The increased C-C signal suggests the aliphatic portion of the BMIM ion has oriented toward the surface. The spectrum would have a shape similar to the reference spectrum if the BMIM ion had not preferentially oriented itself at the l/v surface. The spectrum attains the shape of the reference spectrum 60 minutes after irradiation.

Spreading

We have demonstrated that bulk liquid flow as well as ion rearrangement within the liquid film can occur during irradiation of IL films. Our experiments showed that bulk flow only occurred when ions were included in the irradiation. We performed basic calculations to better understand the droplet-spreading phenomenon.

Equations 1 and 2 [16] were used to estimate the work of adhesion assuming that the adhesion between the IL droplets and the silicon surface is only due to dispersive energy.

$$\cos\theta = -1 + 2\left(\frac{\gamma_s^d}{\gamma_{lv}}\right)^{\frac{1}{2}} \qquad \text{E1}$$

$$W_A = \gamma_{lv}\left(1+\cos\theta\right) \qquad \text{E2}$$

θ is the contact angle between the droplet and the surface, γ^d_s is the dispersive force on the silicon surface (36.5 dyne/cm as estimated by Zhao [19]), γ_{ls} is the surface tension of the IL (48 dyne/cm [17, 18]), and W_A is the work of adhesion in dynes/cm.

Energy added due to ion bombardment was assumed to be the only energy contributing to the spreading affect. A current of 25 pA of 10 eV Ar^+ was measured into an 800 μm diameter faraday cup. Uniform bombardment across the entire 1 cm x 1 cm sample surface was assumed, resulting in energy being added to the surface at a rate of $5x10^{-8}$ J/s. W_A can be converted to N•m by multiplying by the interfacial area of the IL calculated assuming the surface coverage of IL on a 1x1 cm^2 area. Dividing W_A by the rate of energy deposition estimates the time needed to accumulate the energy to overcome the work of adhesion for a specific surface coverage of IL. For these tests, only the x-ray was used during analysis in order to get a more accurate portrayal of irradiation time.

The experimental times for these tests show that the model underestimates the time needed to overcome adhesion though the estimate was supposed to be on the high end. This simple model likely fails because the system is actually complex due to different charging characteristics on the droplets and on the adjacent bare silicon surface. The two surfaces charging differently could cause spreading characteristics to diverge from the assumption that only dispersive forces are keeping the droplets from spreading. Additionally, because the Ar^+ beam was turned off during XPS high-resolution analysis and rastered during irradiation, the system had some time to relax, which could result in longer irradiation times for coalescence than if the beam was left focused on one spot and not turned off.

It is important to note that the spreading phenomena was stable in air for at least 2 months. The imaging and tribology of these samples were delayed after the droplets had spread, so this is a long-term morphology change.

Table 1 shows the estimated times of irradiation to deposit enough energy to overcome the work of adhesion and the experimental times for spreading. The experimental times were determined using samples from Batch 2 due to their more uniform droplet distribution.

Tribology

Figure 6 plots the coefficient of friction (COF) of a bare silicon wafer, an IL droplet film on silicon, and IL films spread on silicon with x-ray/Ar^+ and x-ray/Ar^+/e^-. Initial COF measurements of the droplet and spread films showed little difference but were well below the COF of bare silicon. The spread films produced low COF over a longer period of time than the droplet films, lasting 60% longer in the test of 100 cycles. This increase in durability is likely due to the IL being spread more evenly than the droplet films where the probe could push the IL out of the probe path. As the probe repeated the cycle many times the probe path could eventually be bare of IL, which appears to be the case by the COF returning to that for bare silicon.

Summary and Conclusions

An XPS analysis of 150 nm IL thin films was presented as a function of radiation time. We showed that by irradiating droplet IL films with charged particles the liquid could be induced to move across a surface. The IL was spread into a film in an irreversible way. We also demonstrated that charges applied to a surface can alter the composition and orientation of the IL at the interface. For the [BMIM][PF_6] IL used here, it was easy to differentiate between the anion and cation. While the changes in surface

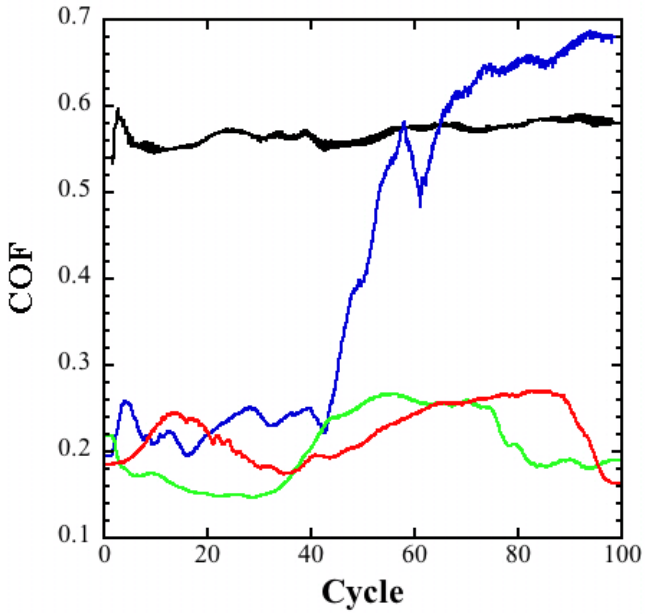

Figure 6. Moving average tribology results for (black) bare silicon, (blue) as-dropcast droplets, (green) spread film of IL using only x-rays and Ar^+ ions, and (red) spread film of IL using x-rays, Ar^+ ions and electrons.

composition would be more difficult to identify for an IL pair with two carbon-based molecules, the ability to manipulate the surface composition should hold across other ILs. Depending on the surface tension of the IL tested the spreading of droplet films could happen at different speeds from the IL tested here. Being able to spread the films can provide an important perspective during tribology studies when looking at the durability of the molecule over the durability of the deposition technique to understand the limits of ILs as a lubricant.

Tables

Table 1. The time for coalescence and actual time until coalescence occurred.

Sample	Radiation	Time (Estimated, min)	Time (Experimental, min)
S2	x-ray/e^-/Ar^+	46	300
S3	x-ray/e^-/Ar^+	53	400
S4	x-ray/Ar^+	39	75
S5	x-ray/e^-/Ar^+	42	150

References Cited

1. Faulkner, C.J., R.E. Fischer, and G.K. Jennings, *Surface-Initiated Polymerization of 5-(Perfluoro-N-Alkyl)Norbornenes from Gold Substrates.* Macromolecules, 2010. **43**(3): p. 1203-1209.
2. Gottfried, J.M., F. Maier, J. Rossa, D. Gerhard, P.S. Schulz, P. Wasserscheid, and H.P. Steinrueck. *Surface Studies on the Ionic Liquid 1-Ethyl-3-Methylimidazolium Ethylsulfate Using X-Ray Photoelectron Spectroscopy (Xps)*. in *Zeitschrift Fur Physikalische Chemie-International Journal of Research in Physical Chemistry & Chemical Physics*.
3. Armstrong, J.P., C. Hurst, R.G. Jones, P. Licence, K.R.J. Lovelock, C.J. Satterley, and I.J. Villar-Garcia, *Vapourisation of Ionic Liquids.* Physical Chemistry Chemical Physics, 2007. **9**(8): p. 982-990.
4. Kabo, G.J., A.V. Blokhin, Y.U. Paulechka, A.G. Kabo, M.P. Shymanovich, and J.W. Magee, *Thermodynamic Properties of 1-Butyl-3-Methylimidazolium Hexafluorophosphate in the Condensed State.* Journal of Chemical and Engineering Data, 2004. **49**(3): p. 453-461.
5. Smith, E.F., F.J.M. Rutten, I.J. Villar-Garcia, D. Briggs, and P. Licence, *Ionic Liquids in Vacuo: Analysis of Liquid Surfaces Using Ultra-High-Vacuum Techniques.* Langmuir, 2006. **22**(22): p. 9386-9392.
6. Palacio, M. and B. Bhushan, *A Review of Ionic Liquids for Green Molecular Lubrication in Nanotechnology.* Tribology Letters, 2010.
7. Keppler, A., M. Himmerlich, T. Ikari, M. Marschewski, E. Pachomow, O. Hoefft, W. Maus-Friedrichs, F. Endres, and S. Krischok, *Changes of the near-Surface Chemical Composition of the 1-Ethyl-3-Methylimidazolium Bis(Trifluoromethylsulfonyl)Imide Room Temperature Ionic Liquid under the Influence of Irradiation.* Physical Chemistry Chemical Physics, 2011. **13**(3): p. 1174-1181.
8. Yoshimura, D., T. Yokoyama, T. Nishi, H. Ishii, R. Ozawa, H. Hamaguchi, and K. Seki. *Electronic Structure of Ionic Liquids at the Surface Studied by Uv Photoemission*. in *Journal of Electron Spectroscopy and Related Phenomena*.
9. Smith, E.F., I.J. Villar Garcia, D. Briggs, and P. Licence, *Ionic Liquids in Vacuo; Solution-Phase X-Ray Photoelectron Spectroscopy.* Chemical Communications, 2005: p. 5633-5635.
10. Villar-Garcia, I.J., E.F. Smith, A.W. Taylor, F. Qiu, K.R.J. Lovelock, R.G. Jones, and P. Licence, *Charging of Ionic Liquid Surfaces under X-Ray Irradiation: The Measurement of Absolute Binding Energies by Xps.* Physical Chemistry Chemical Physics, 2011. **13**(7): p. 2797-2808.
11. Lockett, V., R. Sedev, C. Bassell, and J. Ralston, *Angle-Resolved X-Ray Photoelectron Spectroscopy of the Surface of Imidazolium Ionic Liquids.* Physical Chemistry Chemical Physics, 2008. **10**(9): p. 1330-1335.
12. Lockett, V., R. Sedev, S. Harmer, J. Ralston, M. Horne, and T. Rodopoulos, *Orientation and Mutual Location of Ions at the Surface of Ionic Liquids.* Physical Chemistry Chemical Physics, 2010. **12**(41): p. 13816-13827.
13. Palacio, M. and B. Bhushan. *Molecularly Thick Dicationic Ionic Liquid Films for Nanolubrication*. in *Journal of Vacuum Science & Technology A*.

14. Perkin-Elmer, *Phi Handbook of X-Ray Photoelectron Spectroscopy*. 1979.
15. Jablonski, A. and C.J. Powell, *Practical Expressions for the Mean Escape Depth, the Information Depth, and the Effective Attenuation Length in Auger-Electron Spectroscopy and X-Ray Photoelectron Spectroscopy.* Journal of Vacuum Science & Technology A (Vacuum, Surfaces, and Films), 2009. **27**(2): p. 253-61.
16. Shaw, D.J., *Introduction to Colloid and Surface Chemistry*. 1992.
17. Ghatee, M.H. and A.R. Zolghadr, *Surface Tension Measurements of Imidazolium-Based Ionic Liquids at Liquid,Äìvapor Equilibrium.* Fluid Phase Equilibria, 2008.
18. Marsh, K.N., J.A. Boxall, and R. Lichtenthaler. *Room Temperature Ionic Liquids and Their Mixtures - a Review*. in *Fluid Phase Equilibria*.
19. Zhao, W., M.H. Rafailovich, J. Sokolov, and B.B. Sauer, *Wetting Properties of Thin Liquid Polyethylene Propylene Films.* Physical Review Letters, 1993. **70**(10): p. 1453-1456.

APPENDIX II

COMPUTATIONAL AND EXPERIMENTAL CHARACTERIZATION OF A MICROWAVE DISCHARGE-TUBE FURNACE SYSTEM FOR OXIDATION EXPERIMENTS IN DISSOCIATED ENVIRONMENTS

Introduction

Oxidation due to exposure to dissociated species occurs in a wide variety of situations, such as during fabrication of microelectronic devices and during hypersonic flight. Plasma processes have been an integral part of microelectronic fabrication for decades.[1] In these processes plasmas are used to form reactive species, such as atomic fluorine and atomic oxygen, ions, and free electrons from molecular precursors. These species are used to etch or deposit materials at temperatures significantly below those needed if only the molecular species were present. In some cases plasmas enable reactions to occur that would not take place with only the molecular species present. In particular, the use of plasmas to form very thin, good quality silicon dioxide layers has been extensively investigated.[2-4]

Hypersonic speeds are defined as Mach 5 and above. Rockets in the 1940s flew at speeds greater than Mach 5, and space shuttles experience hypersonic speeds during reentry into the atmosphere. The quest to develop a maneuverable vehicle that can fly sustained missions at hypersonic speeds is on-going.[5] Aerodynamic heating dominates the flow physics in the hypersonic regime. Temperatures reached on vehicle surfaces due to aerodynamic heating pose

tremendous challenges for the design of these vehicles. The desire for maneuverability of these hypersonic vehicles requires them to be designed with sharp leading edges. Aerodynamic heating of leading edges increases as the radius of the edge decreases, thereby increasing the temperature of leading edges compared to flat surfaces.[6] The high-energy shock wave formed in front of vehicles flying at these extreme speeds dissociates atmospheric molecular oxygen and nitrogen. These atomic species can exothermically recombine on the vehicle's surfaces, resulting in additional heating of these surfaces.[7] Atomic species can also react with the vehicle's surfaces. These reactions can form surface layers or can remove material from the surface due to formation of volatile species. Any of these changes in the vehicle's surface can affect the surface roughness, emissivity, and other properties of the surface which can change the aerodynamics of the vehicle.

The role of atomic oxygen in interactions with materials during microelectronics fabrication or with surfaces of hypersonic vehicles has not been clearly defined. Plasma processes in microelectronics fabrication involves radicals, molecules, ions and electrons. Studies carried out in plasma reactors, therefore, cannot clearly separate out the role of each of these species. The dissociated atmospheric chemistry and hypersonic flow physics affect the oxidation of surfaces on hypersonic vehicles. Oxidation of materials for hypersonic flight have been investigated using thermal furnaces [8] and arc-jet facilities [9, 10]. The studies carried out in a thermal furnace do not replicate the environment of hypersonic flight due to low dissociation rates of O_2 and N_2, even at elevated temperatures. While they do include flow effects, studies carried out in arc-jet facilities do not replicate the chemistry of hypersonic flight. Arc-jets dissociate the majority of oxygen molecules, far more than what the material would experience in use.

We have developed an experimental system to study oxidation of materials, such as those used in microelectronic device fabrication or those needed for hypersonic vehicles, in dissociated environments. A microwave discharge is used to dissociate a fraction of the gases flowing through it. The oxidation process takes place in a tube furnace downstream of the discharge. The sample sits a significant distance downstream of the discharge to eliminate charged particles from reaching the sample.

The chemistry, pressure, and temperature at the point where the sample is positioned are needed to define oxidation models based on data from experiments performed in this system. In particular, fluxes of different oxidizing species to the sample are required to determine the role of each species in the oxidation process. Values for the parameters of interest cannot easily be measured inside of the furnace where the sample is positioned. Therefore, we have developed a mathematical model to predict the temperature, pressure, and gas flow composition at any point between the microwave discharge and the tube furnace exhaust. The model is based on continuum fluid mechanics of compressible, laminar flow and incorporates five chemical reactions involving the production or consumption of atomic oxygen.

In this report we discuss the development and validation of the model. We also present the laser-based methods used to determine temperatures of the dissociated gas flows, as well as atomic oxygen and ozone concentrations used to characterize the system under various experimental conditions. We demonstrate the capabilities of the model by presenting calculations comparing temperature, pressure, flow rates, and composition profiles along the length of the system. Profiles for rates of the relevant chemical reactions along the length of the system are also presented.

Experimental Methods

A schematic of the experimental system used to study oxidation in dissociated environments is shown in Figure 1. A 6 kW microwave discharge is used to dissociate oxygen in the O_2 (BOC gases, 99.994 %)/ Ar (BOC Gases, 99.999%) stream flowing through it. The gas stream exiting the discharge flows through an approximately 18 cm long section of unheated and uninsulated 2.2 cm diameter quartz tube before entering a tube furnace. The tube furnace has a 5 cm insulated but unheated section followed by a 35 cm long hot zone and another 5 cm insulated but unheated section. Oxidation samples were placed approximately in the middle of the furnace, at least 40 cm downstream of the microwave discharge. A roots blower exhausted the gasses from the system. A capacitance manometer was used in conjunction with a throttle valve between the furnace and the vacuum pump to control the system pressure.

Conditions within the experimental system were characterized under a range of flow conditions (550–2300 sccm gas mixture flow rate, 1 – 10 Torr exit pressure, 300-1323 K furnace temperature) and microwave discharge (1.2 - 6 kW) settings. Pressure, temperature, and gas composition were measured at various points along the system. Pressures at the entrance (Port A) and exit (Port B) of the system were measured using a capacitance manometer connected to the two ports via a manifold. External wall temperatures of the quartz tube were measured using adhesive type K thermocouples. Wall temperatures at several points along the length of the quartz tube were acquired for conditions when the furnace heating was off. When the furnace was heated the external quartz tube wall temperature measurements were restricted to positions outside of the furnace. Thermocouple temperature measurements of non-dissociated gas flows were also performed by inserting a bare 0.003” diameter type K thermocouple into the flow at ports A and B.

Laser-induced fluorescence (LIF) was used for diagnostics of NO molecules, O atoms, and Xe atoms in the flow tube. The need for NO and Xe LIF measurements is explained below. Figure 2 is a sketch of the setup used for these measurements. For these LIF measurements, pulsed ultraviolet (UV) radiation with tunable wavelength near 226 nm was produced by frequency-tripling the visible output from a dye laser, pumped by a Nd:YAG laser, operated at a pulse repetition rate of 10 Hz. A wavelength meter was used to monitor the dye laser wavelength. Several dichroic mirrors directed the UV laser beam through a down-collimating (factor of ~4) Galilean telescope, through a Brewster angle window and down the centerline of the flow tube. The beam energy was continuously monitored by using a quartz slide to reflect a small fraction of the UV beam into an energy meter. Fluorescence was collected at normal incidence to the laser beam through the quartz tube wall by two gated photomultiplier tubes (PMTs). The PMTs were positioned in two rigid mounts, PMT Mount 1 near Port A and PMT Mount 2 near Port B as shown in Figure 2. Band-pass interference filters were placed in front of PMTs to select the fluorescence wavelength of interest. The filters had center wavelengths of 845 nm, 248 nm, and 460 nm for detection of O, NO, and Xe, respectively, and their full-width-at-half-maximum bandwidths were 3 nm for O and 10 nm for NO and Xe.

Thermocouple temperature measurements in dissociated environments are inaccurate due to recombination of O atoms on the thermocouple surfaces. Therefore gas temperatures were determined using the following method[11, 12] when the microwave discharge was on. Nitric oxide spectroscopic thermometry uses nitric oxide laser induce fluorescence (NO-LIF) to determine the rotational temperature of NO molecules in the $\nu = 0$ level of their ground state. It is assumed that this temperature is equal to the translational temperature of NO because the rotational-to-translational energy transfer for this system is rapid. Furthermore, it is assumed that NO is

translationally equilibrated with the bulk gas in the flow tube. For these measurements, pure NO was metered into the gas flow at Port A. The NO was injected into the system through a narrow quartz nozzle facing the gas flow to promote NO mixing with the bulk of the gas. The laser excitation energy was scanned between 44413 and 44421 cm^{-1}, which corresponds to the $A^2\Sigma^+ - X^2\Pi(0-0)$ system of NO. Fluorescence in the 0-1 band of NO near 248 nm was detected by the PMTs fitted with appropriate band-pass filters and positioned on the two PMT mounts. Dividing the detected LIF signal with the measured laser pulse energy normalized the spectra. We extracted temperatures using 11 lines that present either singlets or doublets with the same rotational quantum number *J*. These lines span *J*-values from 8.5 to 26.5 and cover a rotational level energy range of 133.81 cm^{-1}. The rotational temperature was extracted using the Boltzmann formula,

$$\ln\left(\frac{P_i}{2J+1}\right) = \frac{\varepsilon_i}{k_B T} - \ln q \quad , \tag{1}$$

where P_i is the population of level i, $2J + 1$ is the level degeneracy, ε_i is the level energy, q is the rotational partition function, and k_B is the Boltzmann constant. The experimental line intensities were divided by the respective published oscillator strengths to give the relative populations of the respective *J* levels. The rotational temperature was extracted from the slope of a linear fit of $\ln(P_i/2J+1)$ versus ε_i. The uncertainty in NO temperatures determined in this work is about 7%, as determined by the error of the linear fit.

Centerline O-atom concentrations at PMT Mount 1 were determined using a combination of NO titration[13] and two-photon LIF[14, 15]. The two-photon LIF was achieved using excitation at 225.65 nm vacuum wavelength followed by fluorescence at 845 nm [14, 16]. The O-atom fluorescing state $3p^3P_{1,2,0}$ has a radiative lifetime of approximately 35 ns[17]. The most recently

measured values of the room temperature rate constants for quenching of O atoms in this state by O_2 and Ar are approximately 9.4×10^{-16} m^3s^{-1} and 1.4×10^{-16} m^3s^{-1}, respectively[17, 18]. The O-atom LIF signal was then converted to absolute concentrations at PMT Mount 1 by calibrating the detection system using NO titration as described below.

In the NO titration method, N atoms were formed by flowing pure N_2 through the discharge. NO was added downstream of the discharge to form O atoms via the rapid reaction, $N + NO \rightarrow O + N_2$. One O atom is formed for each NO molecule added until the titration endpoint is reached. Thus, the measured O atom LIF signal produced from a known NO flow rate can be assigned to a known O-atom number density. The gas flowing through the discharge was then immediately changed from N_2 to the standard 13% Ar in O_2 mixture used in the oxidation studies. The LIF signal measured under the new conditions was then assigned to the O-atom number density in the O_2/Ar flow after correcting the ratio of O-atom LIF signals in the N_2 and O_2/Ar flows by the ratio of the respective $3p^3P_{1,2,0}$ state quenching factors in the two atmospheres.

The O-atom concentration near Port B can also be determined using O atom LIF if the detection system (PMT + filter) on PMT Mount 2 is calibrated with respect to the detection system on PMT Mount 1. There are a number of sources for differences in the PMT signals at the two locations. The O-atom density is expected to be less at the system exit (PMT Mount 2) than at the system entrance (PMT Mount 1) because of O-atom losses between the two positions due to recombination along the tube wall and due to gas-phase reactions. Also, the two PMTs could have different quantum efficiencies and amplification factors, and the center wavelengths and transmittances of the two optical filters could be slightly different. Imperfect beam collimation would lead to different laser beam sizes at the two positions. Temperature

differences at the two positions would lead to different rate coefficients for quenching of the fluorescing state used in LIF, different number densities of the quenchers O_2 and Ar, and different populations in the $J = 2$ level of the O-atom ground state. Differences in solid angles for fluorescence detection would also result in differences in the PMT signals.

Cross-calibrating the two detection systems can eliminate differences in LIF signals which are not due to O-atom number density differences. We cross calibrated the two detection systems using two-photon LIF from xenon, an approach motivated by the work of Döbele and coworkers[17, 19]. Since the O and Xe two-photon resonances have similar wavelengths, we assumed that the excitation volumes in the two cases are essentially equal. Döbele and coworkers proposed the comparison of the O-atom and Xe LIF signals to determine the absolute O-atom density. However, in our approach the absolute O-atom density is determined at one location via NO titration and Xe LIF was used to determine a *relative* calibration of the detection systems at two locations. This relative calibration was then used to determine the ratio of O-atom densities at the two locations. This approach requires no knowledge of the PMT detection sensitivities and filter transmittances, and is much less sensitive to the uncertainties in the quenching rate coefficients because quenching effects present only a minor correction to the derived O-atom density ratio.

If fluorescence from O atoms and Xe is observed with the same excitation and observation volumes the ratio of the fluorescence signals from the two species can be expressed as[17]

$$\frac{S_O}{S_{Xe}} = \frac{[\mathrm{O}]_0}{[\mathrm{Xe}]_0}\frac{\mathrm{T}_O}{\mathrm{T}_{Xe}}\frac{\eta_O}{\eta_{Xe}}\frac{\sigma_O}{\sigma_{Xe}}\frac{a_O}{a_{Xe}}\left(\frac{h\nu_{Xe}}{h\nu_O}\right)^2 \qquad (2)$$

where S is fluorescence signal integrated over fluorescence wavelength, excitation wavelength, and laser pulse time, and normalized to the square of laser pulse energy; $[\mathrm{O}]_0$ and $[\mathrm{Xe}]_0$ are the number density of ground-state oxygen and xenon atoms, respectively, in the level from which excitation occurs (i.e., $J = 2$ level for O atoms, while the Xe ground state is singlet); T is the transmittance of the filters used for fluorescence detection; η is the quantum efficiency of the particular PMT for the particular fluorescence wavelength; σ is the cross section for the two-photon excitation; ν is the excitation photon frequency; a is the branching ratio for the observed radiative transition (determined by the relative rates of spontaneous emission and collisional quenching of the excited state).

We used a low pumping speed and a low flow rate of pure Xe (~2.5 sccm) so that the Xe pressures at ports A and B were approximately 1.2 Torr. Consequently, the Xe number densities at the two PMT mount locations were essentially equal. If the same PMT/filter combination is used to detect the LIF signal at both mount positions, the ratios of O-atom and Xe energy-normalized LIF signals at each position can be written as

$$\frac{S_O^A}{S_{Xe}^A} = \mathrm{T}_A^2 \frac{[\mathrm{O}]_0^A}{[\mathrm{Xe}]_0} \frac{\mathrm{T}_O}{\mathrm{T}_{Xe}} \frac{\eta_O}{\eta_{Xe}} \frac{\sigma_O}{\sigma_{Xe}} \frac{a_O^A}{a_{Xe}} \left(\frac{h\nu_{Xe}}{h\nu_O} \right)^2 \tag{3}$$

$$\frac{S_O^B}{S_{Xe}^B} = \mathrm{T}_B^2 \frac{[\mathrm{O}]_0^B}{[\mathrm{Xe}]_0} \frac{\mathrm{T}_O}{\mathrm{T}_{Xe}} \frac{\eta_O}{\eta_{Xe}} \frac{\sigma_O}{\sigma_{Xe}} \frac{a_O^B}{a_{Xe}} \left(\frac{h\nu_{Xe}}{h\nu_O} \right)^2 \tag{4}$$

LIF signals at each position must be collected by each detection system for this calibration procedure. The superscripts A and B in this section denote quantities measured with a specific detector system positioned on PMT Mount 1 and PMT Mount 2, respectively. Equations (3) and (4) contain additional factors T^A and T^B, which represent transmittances at the

excitation beam wavelength in the gas column between the front Brewster window and the respective PMT location. These transmittances depend on the amount of ozone present in the flow tube. The method used to measure these transmittances is described later in this section. Combining (3) and (4) yields the ratio of O-atom densities measured by one PMT/filter combination at the two mount positions

$$\frac{[\mathrm{O}]_0^A}{[\mathrm{O}]_0^B} = \frac{S_O^A}{S_O^B}\frac{S_{Xe}^B}{S_{Xe}^A}\frac{a_O^B}{a_O^A}\left(\frac{\mathrm{T}^B}{\mathrm{T}^A}\right)^2 \tag{5}$$

The number density of O atoms in the $J = 2$ level of the O-atom ground state can be expressed via the Boltzmann distribution as

$$[\mathrm{O}]_0 = [\mathrm{O}]\times\frac{5}{5+3\exp\left(-\frac{227.4\mathrm{K}}{T}\right)+\exp\left(\frac{326.1\mathrm{K}}{T}\right)} \equiv [\mathrm{O}]\times\Delta_{J=2}(T), \tag{6}$$

where [O] is the total O-atom density and the numbers in the exponent are energies of the $J = 1$ and $J = 0$ levels expressed as equivalent temperatures.

The branching ratio for radiative decay, a_O, is given by

$$a_O = \frac{\tau_O^{-1}}{\tau_O^{-1}+\sum_q k_{q,O}[q]}, \tag{7}$$

where τ_O is the radiative lifetime of the O-atom excited state, [q] is the number density of the collision partner q that quenches the excited state, and $k_{q,\mathrm{O}}$ is the rate coefficient for quenching of the excited state by the species q. In our experiments with O_2/Ar mixtures, the only relevant quenchers of the excited state are O_2 and Ar. Both $k_{q,\mathrm{O}}$ and [q] are temperature-dependent. It is usually assumed that the cross section for quenching of the O-atom excited state, σ_q, has weak temperature dependence. Since $k_{q,O} = \sigma_{q,O} < v >$, where $< v >$ is mean collision velocity, the

temperature dependence of $k_{q,\mathrm{O}}$ is proportional to $\sqrt{\mathrm{T}}$. The collision partner densities are related to the gas temperature and partial pressures, p_q, via the ideal gas law. The partial pressures can be related to the total pressure, p, as $p_q = pf_q/f$, where f_q is the molar flow rate of the species q and f is the total molar flow rate of the mixture. Thus, combining expressions (5) through (7) we finally obtain

$$\frac{[\mathrm{O}]^A}{[\mathrm{O}]^B} = \frac{S_O^A}{S_O^B}\frac{S_{Xe}^B}{S_{Xe}^A}\left(\frac{\mathrm{T}^B}{\mathrm{T}^A}\right)^2 \frac{\Delta_{J=2}(T_B)}{\Delta_{J=2}(T_A)} \frac{\tau^{-1} + \dfrac{p^A}{k_B f\sqrt{298\mathrm{K}}\sqrt{T_A}}\displaystyle\sum_q f_q k_{q,\mathrm{O}}^{298}}{\tau^{-1} + \dfrac{p^B}{k_B f\sqrt{298\mathrm{K}}\sqrt{T_B}}\displaystyle\sum_q f_q k_{q,\mathrm{O}}^{298}} \tag{8}$$

In expression (8) all quantities with the exceptions of the room-temperature rate quenching coefficients, $k_{q,\mathrm{O}}^{298}$ and the excited state radiative lifetime were directly measured in the experiment.

For the calibration to be valid, both the O-atom and Xe LIF signals must have a quadratic dependence on the excitation energy, as is expected for a two-photon process. At high excitation energies several saturation effects can lead to deviations from the quadratic dependence. Therefore, the laser excitation energy was kept in the range where quadratic signal dependence has been verified.

The calibration procedure starts by measuring the LIF signal from Xe near Port A, S_{Xe}^A, by a detector system mounted on PMT Mount 1, and then moving that detection system to PMT mount 2 near Port B to measure S_{Xe}^B. Simultaneously, Xe LIF measurements were performed with a second detection system, first positioned on PMT Mount 2 near Port B, then positioned on PMT Mount 1 near Port A. Subsequently, each detection system was returned to its starting position to check reproducibility of the measurements. The energy-normalized LIF signals

collected after returning the detection systems to their starting positions were reproduced within the noise level of the measurement, confirming that the observation geometry was maintained throughout the procedure. After this, the identical procedure was performed with flowing an 13% Ar in oxygen mixture, under standard flow conditions and discharge power, to determine S_O^A and S_O^B for both detection systems. With temperatures T_A and T_B and transmittances T^A and T^B known from independent measurements, the O atom density ratio $[O]^A/[O]^B$ was calculated. The use of two detection systems provided a redundant measurement of this ratio, which was used as a consistency check.

In addition to the $[O]^A/[O]^B$ ratio, the above described measurements determine the ratio of the detection efficiencies at the O-atom detection wavelength of the two detection systems. In other words, these measurements cross-calibrate the two detection systems. The detection efficiency ratio, $\phi_{1/2}$, is given by

$$\phi_{1/2} \equiv \frac{\Delta\Omega^A(1)}{\Delta\Omega^A(2)} \frac{T_O(1)}{T_O(2)} \frac{\eta_O(1)}{\eta_O(2)} = \frac{S_O^A(1)}{S_O^A(2)} \tag{9}$$

where numbers in the parentheses refer to detection system 1 or 2, and $\Delta\Omega^A$ is the solid angle for LIF detection, which may be different for the two detectors, primarily due to small differences in the their alignments within their housings. Analogous expressions can be written for detectors on PMT Mount 2 near Port B. The extracted values of $\phi_{1/2}^A$ and $\phi_{1/2}^B$ are nearly equal, indicating the measurements at each position are consistent.

Oxygen atoms produced in the microwave discharge recombine with molecular oxygen to form ozone via the three-body process $O + O_2 + M \rightarrow O_3 + M$, with a room-temperature rate coefficient, $k_{298\,K}$, of about 6×10^{-34} $cm^6 s^{-1}$.[20] Presence of a significant amount of ozone in the flow tube has two unwanted effects: further removal of O-atoms via the process

$O + O_3 \rightarrow O_2 + O_2$ ($k_{298\,K} = 8 \times 10^{-15}$ $cm^3 s^{-1}$),[20] and attenuation of the UV laser beam in the flow tube. The same laser system used for the LIF studies was used to measure room temperature UV absorption near 226 nm to investigate ozone formation downstream of the microwave discharge. The absorption cross-section of ozone at this wavelength, σ_{O_3}, is approximately 3.2×10^{-18} cm^2, while the corresponding absorption cross-section of O_2 is six orders of magnitude lower.[20] Absorption by O atoms was avoided by tuning the wavelength slightly off the O-atom two-photon resonance. During the absorption measurement a small quartz slide (4×5 mm) attached to a 3-mm diameter quartz rod was mounted inside the flow tube at Port A or Port B. The slide was used to deflect a portion of the beam by approximately 90° through the quartz tube wall into a laser energy meter. The total absorption path length between the Brewster angle window and the quartz slide was 125 cm.

Ozone formation at room temperature was not detected for total pressures up to 3 Torr. Increasing O_2 partial pressure should increase the rate of ozone formation. Measurements showed that ozone formation became significant above 6 Torr total pressure. At a total pressure of 9.3 Torr, the presence of ozone absorption decreased the transmittance of the gas in the tube to about 0.8, corresponding to an ozone partial pressure of approximately 18 mTorr. We did not observe a relationship between ozone concentration and gas velocity under the conditions investigated.

Numerical Model

The experimental system between Port A and Port B was modeled as axisymmetric, enabling the use of a 1.1 cm high by 76 cm long rectangular model system (see Figure 1). In all

cases the Reynolds number was no greater than 308 and the Knudsen number was no greater than 5.4×10^{-3}. Therefore all investigated flow conditions were laminar and continuous.

Momentum balances in the axial (z) and radial (r) directions, the continuity equation, an energy balance, and three mass balances (O, Ar, and O_3) describe the environment in the reactor system. The partial differential equations (PDEs) of the model are listed in Table 1. A key to the model variables is provided at the end of this manuscript. The model calculates axial and radial velocities, temperature, pressure, and the concentrations of O, O_2, O_3 and Ar throughout the system.

The model was solved using COMSOL MULTIPHYSICS®, a finite element method (FEM) solver. The FEM numerically solves the partial differential equations on a mesh which defines the system geometry[21]. COMSOL employs the Galerkin's weighted residual method to solve the PDEs at each element.[22] Our model was solved on a structured mesh of rectangular elements. All mesh elements were 0.1375 cm high in the radial direction with axial lengths depending on the position of the element in the system. Element sizes were set at the point where reducing their size no longer affected the calculated solution.

The gas entering the microwave discharge consisted of 87 mole % O_2 and 13 mole % Ar. Furthermore, measurements of O-atom concentration at various microwave discharge powers, plotted in Figure 3, indicate that no more than 5% of the O_2 molecules were dissociated under the conditions investigated. Therefore, O_2 was defined as a carrier gas and diffusivities for all species were calculated for diffusion through O_2. Standard physical properties of oxygen, argon, and ozone were used.[23-25] The relationship for the diffusion coefficient of O in O_2 as a function of temperature presented by Pallix and coworkers[26] was used.

Table 2 contains the boundary conditions employed to solve the PDE's. The centerline condition is a consequence of axial symmetry. A no-slip, impenetrable boundary condition was used at the reactor wall (r=1.1 cm). The Biot number is approximately 0.024 for the quartz tube used, supporting the assumption that at any point in the system the inside quartz wall temperature is equal to the outside quartz wall temperature. The temperature of the gas adjacent to the inside wall was assumed to be equal to the wall temperature at that point. Temperatures measured along the outside length of the quartz tube define a boundary condition of the energy balance. When simulating the furnace-on conditions, a linear temperature profile was assumed for the quartz wall temperatures in the 5 cm long insulated but not heated sections at the entrance and exit of the furnace. The pressure at Port B was set to the measured outlet pressure and neither energy nor mass was allowed to diffuse through the outlet boundary

Direct recombination of O atoms and O-atom recombination through the ozone mechanism describe the homogeneous chemistry of the plasma afterglow. O-atom recombination at the wall is taken into account through a reactive boundary condition for the mass balance. The reactions and the reaction rate constants used in our model are presented in Table 3. The subscript on the three-body reaction rate constants in Table 3 denotes the species acting as the third body (M) for these constants. The expression for the rate constant of reaction 2 has an X in the exponential term for temperatures between 400 and 700 K. Note that X changes with temperature. Rate constants for temperatures between 400 and 700 K have not been previously reported. The values for X noted in Table 3 for $K2_{Ar}$ between 400 K and 700 K come from an interpolation to provide a smooth transition between the two reported temperature ranges.

The efficiency of a species (M) to catalyze a three-body reaction can differ for different species. For reaction 1 the reaction rate constant reported in Table 3 was used for M=Ar, O_2, O, or O_3 as no high temperature reaction rate constants as a function of third body have been reported for this reaction. Reaction rate constants for reaction 1 as a function M has been recently measured near room temperature.[27, 28] The rate constants used in this work are approximately a factor of 2 higher than those measured at these low temperatures. However, the region where these low temperatures are applicable in our system is small. Therefore, any errors introduced into our calculations by using the higher values should be negligible. Lin and Leu found that reaction rate constant for M=O_2 was roughly 1.5 times that of M= Ar for reaction 2.[29] No reports were found comparing reaction rate constants for M= O or O_3 in reaction 2, so we used the same reaction rate constants for M=O, O_2 and O_3 in reaction 2. Solving the model using K2 for M=O_2, O, or O_3 equal to 1.5 times $K2_{Ar}$ resulted in the calculated O_3 concentrations more than 10% greater than experimental measurements. Increasing K2 rate constants for M=O_2, O, or O_3 to 2.0 times $K2_{Ar}$ resulted in calculated O_3 concentrations agreeing with experimental measurements to within 4%. Therefore K2 for M= O, O_2, or O_3 was set at 2.0 time $K2_{Ar}$. For reaction 4, the rate constant for M=O_3 was reported to be four times the rate constant for M=Ar[30] and 2 times more than that of M= O_2 [31]. The rate constant for M= O for reaction 4 has not been reported. The rate constant for M=O was assumed to be the same as that for M=O_2 for reaction 4.

The rate coefficient for heterogeneous O-atom recombination, K5, is a function of the reactor inner diameter, d, the fraction of O-atoms striking the wall that recombine to form O_2, γ, and the thermal velocity of O atoms, V_t as given by equation (10).

$$V_t = \sqrt{\frac{8RT}{\pi MW}} \tag{10}$$

Gamma has been measured using arc-jet furnace, microwave discharge, and shock tube experiments[32]. The reported value for γ determined using a microwave discharge has an estimated error of 100% at 300 K and the error increases with temperature [15]. Because of the large discrepancies between reported values of γ at elevated temperatures[15, 26, 32-37], we extracted values for γ based on agreement of our model with experimental measurements of temperature and O-atom concentration.

Experimental data collected with various microwave discharge powers and furnace temperatures were used to determine γ(T) for our system. An iterative process was followed, solving the complete model using different values of γ until temperatures, pressures, and compositions matched experimental measurements. The initial estimate for γ was based on reported values [32-34] and was updated with each iteration. For every iteration of γ, iterations for temperature and composition were also needed. The entrance pressure was measured at Port A, 7.5 cm upstream of PMT Mount 1 where the temperature was measured. The solution procedure started by solving the model using various values for the temperature at Port A until the calculated centerline temperature at PMT Mount 1 agreed with experimental measurements. A parabolic centerline to wall gas temperature profile was used for all calculations, though the solution of the model was insensitive to the profile assumed. O-atom concentrations were measured at PMT Mount 1 and 2. Therefore the O-atom concentration at Port A also needed to be estimated and the model solved until calculations agreed with experimental measurements. The model was iterated with estimated entrance temperatures and O atom mole fractions until the calculated centerline temperature and O atom concentration at PMT Mount 1 agreed with

measurements. Once good agreement was obtained for entrance characteristics, the ratio of O-atom concentration at the PMT Mount 2 to that at PMT Mount 1 was used to evaluate if the value used for γ was correct. If the calculated and measured O-atom concentration ratios did not agree to within 10% γ was updated and the solution cycle was repeated. The furnace-off case was used to estimate γ for temperatures between 300 and 373 K. Furnace-on conditions were used to estimate γ for temperatures at 400 K and above.

Figure 4 plots measured and calculated ratios of O-atom concentration at PMT Mount 2 to that at PMT Mount 1 versus furnace temperature. Figure 5 plots the extracted γ values versus temperature. Due to a lack of experimental measurements, γ values were kept constant for temperatures 900 K and above. Table 4 compares the extracted γ values from this study to those previously reported. Our values are consistent with those reported by others. We used a spline interpolation between the extracted values to define $\gamma(T)$, which was used in the reactor model.

Results and Discussion

The flow components of the model were validated by comparing calculated pressures to those measured under constant temperature (300 K), gas flow rates between 550 and 2300 sccm, with both the discharge and furnace off. The measured entrance pressure for each condition was used to initiate the calculation and was updated after every iteration. The resulting calculated inlet pressure was within 0.1% of the experimental measurement. The calculated inlet pressure was also within 0.1% of the experimental value for similar gas flows through the system with the furnace set at 1323 K. These results confirm that the flow equations and chosen parameters accurately model the flow physics of our system.

Agreement with measured gas compositions was used to determine entrance temperature, entering O-atom mole fraction, and $\gamma(T)$. Solutions of the model which included the chemistry components for the cases 2300 sccm of gas flow with the furnace off and the furnace on agreed with the measured pressure to within 1.7% and 4.5%, respectively.

The remaining results and discussion focuses on calculations performed for conditions of 2300 sccm gas flow rate, pressure at the throttle valve of 298 Pa (furnace-off) and 427 Pa (furnace-on, set point= 1323 K), and 80% of the maximum microwave discharge power. These conditions are representative of those used in our oxidation studies. Figure 6 contains plots of calculated pressure and centerline temperatures along the length of the system. The position of Ports A and B, PMT Mount 1 (PMT 1) and PMT Mount 2 (PMT 2), and the furnace are notated by vertical dashed lines on each of the plots to aid the interpretation of the data. Figure 6a contains calculated pressure profiles. Note that the pressure at Port B is approximately 1.5 times higher for the furnace-on case than for the furnace-off case. The pressure at Port B is an input into the model and reflects the difference in pressure observed in these two cases. Figure 6b contains profiles of the calculated centerline temperature. The temperature profile before the furnace is not affected by the state of the furnace. Note that the centerline temperature of the gas entering the system is nearly 800 K due to heating by the microwave discharge.

The model calculates both the radial and axial gas velocities throughout the system. Due to the boundary conditions used the radial velocity will be zero at the centerline and at the wall. Therefore Figure 7 plots the radial and axial velocity profiles at a radius of 0.006 m to facilitate comparison of velocities in the two directions. The radial velocity for the furnace-off condition is nominally zero throughout the system. However, for the furnace-on condition the radial velocity significantly deviates from zero in the unheated 5-cm long sections at the entrance and

exit of the furnace. The temperature of the wall is input into the model and used as a boundary condition. The wall temperature profile in these unheated sections cannot be measured. We assumed the temperature increased linearly from the last measured temperature, 342 K, to the furnace set point, 1323 K, in unheated section at the entrance of the furnace. Likewise we assumed the temperature decreased linearly from 1323 K to the first measured temperature, 380 K, in the unheated section at the exit of the furnace. These large temperature gradients (approximately 190 K/cm) are driving these radial flows. The magnitude of the radial velocities, however, are between a factor of 25 and 150 less than the axial velocities in the system. Figure 8 contains plots of the velocity profiles in the radial direction. Each plot contains profiles at the system entrance (z=0 m), the furnace entrance (z=0.2 m), midway through the furnace (z=0.4 m), and the system exit (z=0.76 m). The axial velocity profiles are all parabolic with their maxima at the centerline, regardless of the point in the system or the state of the furnace. The radial velocity profiles for furnace-off condition are flat at the system exit and entrance but are parabolic inside the furnace. The radial flow inside the furnace is negative, indicating it is flowing toward the center of the tube. The radial velocity profile at the system entrance is flat for the furnace-on condition. With the furnace on the radial velocity profile is parabolic and negative at furnace entrance and exit, and is parabolic and positive midway through the furnace.

Figure 9 plots the calculated centerline O-atom, O_3, O_2, and Ar concentration profiles for the same flow conditions used in Figures 6-8. The O-atom concentrations at the entrance to the system for the furnace-on and furnace-off conditions are similar. However, the O-atom concentration drops by more than an order of magnitude within the 1323 K furnace. The O-atom concentration only drops by a factor of approximately 5 for the furnace-off condition.

While absolute concentrations drive the rates of the reactions occurring in the system, mole fractions of the components simplifies comparison of gas compositions in systems where both temperature and pressure are not constant. Calculations show that the mole fractions of O_2 and Ar are fairly constant through the system. For the furnace-off condition the mole fraction of oxygen throughout the system was 0.82 ± 0.02 and the mole fraction of argon throughout the system was 0.14 ± 0.007. For the furnace-on conditions the mole fractions for oxygen and argon throughout the system were 0.85 ± 0.03 and 0.14 ± 0.02, respectively. Figure 10 contains plots of the mole fraction profiles of O atoms and ozone for the furnace-off and furnace-on conditions. Note that the O-atom mole fraction is an order of magnitude higher than that of ozone and it decreases from system entrance to exit irrespective of the furnace condition. However, the ozone mole fraction increases from the system entrance to exit when the furnace is off but decreases inside the furnace when the furnace is on.

Figure 11 contains plots showing the calculated rates (change in O-atom number density per time) for the five reactions listed in Table 3. In these plots all the three-body reaction rates are the sum of the rates for all third body species. The rate of each O-atom recombination reaction for the furnace-off condition varies by less than an order of magnitude between the entrance and exit of the furnace. However, when the furnace is off the rate of O-atom generation from the decomposition of ozone drops approximately three orders of magnitude from the entrance to the exit of the furnace. This decrease in the rate of ozone decomposition along the length of the unheated furnace is consistent with the increase in ozone concentration shown in Figure 9. The rate of each O-atom recombination reaction decreases across the system when the furnace is on, but the extent of the decrease depends on the reaction. The rate of recombination at the wall only decreases about one order of magnitude across the system, while the rates of

direct homogeneous recombination and recombination with ozone both decrease over three orders of magnitude across the system. The rate of O-atom generation due to ozone degradation decreases to the entrance of the furnace but then increases inside the hot furnace.

Summary and Conclusion

Values for the parameters of interest to building a model for material oxidation in dissociated environments cannot easily be measured at the sample's position in the experimental system. Therefore, we have developed a mathematical model to predict the gas composition, temperature, and pressure for an argon/oxygen mixture flowing out of a microwave plasma discharge through a downstream tube furnace. The model was based on continuum fluid mechanics of compressible, laminar flow and incorporated five chemical reactions involving the production or consumption of atomic oxygen. Laser-based methods were used to measure temperatures of dissociated flows as well as oxygen atom and ozone concentrations under a variety of process conditions. Experimentally measured oxygen atom concentrations were used to extract ©, the oxygen-atom heterogeneous recombination probability, at several temperatures. The extracted © values were consistent with those previously reported. All other reaction rate constants and physical properties used in the model were based on literature values or calculated by accepted methods.

Temperature, pressure and gas composition profiles calculated by the model are consistent with experimental observations and agree with measured values to within approximately 10%. The excellent agreement to measured data suggests the model is a good representation of the experimental system and can be used to estimate the conditions at any point

within the system. Pressures, temperatures, and gas compositions predicted by this reactor scale model will be used to develop an oxidation model for samples processed in this system.

Acknowledgements

The authors gratefully acknowledge the National Science Foundation for support of this work under grants number DMR 0435843, and DMR0435856.

Variable Key

r, r-direction; radial direction from reactor centerline to wall, m
z, z-direction; axial direction down reactor, m
v_i, velocity component, m s^{-1}
v_{mean}, mean velocity at the entrance, m s^{-1}
T, temperature, K
T_{in}, temperature set in program for the entrance temperature linear correlation, K
μ, viscosity, $Pa \cdot s$
p, pressure, Pa
ρ, density, kg m^{-3}
g, acceleration due to gravity, m s^{-2}
N_{iz}, z-direction flux component, mol $m^{-2}s^{-1}$
N_{ir}, r-direction flux component, mol $m^{-2}s^{-1}$
H_i, enthalpy of component i, J mol^{-1}
k, thermal conductivity, W $m^{-2}K^{-1}$
C_{pi}, heat capacity of component i, J $mol^{-1}K^{-1}$
c, total concentration, mol m^{-3}
c_i, concentration of component i, mol m^{-3}
c_{io}, initial concentration of component i, mol m^{-3}
D_i, diffusivity of component i through O_2, m^2s^{-1}
R_i, reaction rate expression for component i, mol $m^{-3}s^{-1}$
$K1_M$, Direct recombination reaction rate constant involving third body M, cm^6 $molecule^{-2}$ s^{-1}
$K2_M$, Ozone mechanism step 1 recombination rate constant involving third body M, cm^6 $molecule^{-2}$ s^{-1}
K3, Ozone mechanism step 2 rate constant, cm^3 $molecule^{-1}$ s^{-1}
$K4_M$, Ozone mechanism step 3 rate constant involving third body M, cm^6 $molecule^{-2}$ s^{-1}
K5, O-atom wall recombination rate, s^{-1}
γ, fraction of O-atoms striking the wall which recombine
V_t, thermal velocity of O-atoms, ms^{-1}
d, internal diameter of reactor, m
R, universal gas constant, m^3Pa $mol^{-1}K^{-1}$
MW, molecular weight, g mol^{-1}

Figure Captions

Figure 1. Schematic of experimental system used to study oxidation of materials in dissociated environments.

Figure 2. Sketch of experimental system including the components used for the laser induced fluorescence measurements.

Figure 3. Percent of molecular oxygen dissociated versus power setting on the microwave discharge.

Figure 4. Plot of the ratio of the concentration of atomic oxygen measured at the entrance to the that measured at the exit of the system as a function of temperature of the furnace. Open symbols with error bars indicate measurements. Filled symbols indicate model calculated values.

Figure 5. Plot of fraction of oxygen atoms striking the furnace wall that recombine as a function of temperature. These values were extracted by fitting the model to experimental measurements.

Figure 6. Calculated pressure and centerline temperature profiles along the length of the system. Conditions used were 2300 sccm gas flow rate, pressure at the throttle valve of 298 Pa (furnace-off) and 427 Pa (furnace-on, set point= 1323 K), and 80% of the maximum microwave discharge power. Open symbols indicate furnace-off conditions. Filled symbols indicated furnace-on conditions.

Figure 7. Radial and axial velocity profiles calculated at a radius midway between the centerline and the furnace wall. Conditions used were 2300 sccm gas flow rate, pressure at the throttle valve of 298 Pa (furnace-off) and 427 Pa (furnace-on, set point= 1323 K), and 80% of the maximum microwave discharge power. Open symbols indicate furnace-off conditions. Filled symbols indicated furnace-on conditions.

Figure 8. Radial velocity (left) and axial velocity (right) radial profiles calculated at z= 0, 0.2, 0.4, and 0.76 meters. Conditions used were 2300 sccm gas flow rate, pressure at the throttle valve of 298 Pa (furnace-off) and 427 Pa (furnace-on, set point= 1323 K), and 80% of the maximum microwave discharge power. Open symbols indicate furnace-off conditions. Filled symbols indicated furnace-on conditions.

Figure 9. Calculated centerline O-atom, O_3, O_2, and argon concentration profiles. Conditions used were 2300 sccm gas flow rate, pressure at the throttle valve of 298 Pa (furnace-off) and 427 Pa (furnace-on, set point= 1323 K), and 80% of the maximum microwave discharge power. Open symbols indicate furnace-off conditions. Filled symbols indicated furnace-on conditions.

Figure 10. Calculated mole fraction profiles for O-atoms and O_3. Conditions used were 2300 sccm gas flow rate, pressure at the throttle valve of 298 Pa (furnace-off) and 427 Pa (furnace-on, set point= 1323 K), and 80% of the maximum microwave discharge power. Open symbols indicate furnace-off conditions. Filled symbols indicated furnace-on conditions.

Figure 11. Calculated reaction rate profiles for the five reactions included in the model. Conditions used were 2300 sccm gas flow rate, pressure at the throttle valve of 298 Pa (furnace-off) and 427 Pa (furnace-on, set point= 1323 K), and 80% of the maximum microwave discharge power. Open symbols indicate furnace-off conditions. Filled symbols indicated furnace-on conditions.

Table 1. The partial differential equations used to describe conditions inside the reactor system.

Momentum Balance
r-component
$$-\frac{4}{3}\mu\frac{\partial^2 v_r}{\partial r^2}-\mu\frac{\partial^2 v_r}{\partial z^2}=\frac{\partial p}{\partial r}+\frac{dv_r}{\partial r}\left[\frac{2\mu}{3r}-\rho v_r\right]-\frac{\partial v_z}{\partial z}\left[\frac{2\mu}{3r}\right]+\frac{\partial^2 v_z}{\partial z\partial r}\left[\frac{\mu}{3}\right]+\rho g_r-\rho v_z\frac{\partial v_r}{\partial z}$$
z-component
$$-\frac{4}{3}\mu\frac{\partial^2 v_z}{\partial z^2}-\mu\frac{\partial^2 v_z}{\partial r^2}=\frac{\partial p}{\partial z}+\frac{dv_z}{\partial r}\left[\frac{\mu}{r}-\rho v_r\right]-\frac{\partial v_r}{\partial z}\left[\frac{\mu}{3r}\right]+\frac{\partial^2 v_r}{\partial z\partial r}\left[\frac{\mu}{3}\right]-\rho v_z\frac{\partial v_z}{\partial z}$$
Continuity Equation
$$c\left[\frac{\partial v_r}{\partial r}+\frac{v_r}{r}+\frac{\partial v_z}{\partial z}\right]+v_r\frac{\partial c}{\partial r}+v_z\frac{\partial c}{\partial z}=Ro+Ro_2+Ro_3$$
Energy Balance
$$k\left[\frac{\partial^2 T}{\partial z^2}+\frac{\partial^2 T}{\partial r^2}\right]=\sum_{i=1}^{3}\left[\frac{\partial\left(N_{ir}H_i\right)}{\partial r}+\frac{\partial\left(N_{iz}H_i\right)}{\partial z}+\frac{N_{ir}H_i}{r}\right]-v_z\frac{\partial p}{\partial z}-v_r\frac{\partial p}{\partial r}$$ $$+\mu\left[2\left[\left(\frac{\partial v_z}{\partial z}\right)^2+\left(\frac{\partial v_r}{\partial r}\right)^2\right]+\left[\frac{\partial v_z}{\partial r}+\frac{\partial v_r}{\partial z}\right]^2-\frac{2}{3}\left[\frac{\partial v_z}{\partial z}+\frac{\partial v_r}{\partial r}\right]^2\right]$$
Component Mass Balance
$$c\left[\frac{\partial v_r}{\partial r}+\frac{v_r}{r}+\frac{\partial v_z}{\partial z}\right]+v_r\frac{\partial c_i}{\partial r}+v_z\frac{\partial c_i}{\partial z}=D_i\left[\frac{\partial^2 c_i}{\partial r^2}+\frac{1}{r}\frac{\partial c_i}{\partial r}+\frac{\partial^2 c_i}{\partial z^2}\right]$$

Table 2. The boundary conditions used to solve the model PDEs

Equation	Entrance	Centerline	Wall	Outlet
Momentum Balance	$v = 2v_{mean}\left(1-\left(\frac{r}{R}\right)^2\right)$ $v_r = 0$	$\frac{dv}{dr} = 0$	$v = 0$	$p = p_{outlet}$
Energy Balance	$T = T_{in}(r)$	$\frac{dT}{dr} = 0$	$T = T_{wall}$	Diffusive flux=0
Mass Balance	$c_i = c_{io}(T)$	$\frac{dc}{dr} = 0$	$\frac{dc_{O_3}}{dr} = \frac{dc_{Ar}}{dr} = 0$ $\frac{dc_O}{dr} = \frac{\gamma V_t c_o}{4}$	Diffusive Flux=0 for each species

Table 3

Reaction	Rate Constant	Uncertainty	Source
	Direct Recombination		
1. $O+O+M \rightarrow O_2+M$	$K1_{Ar} = 5.2x10^{-35} e^{\left(\frac{900}{T}\right)}$ $K1_{Ar} = K1_O = K1_{O_2} = K1_{O_3}$	20% at 300 K, 60% at higher temperatures	[38]
	Ozone Mechanism		
2. $O+O_2+M \rightarrow O_3+M$	$K2_{Ar} = 4.5x10^{-34} e^{\left(\frac{T}{300}\right)^{-2.7}}$ $200 \le \mathrm{T} < 400$ K $K2_{Ar} = 4x10^{-35} e^{\left(\frac{T}{1000}\right)^{X}}$ $X = -1.8$ for 400<T < 500 K X= -1.7 for $500 \le \mathrm{T} < 600$ K X= -1.4 for $600 \le \mathrm{T} < 700$ K X= -1.0 for $700 \le \mathrm{T} < 2000$ K $K2_O = K2_{O_2} = K2_{O_3} = 2 \times K2_{Ar}$	15% at 400 K	[39]
3. $O+O_3 \rightarrow 2O_2$	$K3 = 8x10^{-12} e^{\left(\frac{-2060}{T}\right)}$	15% at 300 K	[20, 40]
4. $O_3+M \rightarrow O_2+O+M$	$K4_{Ar} = 7.16x10^{-10} e^{\left(\frac{-11180}{T}\right)}$ $K4_O = K4_{O_2} = 2 \times K4_{Ar}$ $K4_{O_3} = 4 \times K4_{Ar}$	100% at 1000 K	[30, 31]
	Surface Reaction		
5. $O+O_{Surface} \rightarrow O_2$	$K5 = \frac{\gamma V_t}{d}$	100% at 300 K, Increases with temperature	See Table 4

Table 4.

$\gamma \times 10^4$	Temperature (K)	P (Pa)	Reference
4.75-8.9	300-1450	290-600	This Study
2.5	400-900	40	Marschall[15]
0.6-1.3	300	27-93	Pallix[26]
5-11	194-1260	27	Kim[35]
1.8-140	293-873	1.5×10^{-3}	Greaves[34]
0.27-0.78	293	533	Berkowitz[33]
0.4	300	150	Hacker[36]
3.2	300	133	Krongelb[37]

Figure 1

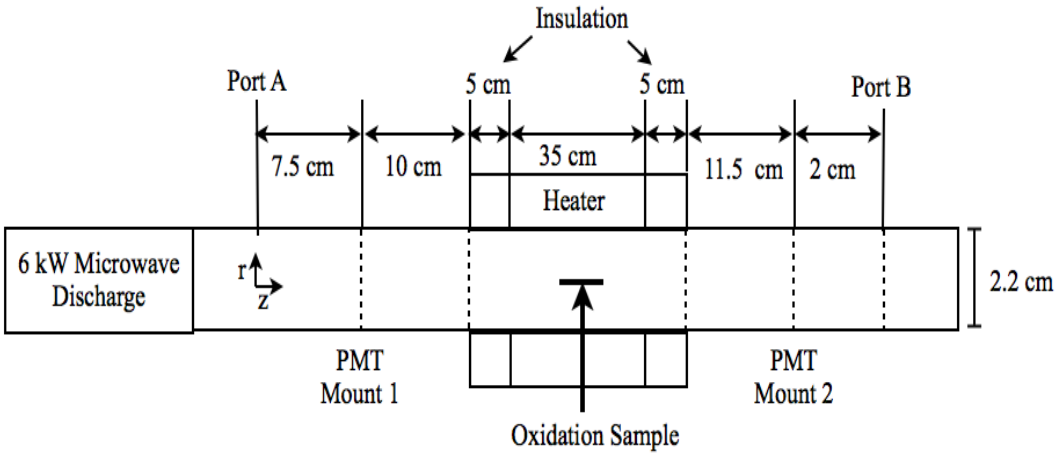
Insulation
Port A
5 cm
5 cm
Port B
7.5 cm
10 cm
35 cm
Heater
11.5 cm
2 cm
6 kW Microwave Discharge
r
z
2.2 cm
PMT Mount 1
PMT Mount 2
Oxidation Sample

Figure 2

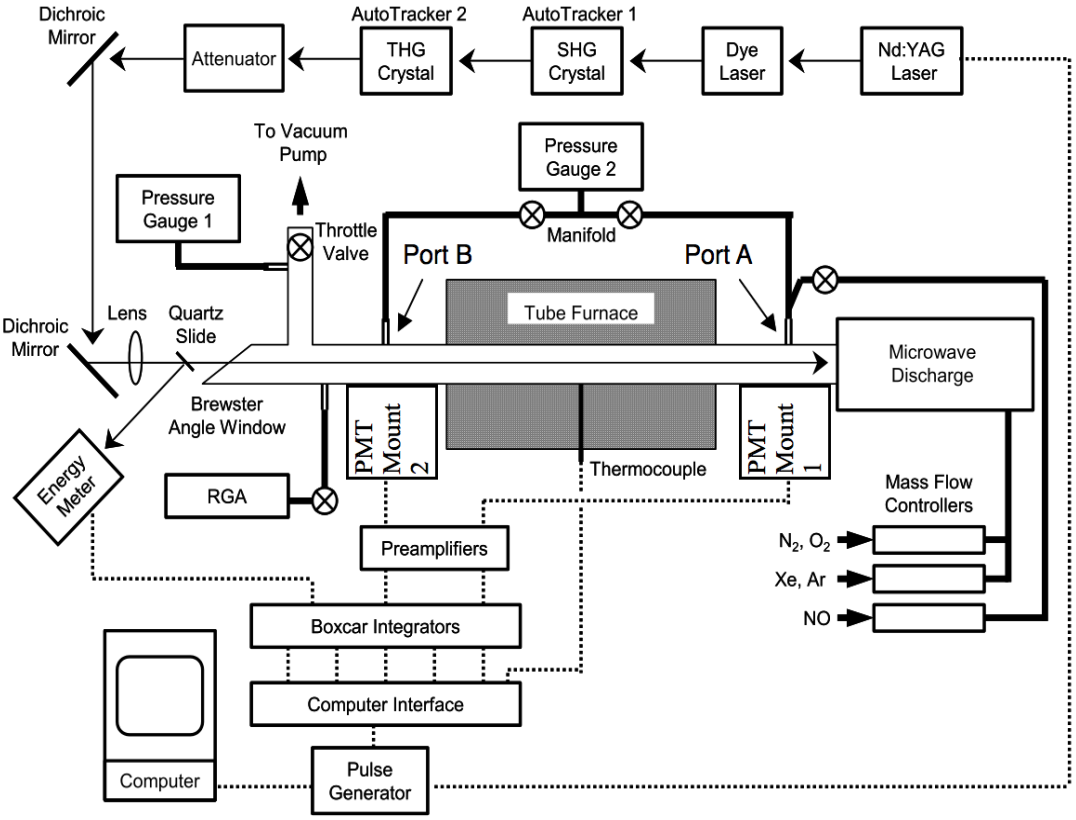
Dichroic Mirror
Attenuator
AutoTracker 2
THG Crystal
AutoTracker 1
SHG Crystal
Dye Laser
Nd:YAG Laser
To Vacuum Pump
Pressure Gauge 2
Pressure Gauge 1
Throttle Valve
Manifold
Port B
Port A
Tube Furnace
Dichroic Mirror
Lens
Quartz Slide
Microwave Discharge
Brewster Angle Window
PMT Mount 2
PMT Mount 1
Energy Meter
RGA
Thermocouple
Mass Flow Controllers
Preamplifiers
N_2, O_2
Xe, Ar
NO
Boxcar Integrators
Computer Interface
Computer
Pulse Generator

Figure 3

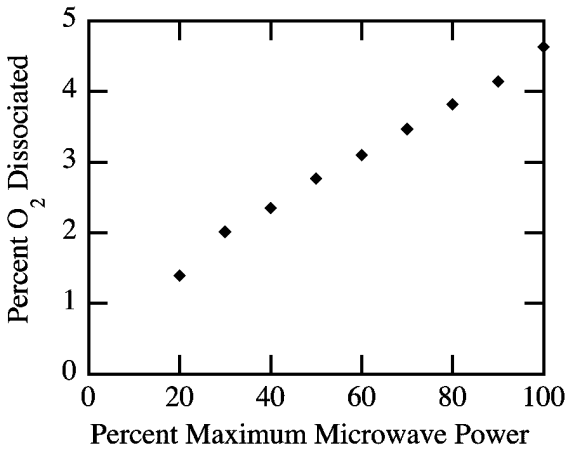
Percent O_2 Dissociated
0
1
2
3
4
5
0
20
40
60
80
100
Percent Maximum Microwave Power

Figure 4

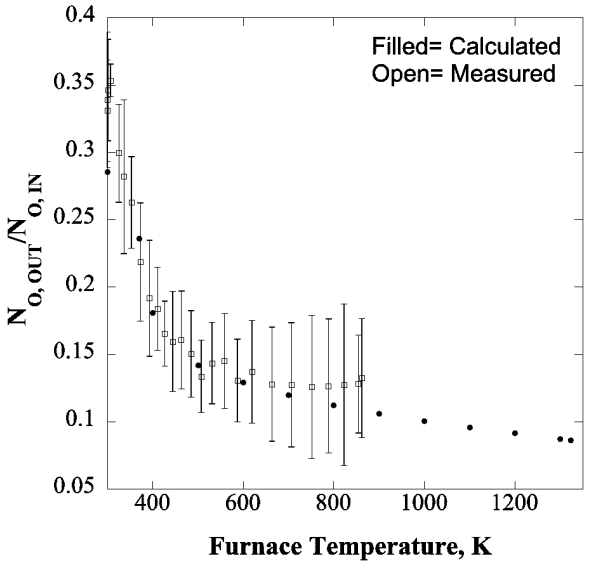
Filled= Calculated
Open= Measured
$N_{O,OUT}/N_{O,IN}$
0.4
0.35
0.3
0.25
0.2
0.15
0.1
0.05
400
600
800
1000
1200
Furnace Temperature, K

Figure 5

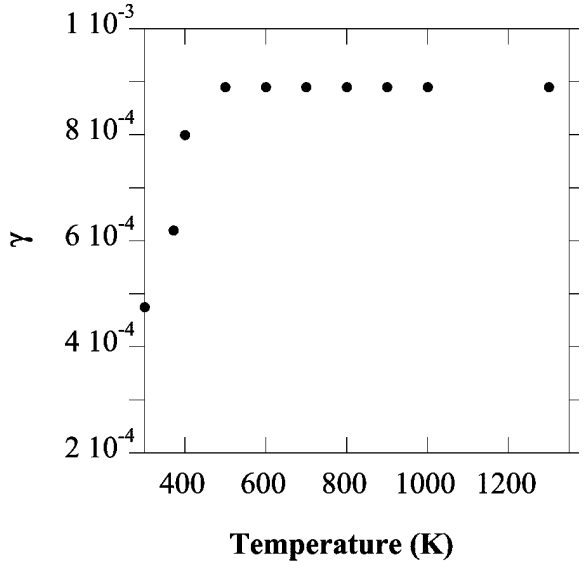
1 10-3
8 10-4
6 10-4
4 10-4
2 10-4
γ
400
600
800
1000
1200
Temperature (K)

Figure 6

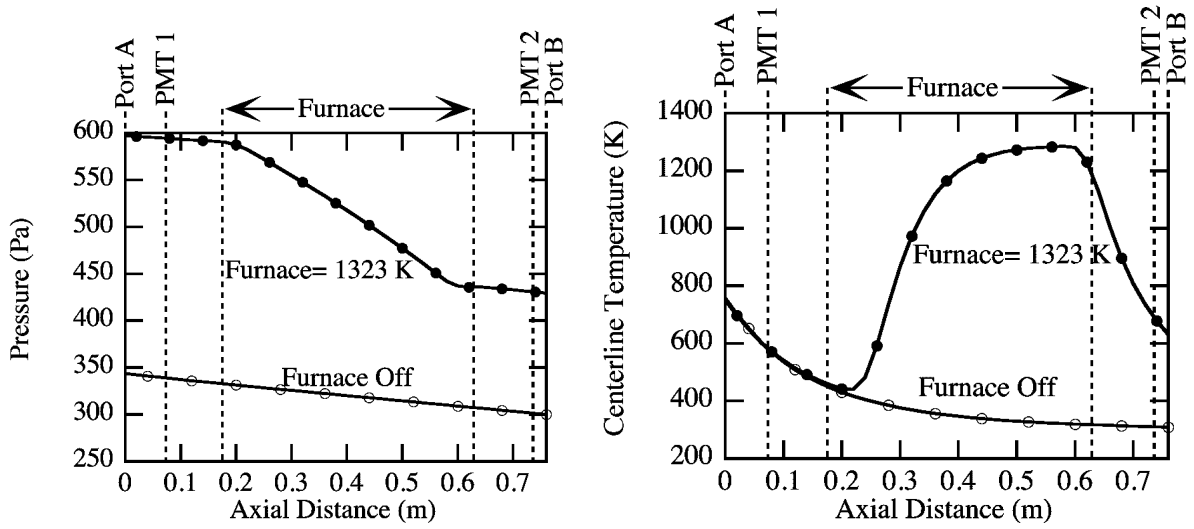
Port A
PMT 1
Furnace
PMT 2
Port B
Pressure (Pa)
600
550
500
450
400
350
300
250
Furnace= 1323 K
Furnace Off
0
0.1
0.2
0.3
0.4
0.5
0.6
0.7
Axial Distance (m)
Centerline Temperature (K)
1400
1200
1000
800
600
400
200

Figure 7

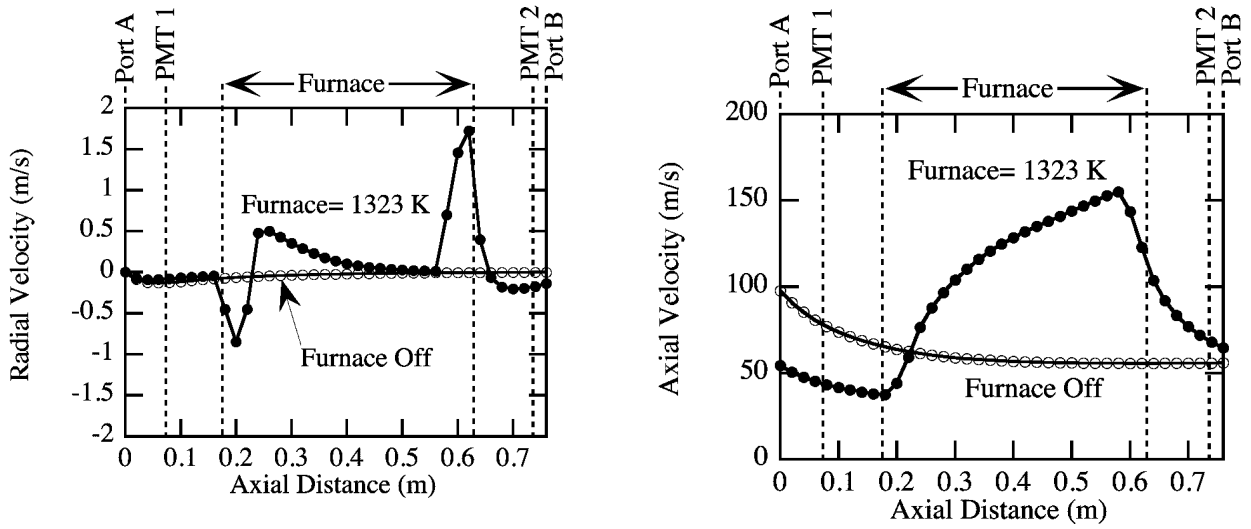
Port A
PMT 1
Furnace
PMT 2
Port B
Radial Velocity (m/s)
Furnace= 1323 K
Furnace Off
Axial Distance (m)
Axial Velocity (m/s)

Figure 8

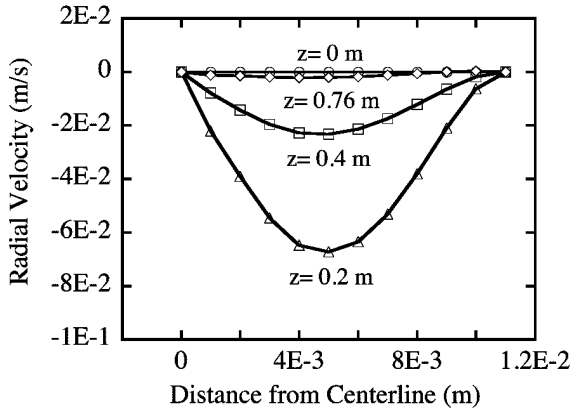
2E-2
0
-2E-2
-4E-2
-6E-2
-8E-2
-1E-1
Radial Velocity (m/s)
z= 0 m
z= 0.76 m
z= 0.4 m
z= 0.2 m
0
4E-3
8E-3
1.2E-2
Distance from Centerline (m)

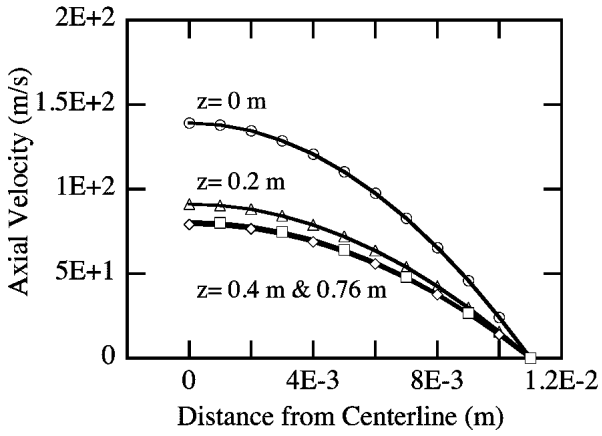
2E+2
1.5E+2
1E+2
5E+1
0
Axial Velocity (m/s)
z= 0 m
z= 0.2 m
z= 0.4 m & 0.76 m
0
4E-3
8E-3
1.2E-2
Distance from Centerline (m)

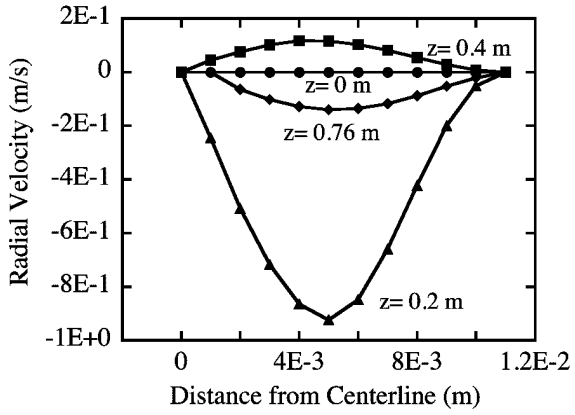
2E-1
0
-2E-1
-4E-1
-6E-1
-8E-1
-1E+0
Radial Velocity (m/s)
z= 0.4 m
z= 0 m
z= 0.76 m
z= 0.2 m
0
4E-3
8E-3
1.2E-2
Distance from Centerline (m)

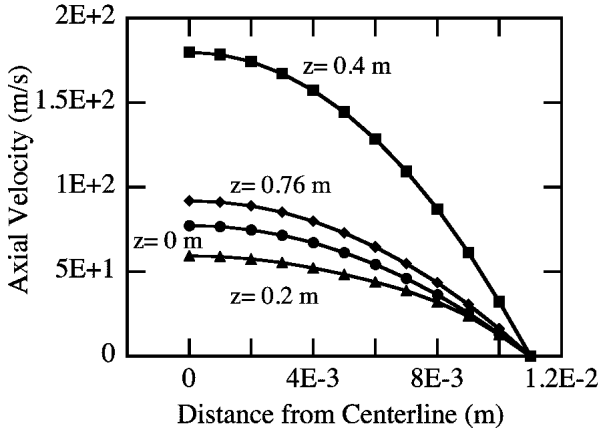
2E+2
1.5E+2
1E+2
5E+1
0
Axial Velocity (m/s)
z= 0.4 m
z= 0.76 m
z= 0 m
z= 0.2 m
0
4E-3
8E-3
1.2E-2
Distance from Centerline (m)

Figure 9

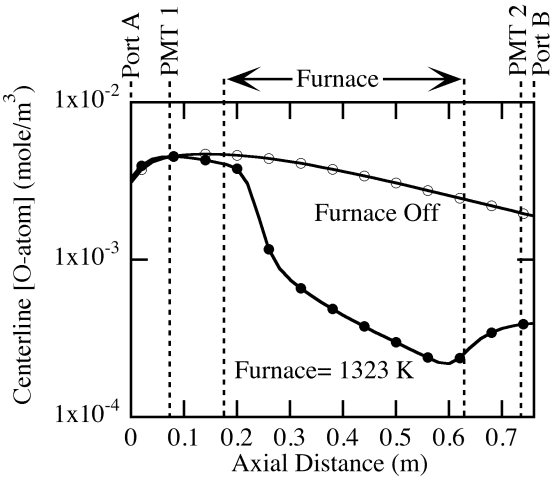
Port A
PMT 1
Furnace
PMT 2
Port B
Centerline [O-atom] (mole/m3)
1x10-2
1x10-3
1x10-4
Furnace Off
Furnace= 1323 K
0 0.1 0.2 0.3 0.4 0.5 0.6 0.7
Axial Distance (m)

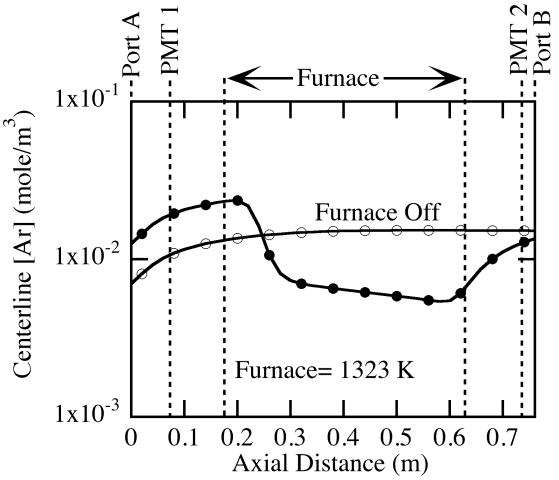
Port A
PMT 1
Furnace
PMT 2
Port B
Centerline [Ar] (mole/m3)
1x10-1
1x10-2
1x10-3
Furnace Off
Furnace= 1323 K
0 0.1 0.2 0.3 0.4 0.5 0.6 0.7
Axial Distance (m)

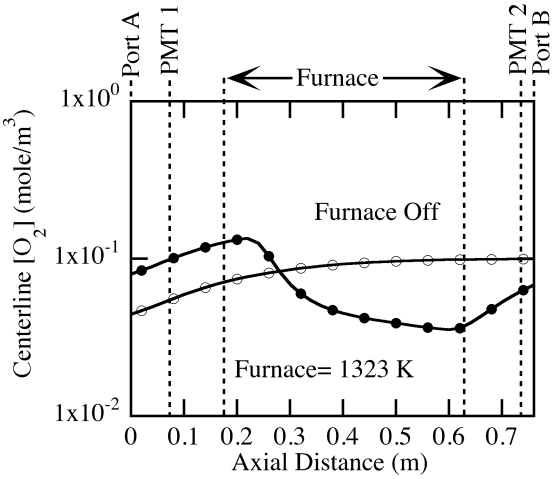
Port A
PMT 1
Furnace
PMT 2
Port B
Centerline [O2] (mole/m3)
1x100
1x10-1
1x10-2
Furnace Off
Furnace= 1323 K
0 0.1 0.2 0.3 0.4 0.5 0.6 0.7
Axial Distance (m)

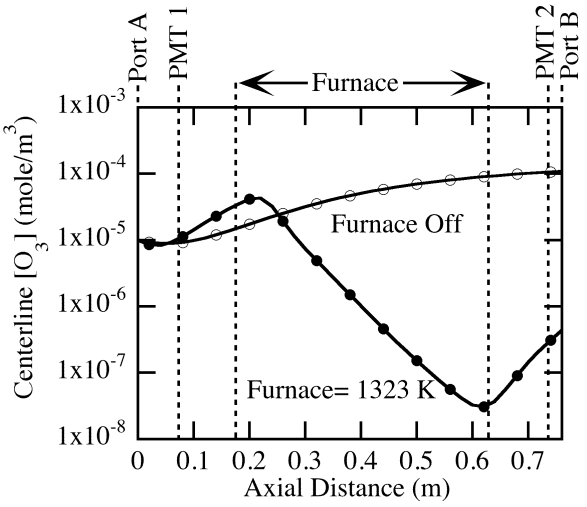
Port A
PMT 1
Furnace
PMT 2
Port B
Centerline [O3] (mole/m3)
1x10-3
1x10-4
1x10-5
1x10-6
1x10-7
1x10-8
Furnace Off
Furnace= 1323 K
0 0.1 0.2 0.3 0.4 0.5 0.6 0.7
Axial Distance (m)

Figure 10

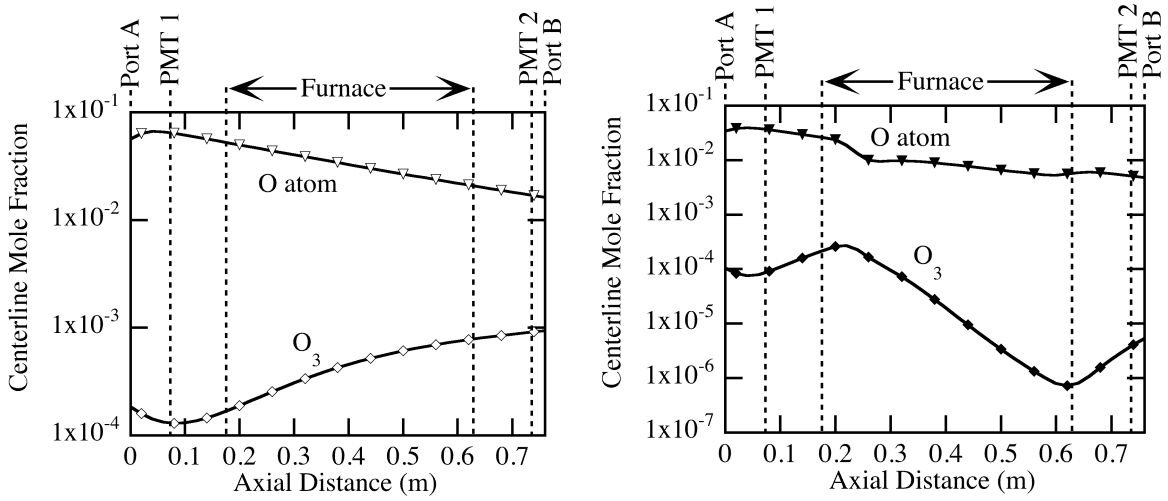
Port A
PMT 1
Furnace
PMT 2
Port B
Centerline Mole Fraction
1x10-1
1x10-2
1x10-3
1x10-4
O atom
O3
0 0.1 0.2 0.3 0.4 0.5 0.6 0.7
Axial Distance (m)
Port A
PMT 1
Furnace
PMT 2
Port B
Centerline Mole Fraction
1x10-1
1x10-2
1x10-3
1x10-4
1x10-5
1x10-6
1x10-7
O atom
O3
0 0.1 0.2 0.3 0.4 0.5 0.6 0.7
Axial Distance (m)

Figure 11

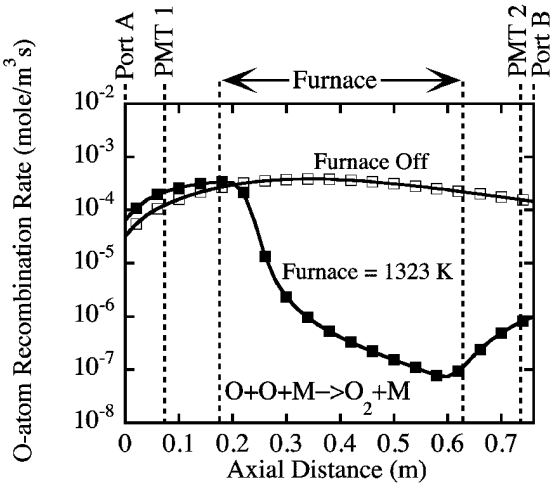
Port A
PMT 1
Furnace
PMT 2
Port B
Furnace Off
Furnace = 1323 K
O+O+M->O2+M
O-atom Recombination Rate (mole/m3 s)
Axial Distance (m)

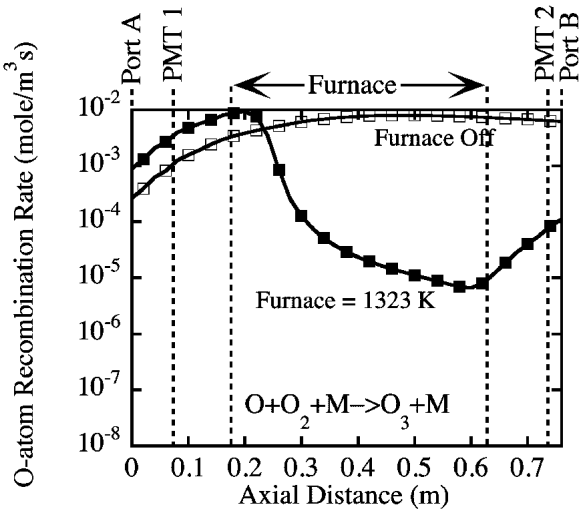
Port A
PMT 1
Furnace
PMT 2
Port B
Furnace Off
Furnace = 1323 K
O+O2+M->O3+M
O-atom Recombination Rate (mole/m3 s)
Axial Distance (m)

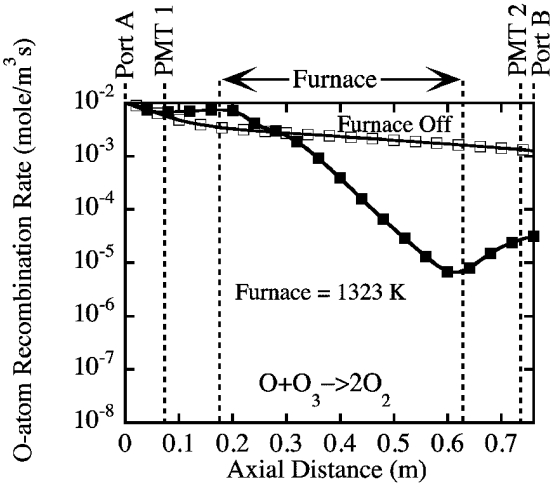
Port A
PMT 1
Furnace
PMT 2
Port B
Furnace Off
Furnace = 1323 K
O+O3->2O2
O-atom Recombination Rate (mole/m3 s)
Axial Distance (m)

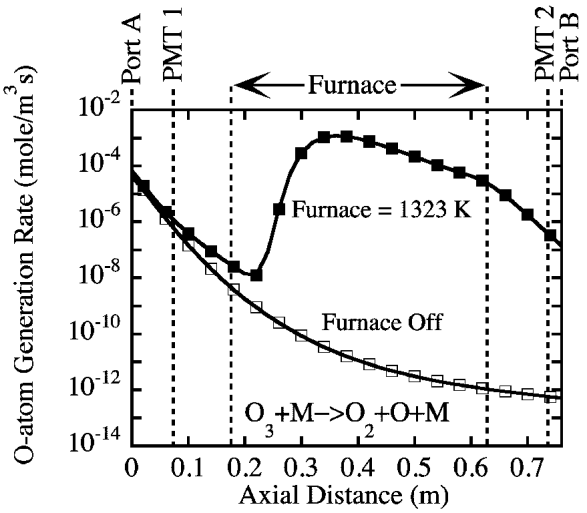
Port A
PMT 1
Furnace
PMT 2
Port B
Furnace = 1323 K
Furnace Off
O3+M->O2+O+M
O-atom Generation Rate (mole/m3 s)
Axial Distance (m)

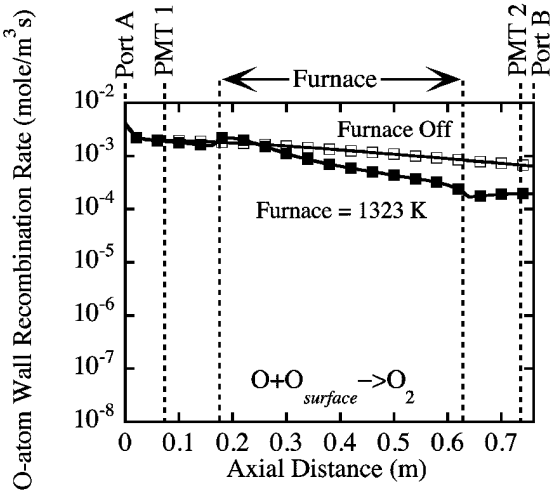
Port A
PMT 1
Furnace
PMT 2
Port B
Furnace Off
Furnace = 1323 K
O+O surface ->O2
O-atom Wall Recombination Rate (mole/m3 s)
Axial Distance (m)

References

1. B. R. Rogers and T. S. Cale, Vacuum **65** (3-4), 267-279 (2002).
2. K. T. Sung and S. W. Pang, Journal of Vacuum Science & Technology B **10** (5), 2211-2216 (1992).
3. T. Kaspar, A. Tuan, R. Tonkyn, W. P. Hess, J. W. Rogers and Y. Ono, Journal of Vacuum Science & Technology B **21** (2), 895-899 (2003).
4. K. Kim, M. H. An, Y. G. Shin, M. S. Suh, C. J. Youn, Y. H. Lee, K. B. Lee and H. J. Lee, Journal of Vacuum Science & Technology B **14** (4), 2667-2673 (1996).
5. T. A. Heppenheimer, *Facing the Heat Barrier: A History of Hypersonics*. (National Aeronautics and Space Administration, 2007).
6. W. F. N. Santos, Journal of Spacecraft and Rockets **42** (1), 22-29 (2005).
7. J. V. Rakich, D.A.S. and M. J. Lanfranco, in *AIAA/ASME 3rd Joint Thermophysics, Fluids, Plasma and Heat Transfer Conference* (St. Louis, Missouri, 1982), Vol. 80-0944.
8. Q. N. Nguyen, E. J. Opila and R. C. Robinson, Journal of the Electrochemical Society **151** (10), B558-B562 (2004).
9. M. Gasch, D. Ellerby, E. Irby, S. Beckman, M. Gusman and S. Johnson, Journal of Materials Science **39** (19), 5925-5937 (2004).
10. X. H. Zhang, P. Hu, J. C. Han and S. H. Meng, Composites Science and Technology **68** (7-8), 1718-1726 (2008).
11. J. Misewich, H. Zacharias and M. M. T. Loy, Journal of Vacuum Science & Technology B **3** (5), 1474-1478 (1985).
12. V. N. Vyrodov, Y. V. Kozlov, V. P. Martemyanov, I. N. Machulin, L. A. Mikaelyan, M. D. Skorokhvatov, S. V. Sukhotin, A. V. Etenko, Y. Declais, H. Dekerret, B. Lefievre and M. S. Obolensky, Jetp Lett+ **61** (3), 163-169 (1995).
13. P. Vasina, V. Kudrle, A. Talsky, P. Botos, M. Mrazkova and M. Mesko, Plasma Sources Science & Technology **13** (4), 668-674 (2004).
14. W. K. Bischel, B. E. Perry and D. R. Crosley, Chemical Physics Letters **82** (1), 85-88 (1981).
15. J. Marschall, in *AIAA Annual Conference* (American Institue of Aeronautics and Astronautics, Inc., 1997), pp. 97-3879.
16. W. K. Bischel, B. E. Perry and D. R. Crosley, Applied Optics **21** (8), 1419-1429 (1982).
17. K. Niemi, V. S.-v. d. Gathen and H. F. Döbele, Plasma Sources Science and Technology **14** (2), 375 (2005).
18. K. Niemi, V. S.-v. d. Gathen and H. F. Döbele, Journal of Physics D: Applied Physics **34** (15), 2330 (2001).
19. H. F. Döbele, T. Mosbach, K. Niemi and V. S.-v. d. Gathen, Plasma Sources Science and Technology **14** (2), S31 (2005).
20. S. P. Sander, R. R. Friedl, D. M. Golden, M. J. Kurylo, R. E. Huie, V. L. Orkin, G. K. Moortgat, A. R. Ravishankara, C. E. Kolb, M. J. Molina and B. J. Finlayson-Pitts, JPL Publication (2003).
21. O. C. Zienkiewicz, R. L. Taylor and P. Nithiarasu, (Elsevier).
22. W. B. J. Zimmerman, *Process Modelling and Simulation with Finite Element Methods*. (World Scientific Publishing Company, Hackensack, NJ, 2004).

23. R. C. Reid, J. M. Prausnitz and T. K. Sherwood, *The properties of gases and liquids*, 3d ed. (McGraw-Hill, New York, 1977).
24. N. P. Chopey and Knovel (Firm), (McGraw-Hill, New York, 2004), pp. 1 v. (unpaged).
25. R. H. Perry and D. W. Green, *Perry's Chemical Engineering Handbook*, 7th ed. (McGraw-Hill, 1997).
26. J. B. Pallix and R. A. Copeland, Journal of Thermophysics and Heat Transfer **10** (2), 224-233 (1996).
27. D. A. Pejakovic, K. S. Kalogerakis, R. A. Copeland and D. L. Huestis, J. Geophys. Res-Space Phys. **113** (A4), - (2008).
28. G. P. Smith and R. Robertson, Chemical Physics Letters **458** (1-3), 6-10 (2008).
29. C. L. Lin and M. T. Leu, International Journal of Chemical Kinetics **14** (4), 417-434 (1982).
30. J. M. Heimerl and T. P. Coffee, Combustion and Flame **35** (2), 117-123 (1979).
31. H. Endo, K. Glanzer and J. Troe, Journal of Physical Chemistry **83** (16), 2083-2090 (1979).
32. L. Bedra and M. J. H. Balat-Pichelin, Aerospace Science and Technology **9** (4), 318-328 (2005).
33. J. Berkowitz, in *The Structure and Chemistry of Solid Surfaces*, edited by G. A. Somorjai (John Wiley & Sons, New York, 1968), pp. 80.81-80.16.
34. J. C. Greaves and J. W. Linnett, Transactions of the Faraday Society **55**, 1355-1361 (1959).
35. Y. C. Kim and M. Boudart, Langmuir **7** (12), 2999-3005 (1991).
36. D. S. Hacker, S. A. Marshall and M. Steinberg, The Journal of Chemical Physics **35** (5), 1788-1792 (1961).
37. S. Krongelb and M. W. P. Strandberg, The Journal of Chemical Physics **31** (5), 1196-1210 (1959).
38. D. L. Baulch, Drysdale, D.D., Duxbury, J., Grant, S.J., *Evaluated kinetic data for high temperature reactions*. (Butterworths, London, 1976).
39. H. Hippler, R. Rahn and J. Troe, Journal of Chemical Physics **93** (9), 6560-6569 (1990).
40. R. Atkinson, D. L. Baulch, R. A. Cox, J. N. Crowley, R. F. Hampson, R. G. Hynes, M. E. Jenkin, M. J. Rossi and J. Troe, Atmospheric Chemistry and Physics **4**, 1461-1738 (2004).